

Electronic Thesis and Dissertation Repository

3-4-2022 2:00 PM

Cost-effective non-destructive testing of biomedical components fabricated using additive manufacturing

Santiago Fabian Cobos, *The University of Western Ontario*

Supervisor: Holdsworth, David W., *The University of Western Ontario*

A thesis submitted in partial fulfillment of the requirements for the Doctor of Philosophy degree in Medical Biophysics

© Santiago Fabian Cobos 2022

Follow this and additional works at: <https://ir.lib.uwo.ca/etd>



Part of the [Biomedical Engineering and Bioengineering Commons](#), and the [Medical Biophysics Commons](#)

Recommended Citation

Cobos, Santiago Fabian, "Cost-effective non-destructive testing of biomedical components fabricated using additive manufacturing" (2022). *Electronic Thesis and Dissertation Repository*. 8412. <https://ir.lib.uwo.ca/etd/8412>

This Dissertation/Thesis is brought to you for free and open access by Scholarship@Western. It has been accepted for inclusion in Electronic Thesis and Dissertation Repository by an authorized administrator of Scholarship@Western. For more information, please contact wlsadmin@uwo.ca.

Abstract

Biocompatible titanium-alloys can be used to fabricate patient-specific medical components using additive manufacturing (AM). These novel components have the potential to improve clinical outcomes in various medical scenarios. However, AM introduces stability and repeatability concerns, which are potential roadblocks for its widespread use in the medical sector. Micro-CT imaging for non-destructive testing (NDT) is an effective solution for post-manufacturing quality control of these components. Unfortunately, current micro-CT NDT scanners require expensive infrastructure and hardware, which translates into prohibitively expensive routine NDT. Furthermore, the limited dynamic-range of these scanners can cause severe image artifacts that may compromise the diagnostic value of the non-destructive test. Finally, the cone-beam geometry of these scanners makes them susceptible to the adverse effects of scattered radiation, which is another source of artifacts in micro-CT imaging.

In this work, we describe the design, fabrication, and implementation of a dedicated, cost-effective micro-CT scanner for NDT of AM-fabricated biomedical components. Our scanner reduces the limitations of costly image-based NDT by optimizing the scanner's geometry and the image acquisition hardware (i.e., X-ray source and detector). Additionally, we describe two novel techniques to reduce image artifacts caused by photon-starvation and scatter radiation in cone-beam micro-CT imaging.

Our cost-effective scanner was designed to match the image requirements of medium-size titanium-alloy medical components. We optimized the image acquisition hardware by using an 80 kVp low-cost portable X-ray unit and developing a low-cost lens-coupled X-ray detector. Image artifacts caused by photon-starvation were reduced by implementing dual-exposure high-dynamic-range radiography. For scatter mitigation, we describe the design, manufacturing, and testing of a large-area, highly-focused, two-dimensional, anti-scatter grid.

Our results demonstrate that cost-effective NDT using low-cost equipment is feasible for medium-sized, titanium-alloy, AM-fabricated medical components. Our proposed high-dynamic-range strategy improved by 37% the penetration capabilities of an 80 kVp micro-CT imaging system for a total x-ray path length of 19.8 mm. Finally, our novel anti-scatter

grid provided a 65% improvement in CT number accuracy and a 48% improvement in low-contrast visualization. Our proposed cost-effective scanner and artifact reduction strategies have the potential to improve patient care by accelerating the widespread use of patient-specific, bio-compatible, AM-manufactured, medical components.

Keywords

Additive manufacturing, non-destructive testing, laser powder-bed fusion, customized-medicine, cone-beam CT, anti-scatter grid, high-dynamic range CT, under-ranging, CT artifacts

Summary for Lay Audience

In medicine, 3D printing technologies are currently changing the way doctors treat patients. Medical images can now be used to produce patient-specific medical components, improving the results of the treatments. These medical components need to be carefully inspected before being used. However, current 3D inspecting methods are too costly for routine quality control. These methods are costly because they require expensive hardware and expensive infrastructure. Furthermore, because these 3D inspecting methods use X-rays to 'see' inside the medical component, they are susceptible to various limitations due to complex interactions between the X-rays and the component's material. The goals of this thesis were (1) to develop a cost-effective solution for quality control of these novel medical components using 3D X-ray imaging and (2) to reduce the impact of non-idealities caused by complex X-ray physics to improve the quality of these inspections.

In this work, I propose using low-cost X-ray equipment to build a cost-effective, 3D, X-ray scanner for quality control of components manufactured using medical 3D printing. First, I showed that these titanium-alloy medical components have characteristics that make them suitable for inspection using non-sophisticated X-ray imaging equipment. Following this, I developed a low-cost X-ray detector using off-the-shelf hardware combined with the previously described X-ray equipment to build a cost-effective 3D scanner. Finally, I describe two advanced methods to improve the quality of the X-ray-based inspection by reducing the negative effects of scattered radiation and photon starvation, which are two well-known sources of error in 3D X-ray imaging. I found that our cost-effective 3D scanner was able to produce inspection images with the required accuracy to be used for quality control in the medical industry. Additionally, I demonstrated that anti-scatter grids and high-dynamic-range radiography are effective means to improve the image quality of this type of scanner. I believe that the work presented in this thesis offers a cost-effective alternative for inspecting medical devices produced using medical 3D printing. The use of this technology will propel the clinical use of these innovative treatment options using 3D printing.

Co-Authorship Statement

This thesis is presented in an integrated article format, the body of this dissertation is based on the following research articles which are all submitted for publication:

Chapter 2: Cobos S.F., Norley C.J., Pollmann S.I., and Holdsworth D.W., Cost-effective micro-CT system for non-destructive testing of titanium 3D printed medical components. Submitted to Plos One on October 14, 2021.

My contributions to this work include study conception, manufacturing of supporting hardware, software for hardware integration, system's design and development, system's calibration, data collection, image reconstruction, data analysis, and manuscript preparation. C. Norley contributed with the proof reading and scientific editing of the manuscript. S. Pollmann developed software for: camera integration, data acquisition, data correction, and reconstruction. Dr. D. Holdsworth contributed to study conception, data interpretation and analysis, funding allocation, and manuscript preparation.

Chapter 3: Cobos S.F., Norley C.J., Pollmann S.I., and Holdsworth D.W., High-dynamic-range micro-CT for non-destructive testing of titanium 3D-printed medical components. Submitted to Journal of Medical Imaging on March 03, 2022.

My contributions to this work include study conception, data acquisition hardware modifications, data collection, data analysis, software for image processing, and manuscript preparation. C. Norley contributed with the proof reading and scientific editing of the manuscript. S. Pollmann developed the software for data processing. Dr. D. Holdsworth contributed to study conception, phantom design, data interpretation and analysis, funding allocation, and manuscript preparation.

Chapter 4: Cobos S.F., Norley C.J., Nikolov H.N., and Holdsworth D.W., 3D printed large-area focused grid for scatter reduction in cone-beam CT. Submitted to Medical Physics on September 06, 2021; revisions have been requested.

My contributions to this work include study conception, software for parametric modelling, anti-scatter grid's design, scanner development, software and hardware for integration of

scanner's components, data collection, software for grid-line artifact correction, data post-processing, CT reconstruction, data analysis, and manuscript preparation. C. Norley contributed with the proof reading and scientific editing of the manuscript. H. Nikolov manufacturing of the anti-scatter grid, phantom conditioning, and proof reading of the manuscript. Dr. D. Holdsworth contributed to study conception, anti-scatter grid design, data interpretation and analysis, funding allocation, and manuscript preparation.

Acknowledgments

This journey has been as challenging as rewarding, and I am grateful for the help and support of everyone involved. This dissertation, and most in science, in my belief, could not have been completed without the work of a team comprised of kind, inquisitive, compassionate, and adventurous minds. The following lines are a most likely inappropriate attempt to recognize their contributions and highlight this unequivocal fact.

First and foremost, I would like to thank Dr. David Holdsworth for providing me with the opportunity to join his research group and for all his guidance, support, and generosity. There is no doubt that individuals like Dr. Holdsworth are fundamental for the non-random assembly of these high-quality teams capable of fostering equal quality science. In particular, I would like to sincerely and fondly thank Hristo Nikolov and Chris Norley for their help with all aspects of my growth as a young researcher. Their support, guidance, and friendship made this journey walkable. Additionally, I would like to extend my gratitude to the entire Holdsworth Lab. research group as they were always kind, helpful, and supportive.

I would like to say thanks to all the additional academic, and technical support received from the members of my advisory committee, the department of Medical Biophysics, ADEISS, the Robarts Research Institute, the Bone and Joint Institute, the Collaborative Program in MSK Health Research, the Writing Support Centre, and Western Libraries. Having access to this extensive network of resources and support was a privilege and a critical reason for the success of my research projects. In particular, I would like to mention the guidance, help, and advice I received from Dr. Yara Hosein, Tom Chmiel, Kathleen Petts, Jacques Montreuil, and Kevin Barker.

Regarding non-academic support, I want to acknowledge the sources of additional funding that allowed me to concentrate on my academic endeavors without extra worries. In particular, Dr. Jacinta Santos, Dr. Steven Ferrier, and Dr. Ali Tassi for trusting me with several educational responsibilities as Adjunct Clinical Instructor, Lecturer, and Course Coordinator. I also want to extend my feelings of gratitude to the fantastic human resources from the Department of Anatomy and Cell Biology, Tom Chrones, Haley Linklater, and Kevin Walker. And finally, a special thanks to the tremendous generosity of Dr. Khadry

Galil and for his mentorship and guidance when obtaining these work opportunities. They certainly added extremely valuable teaching experiences to this journey.

Outside of the academic and professional world, I want to say thanks to all the amazing people who offered me their sincere friendship, emotional support, and company. In no particular order, except for the first name, I want to mention Jessica, Oleksiy, Jenna, Yolanda, Michelle, Tyler, Shannon, Hareem, Francisco, Gollie, Sara, Allie, Adrian, Tomi, and Greg. You all improved my quality of life significantly, and I am extremely lucky for having the opportunity to know you.

Finally, I want to mention some of the names of people, and others, without whom I will be who I am. They have gifted me privileges that are almost impossible to measure. They are: my parents, Norma and Diego; my grandparents, Silvia, Laura, Roberto, and Tomas; my siblings Fabiola and Diego; my mentor Rajah; my home-friends Richard, Alejandro, Andres, Cristobal, Luis, Cristina, Johanna, and Vanessa; and my pets Chiqui, Smokey, and Barbas. Thanks for being so generous towards me. I could not have done any of this without you! Thanks to all of you for all your relentless efforts to improve my life I am very lucky!

Table of Contents

Abstract.....	ii
Summary for Lay Audience.....	iv
Co-Authorship Statement.....	v
Acknowledgments.....	vii
Table of Contents.....	ix
List of Tables.....	xiii
List of Figures.....	xiv
List of Abbreviations.....	xxiii
Chapter 1.....	1
1 General introduction.....	1
1.1 What is additive manufacturing?.....	1
1.2 Additive manufacturing in the medical industry.....	1
1.2.1 Additive manufacturing of bio metallic medical components.....	3
1.3 Common characteristics of AM-fabricated biomedical components.....	5
1.4 Non-destructive testing.....	7
1.4.1 Cost-effectiveness and alternatives.....	8
1.4.2 Lens-coupled x-ray detectors.....	9
1.4.3 Image artifacts and limitations.....	11
1.5 Anti-scatter grids for cone-beam CT.....	15
1.6 High-dynamic range radiography.....	18
1.7 Objectives.....	19
1.8 Thesis outline.....	19
1.9 References.....	21
Chapter 2.....	27

2	Cost-effective micro-CT system for non-destructive testing of titanium 3D printed medical components.....	27
2.1	Introduction.....	28
2.2	Methods.....	29
2.2.1	System Geometry Description	29
2.2.2	Internal Components and Experimental Setup	32
2.2.3	Geometric Calibration and CT Reconstruction.....	35
2.2.4	Phantoms.....	38
2.2.5	Data Analysis	41
2.3	Results.....	43
2.3.1	Cost-effectiveness analysis	43
2.3.2	Geometric correction	44
2.3.3	Imaging Characteristics of the System	46
2.3.4	Titanium metal-alloy (Ti6Al4V) phantoms	52
2.4	Discussion.....	55
2.5	Conclusion	59
2.6	Acknowledgments.....	60
2.7	References.....	60
	Chapter 3.....	63
3	High-dynamic-range micro-CT for non-destructive testing of titanium 3D-printed medical components.....	63
3.1	Introduction.....	64
3.2	Methods.....	66
3.2.1	Scanned Test Samples.....	66
3.2.2	Dual-exposure Data Acquisition.....	68
3.2.3	Dual-exposure HDR Projection Data Post-processing	70
3.2.4	CT Reconstruction and Data Analysis	72

3.3	Results.....	73
3.3.1	Generation of HDR Projection Images	73
3.3.2	HDR-CT of Porous Cylindrical Samples.....	77
3.3.3	HDR-CT of Resolution Phantom.....	78
3.4	Discussion.....	80
3.5	Conclusion	82
3.6	Acknowledgments.....	83
3.7	References.....	83
Chapter 4	85
4	3D printed large-area focused grid for scatter reduction in cone-beam CT.....	85
4.1	Introduction.....	86
4.2	Methods.....	89
4.2.1	2D Anti-scatter grid parametric modelling.....	89
4.2.2	2D-ASG manufacturing	92
4.2.3	Verification of grid septa dimensions	94
4.2.4	CBCT experimental setup.....	95
4.2.5	2D low-contrast visualization	96
4.2.6	Grid-line artifact corrections and CBCT reconstruction.....	97
4.2.7	CBCT data analysis.....	100
4.3	Results.....	103
4.3.1	Parametric modelling	103
4.3.2	2D-ASG post-manufacturing evaluation	104
4.3.3	2D low-contrast visualization	106
4.3.4	Evaluation of grid-line artifact correction.....	107
4.3.5	CBCT image quality evaluation.....	110
4.4	Discussion.....	117

4.5 Conclusion	121
4.6 Acknowledgements.....	123
4.7 References.....	123
Chapter 5.....	130
5 General discussion and conclusions.....	130
5.1 Development of the bodies of research.....	130
5.2 Overview and Objectives	131
5.3 Cost-effective NDT of titanium-alloy biomedical components.....	132
5.4 Large-area 2D focused anti-scatter grids	136
5.5 Significance and future directives.....	138
5.6 References.....	140
Curriculum Vitae	144

List of Tables

Table 1-1: Advantages of AM in the production of bio metallic medical components.....	4
Table 1-2: Key mechanical properties of the most used medical-grade metals fabricated using AM.	5
Table 2-1. X-ray source comparisons and exposure-level matching, x-ray protocols.....	34
Table 2-2. Summary of the estimated costs for the main components of our low-cost CT scanner.	44
Table 2-3. Sub-voxel, Euclidean distances between the centroids of all five beads of the geometric accuracy plate of the CT quality assurance phantom.....	49
Table 3-1. Dual-exposure HDR protocols for the eXplore Locus RS X-ray scanner.....	69
Table 3-2. Summary of HDR-CT protocol-pairs per test sample.....	74
Table 4-1. 2D-ASG design parameters.....	91
Table 4-2. Contrast plate CNR calculations with and without 2D-ASG.	113
Table 5-1. Overall development of bodies of research	130

List of Figures

Fig 1-1. (a) titanium cranial plate, with (b) CT scan data at 80 kVp (GE Ultra, 150 μ m, 16 s scan).....	6
Fig 1-2. Geometry of a cone-beam CT system. The diagram shows the main parameters of a stationary source design. (SOD, source–object distance and SDD, source–detector distance).	8
Fig 1-3. Illustration of a focused anti-scatter grid. Each grid channel has a unique angle aligned towards the focal spot of the CBCT geometry.....	17
Fig 2-1. Geometry of the micro-CT System. (a) Top view depicting the arrangement of the internal components of the system: x-ray source, rotary stage, phosphor detector screen, detector-screen tilt angle (DSTA), lead plate, camera, lens, source-to-object distance (SOD), and object-to-detector distance (ODD). The orange dotted-lines represent the trajectory of the polychromatic, cone-shaped, x-ray beam. (b) Perspective view of the system showing the arrangement of the various 2 x 2 cm aluminum extrusion profiles. One of the opaque panels was removed from the 3D rendering to allow visualization of the internal components.	31
Fig 2-2. Experimental Setup using the General-Purpose X-ray Source. Note that the rotary stage is not visible as it is hidden behind the lead plate. The source-to-detector distance (SDD) was 60 cm.....	33
Fig 2-3. Summary of image processing steps required between projection data acquisition and CT reconstruction.....	35
Fig 2-4. Assessment of geometric distortion correction resulting from the tilted-detector configuration. (a) shows the un-corrected, raw data of the Cartesian calibration grid. (b) corrected image of the Cartesian calibration grid.	37
Fig 2-5 Physical appearance of the imaged phantoms for this study. (a) comprehensive quality assurance CT phantom, (b) porous, gyroid-based, cylindrical, titanium-alloy (Ti6Al4V) phantom, and (c) titanium-alloy (Ti6Al4V) resolution phantom.	38

Fig 2-6 Computer-aided design (CAD) of the porous, gyroid-based, cylindrical, titanium-alloy (Ti6Al4V) scaffold. (a) perspective view of 3D rendering of the CAD. (b) Trans-coronal synthetic slice of the porous cylinder CAD. (c) Trans-sagittal synthetic slice of the porous cylinder CAD. (d) Transaxial synthetic slice of the porous cylinder CAD. (b),(c), and (d) are color coded to depict the titanium-alloy (yellow) and internal porosity (red) regions of the scaffold..... 40

Fig 2-7 Computer-aided design (CAD) of the resolution titanium-alloy (Ti6Al4V) phantom. (a) translucent perspective view of 3D rendering of the phantom’s CAD. (b) Trans-coronal synthetic slice of the phantom’s CAD. (c) Trans-sagittal synthetic slice of the phantom’s CAD depicting details of the internal voids. The bar patterns are described in $lp\ mm^{-1}$ all the other measurements are shown in mm (d) Transaxial synthetic slice of the phantom’s CAD. 41

Fig 2-8. Results of geometric calibration evaluation using a cylindrical phantom with four radiopaque marker beads. (a) x-ray projection radiograph of the phantom; (b) uncorrected and corrected elliptical trajectories prescribed by the phantom’s markers over the course of one full rotation of the rotary stage. (c) close-up of uncorrected and corrected elliptical trajectories of the top-most marker bead. The corrected position of the markers aligns with the ideal trajectory calculated using a sinusoidal best fit..... 45

Fig 2-9. Evaluation of spatial resolution of the cost-efficient CT scanner. (a) a single reconstructed transaxial-slice CT image of the slanted-edge plate of the CT quality assurance phantom. (b) reconstructed transaxial-slice CT image of the resolution coil plate of the CT quality assurance phantom illustrating the qualitative display of resolution coils. 47

Fig 2-10. Modulation transfer function (MTF) of the cost-effective CT scanner measured from the slanted-edge plate, the resolution coil plate, and the copper wire of the CT quality assurance phantom. The 10% MTF level was reached at $2.12\ mm^{-1}$, corresponding to a spatial resolution of $235\ \mu m$ 47

Fig 2-11. Reconstructed transaxial-slice CT image of the geometric-accuracy plate of the CT quality assurance phantom with four beads located at the periphery and 35 mm apart and one central bead at a distance of 24.75 mm from the other four. 48

Fig 2-12. Reconstructed transaxial-slice CT images of the linearity plate (a) with air, water, and various concentrations of iodine shown in ml mg^{-1} ; and the CT number evaluation plate (b) of the CT quality assurance phantom..... 50

Fig 2-13. Plot of measured CT number within ROIs placed in each iodine vial versus known iodine concentration within the linearity plate of the CT quality assurance phantom. A significant linear correlation is seen between CT number in HU and iodine concentration in mg ml^{-1} 51

Fig 2-14. (a) Reconstructed transaxial-slice CT image of the uniformity plate of the CT quality assurance phantom. (b) Radial signal profile taken through the center of the uniformity plate as illustrated by the white dotted-line in (a)..... 52

Fig 2-15. CT reconstruction of the porous, gyroid-based, cylindrical, titanium-alloy (Ti6Al4V) scaffold using the cost-effective CT scanner. (a) perspective view of volumetric rendering using the FWHM threshold used to segment titanium. (b) Trans-coronal slice CT reconstruction of the porous cylinder. (c) Signal profile across a wall of the porous cylinder used to determine the FWHM threshold for segmentation. (d) Trans-sagittal slice CT reconstruction of the porous cylinder. (e) Transaxial slice CT reconstruction of the porous cylinder and line profile used for (c). (f) close-up version of (e) illustrating boundaries between the titanium and air ROIs used to measure the porosity of the porous, cylindrical, titanium scaffold. 53

Fig 2-16. Beam-hardening corrected CT reconstruction of the titanium-alloy resolution phantom using the cost-effective CT scanner. (a) Volumetric rendering of the phantom with the top cap clipped to reveal the internal-void features of the resolution phantom. (b) Transcoronal slice of the resolution phantom showing the relative position of the clipping plane for (a). (c) Close-up of (e) illustrating the internal features of the phantom at the level of the clipping plane where the outer diameter of the object is 10 mm. (d) Transsagittal slice of the resolution phantom showing the level where the resolution limit was reached. (e) Transaxial slice of the resolution phantom showing details of the internal features of the phantom. (f) Transaxial slice at the level of the resolution limit where the external diameter of the phantom was 13 mm. At diameters greater than this, internal-void features are difficult to distinguish, and photon starvation artifacts start to dominate. 54

Fig 3-1. Test samples scanned in this project. (a) Titanium-alloy, gyroid-based, cylindrical samples with porosity fractions of 60, 70, 80 and 90%. (b) Titanium-alloy, resolution and conspicuity phantom. The internal features of this resolution phantom are described in Fig 3-2. 67

Fig 3-2. Detailed schematics of the titanium-alloy, resolution and conspicuity phantom. (a) Perspective view of the 3D-rendering of the computer-assisted design (CAD) with a transparency filter. (b) Central, trans-coronal, synthetic slice of the phantom’s CAD. (c) Central, trans-axial, synthetic slice of the phantom’s CAD illustrating the details of the internal voids. The bar patterns are described in lp mm^{-1} . All other measurements are shown in mm. (d) Central, trans-sagittal, synthetic slice of the phantom’s CAD..... 68

Fig 3-3. Projection images used to generate HDR data illustrating the location of the 95% saturation and 75% saturation threshold boundaries. (a) Projection image of the titanium-alloy, resolution phantom acquired using the EV0 protocol. (b) Projection image of the titanium-alloy, resolution phantom acquired using the EV4 protocol..... 72

Fig 3-4. Scaling factors (Equation 3.1) for matching the intensity of EV0 projection images to EVn as a function of projection angle for the 60% porosity cylinder for: (a) the EV0, EV2 HDR pair and (b) the EV0, EV3 HDR pair, and for the resolution and conspicuity phantom for: (c) the EV0, EV2 HDR pair; (d) the EV0, EV3 HDR pair; and (e) the EV0, EV4 HDR pair. 75

Fig 3-5. HDR strategy for the combination of EV0 with EVn projection images. (a) Dark-corrected, EV0 projection image of the resolution and conspicuity phantom, scaled to match the intensity values of EV4 (*i.e.*, intensity-matched, IM EV0). Due to a long ray path through the metal in the central region of the phantom, pixels were underexposed in the EV0 image and were discarded from the final HDR projection image. (b) Corresponding, dark-corrected EV4 projection, showing regions with saturated pixels and valid data. (c) Line profile through pixels marked by the red-dotted line in (a) and (b) showing the $\sin^2 + \cos^2$, weighted-average combination strategy for pixels with intensity values between the 95% (t_{95}) and 75% (t_{75}) saturation thresholds..... 76

Fig 3-6. Results of the CT reconstructions for the 60% titanium-alloy, porous cylinder. (a), (b) and (c) show a trans-axial slice through the data for the conventional-DR, the EV0 EV2 pair, and the EV0 EV3 pair, respectively. (d) Shows a 3D-rendering of the data in a perspective view. (e) and (f) show the voxel values through a line-profile following the red-dotted line in (a) to compare the differences in signal-to-noise ratio between datasets. 77

Fig 3-7. Results of the CT reconstructions for the 70% and 80% titanium-alloy, porous cylinders. (a) and (b) show a trans-axial slice through the 70% porous, cylinder for the conventional-DR and the EV0 EV3 pair, respectively. (d) and (e) show a trans-axial slice through the 80% porous, cylinder for the conventional-DR and the EV0 EV2 pair, respectively. (c) and (f) show the voxel values through a line-profile following the red-dotted line in (a) and (d) to compare the differences in signal-to-noise ratio between the respective datasets..... 78

Fig 3-8. CT reconstructions for the resolution and conspicuity phantom. (a), (b), (d), and (e) show a trans-coronal slice through the reconstructed data for the conventional-DR, the EV0 EV2, the EV0 EV3, and EV0 EV4 pairs, respectively. The red arrows in these images describe the location of the void conspicuity limit for the 30 μm wide and the 300 μm wide prismatic voids. The red horizontal lines mark the void conspicuity limit reached by the immediately shorter HDR reconstruction. The red circle in (e) shows the location of a discontinuity artifact for the EV0 EV4 dataset. (c) Shows a 3D rendering of a perspective view of the EV0 EV3 HDR reconstruction with the top portion of the phantom clipped at the level marked in (a). (f) Shows the intensity values of voxels in a profile-line located along the longitudinal axis of the phantom, and within the 300 μm wide prismatic void. 79

Fig 4-1. Close-up of 2D-ASG septal cell. (a) grid height, (b) element size, (c) septal thickness, and (d) inclination angle to match CBCT geometry. 90

Fig 4-2. QuantAM 3D printing interface preview of grid placement in the (250x250 mm) build-plate. Red arrow shows build-plate securing clearance holes, which limited grid size in one dimension. 92

Fig 4-3. QuantAM laser scanning strategy preview for the top layer of the large-area, focused, 2D-ASG. (a) Laser scanning pattern starting at the top-left corner of the grid's

frame. (b) Close-up of grid septa being consolidated with a single laser path, white arrows show the progression of laser position across the grid.	93
Fig 4-4. Custom, stationary-source, CBCT experimental setup. Ceiling-mounted x-ray unit, precision rotary stage, 2D-ASG, and flat-panel digital detector.....	95
Fig 4-5. (305x154 mm) modular QA phantom used to evaluate CBCT image quality characteristics. The different sections and plates are arranged from left-to-right in the image.	96
Fig 4-6. 3D rendering of the design of the 2D, 3D-printed, low-contrast phantom.	97
Fig 4-7. Exposure dependent gain-factor variations for three, example, detector elements illustrating the effect of varying the degree of grid septa shadow. Septa represents low shadow and septal intersection a greater degree of shadow. Power series curve-fits are shown in solid lines.	99
Fig 4-8. FFT images of an open acquisition with the 2D anti-scatter grid in place. (a) FFT power-spectrum. (b) thresholded and manually segmented binary-mask of FFT notch filter use to remove grid-line artifacts from projection images in frequency space.	100
Fig 4-9. Technical details of the modular QA phantom. (a) Modules organization. (b) Spatial resolution section comprised of a (5x6) tungsten-carbide beads array, and a (x-z) slanted-edge. (c) Geometric accuracy plate with five steel beads designed to verify voxel-spacing in the reconstructed images. (d) Spatial resolution plate comprised of a (x-y) slanted-edge. (e) Spatial resolution plate used for qualitative evaluation using bar-patterns with different pitches, values are expressed in $lp \times mm^{-1}$. (f) Artifacts characterization plate designed to investigate artifacts that may be encountered near large dense objects (<i>i.e.</i> , trabecular bone or metal implants). (g) Contrast plate comprised of bone-mimicking inserts (CIRS, Norfolk, VA and SB3™ Gamex RMI, Middleton, WI), values are expressed in $mg \times cm^{-3}$ of bone mineral density. (h) Linearity plate with iodine filled vials (Omnipaque, Sanofi Winthrop, New York, NY) at different concentrations, values in $mg \times ml^{-1}$	102

Fig 4-10. Blender 2D-ASG parametric modelling module. (a) Node-tree interface with various user definable 2D-ASG parameters. (b) CAD model preview and drawing of the optimized geometry of one grid channel. 104

Fig 4-11. Large-area, focused, 2D-ASG after manufacturing and post-processing. (a) closeup of grid septa using the measuring microscope (nominal septal width was 101 μm). (b) picture of the 2D-ASG after heat treatment still attached to the LBPF build-plate..... 104

Fig 4-12. Grid-septa shadow consistency across the 2D-ASG (a-e) close-up images of gain maps at various regions of the grid upper left, center, upper right, lower left, and lower right, respectively. (f) line profiles across five grid-septa at each location showing consistency of grid-septa shadow thickness. The line profiles, for each region, were placed approximately in the same relative location marked by the red-dotted line in (b). 105

Fig 4-13. Cumulative histogram of the transmission map for a flood-field image of the large-area, focused, 2D-ASG. 106

Fig 4-14. Low-contrast object conspicuity: 2D radiographs of the low-contrast phantom acquired with a 15 cm water bath and (a) without ASG, versus (b) with 2D-ASG. (c and d) show improvements in CNR across the 5 mm and 3 mm holes marked by the dotted box in (b). Images are shown using identical window and level settings..... 107

Fig 4-15. Close-up of QA phantom region in a CBCT 2D-projection image. (a) uncorrected, raw grid-line artifacts (b) with flat-field correction (c) with exposure-dependent gain correction, (d) with exposure-dependent gain correction and notch-FFT-filter and (e) line-profiles (across yellow-dotted line in (a)) showing the reduction of grid-line artifact intensity using the exposure-dependent correction method and further notch-FFT-filter..... 108

Fig 4-16. Resolution plate of QA phantom reconstructed (a) using linear-gain correction, (b) using exposure-dependent gain correction, and (c) after both exposure-dependent gain correction and Fourier-notch filtering. Standard deviations calculated in the outlined circular, yellow ROI show improvements in image quality using the proposed GLA correction method..... 109

Fig 4-17. CT number accuracy improvements for air-filled, slanted-edge chamber inside the QA phantom. (a) reconstruction with traditional gain correction (b) with exposure-dependent gain correction, and (c) using Fourier filtering. (d, e) show line profiles, marked by the yellow dotted line in (a), across the air-filled structure. 110

Fig 4-18. (a) CBCT slice of the geometric accuracy plate of the QA phantom, (b) closeup of the area in yellow-dotted lines in (a) showing the five steel beads in the axial plane and measured inter-bead distance. 111

Fig 4-19. Modulation transfer function (MTF) of the CBCT reconstructions measured from the slanted-edge plate of the QA phantom. 112

Fig 4-20. Qualitative evaluation of spatial resolution using the resolution plate of the QA phantom. (a) CBCT reconstruction without 2D-ASG. (b) CBCT reconstruction with 2D-ASG. (c) details of the resolution plate with interleaved Mylar and Aluminum sheets in lp/mm. (d, e) magnified images of (a) and (b) respectively. 112

Fig 4-21. Evaluation of contrast and linearity using the contrast plate of the QA phantom. (a) details of the contrast plate showing BMD inserts at various densities. (b) CBCT reconstruction without 2D-ASG. (c) CBCT reconstruction with 2D-ASG. (d) Linearity plots for the reconstruction without the 2D-ASG (d), and with the 2D-ASG (e) (linearity plots represent HU as a function of bone mineral density). 114

Fig 4-22. CT number accuracy evaluation using the uniformity plate of the QA phantom (a) CBCT reconstruction of the uniformity plate without 2D-ASG. (b) CBCT reconstruction of the uniformity plate with 2D-ASG. (c) HU profile along the dotted line in (a). 115

Fig 4-23. CT number accuracy evaluation using the slanted-edge, MTF, resolution plate of the QA phantom (a) CBCT reconstruction of the resolution plate without the 2D-ASG. (b) CBCT reconstruction of the resolution plate with the 2D-ASG. (c) shows a linear profile in HU across the phantom along the yellow dotted line in (a). 116

Fig 4-24. Experimental x-ray spectral characteristics and percent transmission through 2D-ASG septa. (a) characterization of the x-ray spectrum for CBCT data acquisition with an

additional 154 mm of water filtration. (b) photon percent transmission through 0.9 to 5 mm of cobalt-chrome septal material..... 117

List of Abbreviations

ADEISS	Additive design in surgical solutions facility
AM	Additive manufacturing
ADU	Analog-to-digital units
ASG	Anti-scatter grid
AI	Artificial intelligence
CCD	Charge coupled devices
CMOS	Complementary metal oxide semiconductor
CT	Computed tomography
CAD	Computer-assisted design
CBCT	Cone-beam computed tomography
CNR	Contrast-to-noise ratio
DSTA	Detector screen tilt angle
dSLR	Digital single-lens reflex
DED	Direct energy deposition
DR	Dynamic range
EDM	Electrical discharge machining
EPBF	Electron beam powder-bed fusion
EV	Exposure value
FDK	Feldkamp Davis and Kress
FOV	Field-of-view

FFT	Fourier fast transform
FWHM	Full-width-at-half-maximum
FDM	Fused deposition modelling
GLA	Grid-line artifacts
HDR	High-dynamic range
HDR-CT	High-dynamic range computed tomography
HU	Hounsfield unit
LPBF	Laser powder-bed fusion
MTF	Modulation transfer function
NDT	Non-destructive testing
ODD	Object-to-detector distance
1D-ASG	One-dimensional anti-scatter grid
PBF	Powder-bed fusion
QA	Quality assurance
RGGB	Red green green blue
ROI	Region-of-interest
SPR	Scatter-to-primary ratio
SLS	Selective laser sintering
SNR	Signal-to-noise ratio
SDD	Source-to-detector distance

SOD	Source-to-object distance
SLA	Stereolithography
STL	Stereolithographic file
3D	Three-dimensional
2D-ASG	Two-dimensional focused anti-scatter grid
UI	Uniformity index

Chapter 1

1 General introduction

1.1 What is additive manufacturing?

Today's manufacturing environment is composed of three main techniques, subtractive manufacturing (milling/turning), formative manufacturing (casting/forging), and additive manufacturing (rapid-manufacturing/3D printing). Additive manufacturing (AM) is an automated fabrication technique that uses computer-aided designs to generate three-dimensional objects layer-by-layer. In contrast to the other manufacturing techniques, AM provides a unique way to create parts with high complexity and variability in geometrical features. Furthermore, the complexity of the component's shape has a negligible impact on fabrication cost or time.

AM processes can be defined using a variety of perspectives. For instance, they can be classified based upon the type of raw material (metal, plastic, ceramic, resin, powder) or the type of working principle used for layer generation (photopolymerization, material extrusion, sheet lamination, powder bed fusion, etc.) On the other hand, AM machines can be put into three categories, "fabbers," office machines, and shop-floor machines.¹ Fabbers are small, low-cost modelers for personal use, often located at home or co-working spaces. Office machines are slightly more sophisticated but characterized by easy operation, minimal maintenance, and easy waste disposal. Shop-floor machines are highly sophisticated machines used for manufacturing, prototyping, and tooling that require intricate logistics, skilled labour, and complex post-processing.¹ In this dissertation, the use of AM machines will refer to shop-floor equipment, while the term 3D printer will refer to both fabbers and office machines.

1.2 Additive manufacturing in the medical industry

The medical/dental sector represents ~17% of the AM industry, where both 3D printers and AM machines play an essential role.² The use of AM in the health care industry can be classified into four categories: (1) treatment planning, (2) bio-printing/tissue

engineering, (3) non-invasive medical devices, and (4) invasive medical devices.³ For each type of application, a specific AM technology and material will be more suitable. Organ models printed for visualization, surgical rehearsal, or non-invasive interventions do not require bio-compatible materials. In contrast, medical devices printed for invasive procedures (*e.g.*, a customized tracheobronchial stent) and tissue-engineering constructs (*e.g.*, a collagen scaffold) need to be biocompatible and incur minimal to no tissue response.

3D printers are frequently used for non-invasive applications. For example, resin-based printers are used in dental offices to produce orthodontic appliances (*i.e.*, retainers, aligners, and expanders).^{4,5} Plastic deposition printers have been used to manufacture durable and light exoskeletons for patients who suffer from stiff joints or underdeveloped muscles.⁵ AM machines are frequently used for applications that require biocompatible materials or biomedical components. Powder bed fusion (PBF) has been used to produce titanium (Ti6Al4V) scaffolds that support the growth of osteoblasts (bone cells).⁶ Ti6Al4V parts produced using PBF can be fine-tuned to match strict mechanical properties that are important for musculoskeletal applications.⁶ For instance, functionally graded structures are designed to match the radially dependent porosity of long bones.⁷ Aside from PBF, other AM technologies commonly used in the medical/dental field include stereolithography (SLA), selective laser sintering (SLS), and fused deposition modelling (FDM).⁸

Biocompatible materials used in AM machines include polymers, composites, ceramics, and metals.^{9,10} Biocompatible polymers and composites are the materials of choice for tissue engineering and regenerative medicine, while biocompatible ceramics and metals are the materials of choice for medical implants and prostheses.⁹ The most commonly used biocompatible ceramics are alumina, zirconia, and hydroxyapatite;¹⁰ the most used metallic biomaterials are 316L stainless steel, Ti6Al4V titanium-aluminum-vanadium alloys, and CoCrMo cobalt-chromium-molybdenum alloys.¹¹ For this dissertation, the term medical component refers to medical implants or prostheses made of biocompatible metals.

AM processes are driven by various technology-specific parameters. The correct selection of these parameters defines the success of the manufacturing process by ensuring quality, consistency, and reliability.⁵ For a printing job to be considered successful, it needs to satisfy the following criteria: the part has to be defect-free and must have the same material properties as the parent material, it must have geometric fidelity when compared to the computer-assisted design (CAD), and it must satisfy the prescribed functional requirements (*e.g.*, microstructure, surface roughness, and mechanical properties).

1.2.1 Additive manufacturing of bio metallic medical components

Recent advancements in AM and accelerated developments of biomedical materials have increased the interest in producing medical components using metallic biomaterials. AM facilitates the fabrication of custom-made patient-specific implants and components with optimized topologies. Custom implants can be designed to match the patient's anatomy using volumetric data acquired with clinical MRI or CT machines.^{2,8,12} Topology optimization is a powerful technique for finding the ideal material distribution within a part.¹³ Due to their stringent requirements, some of these biomedical components can only be manufactured using AM machines; and others benefit from being produced with AM, thanks to the inherent characteristics of the technology.¹⁴ Table 1-1 highlights the benefits of AM when compared to other manufacturing methods that apply to the production of medical components.¹

Table 1-1: Advantages of AM in the production of bio metallic medical components.

	AM	Other methods
1. Require tools and fixtures	No	Yes
2. Lead time for fabrication	Low	High
3. Spectrum of applications	High	Medium
4. Operator intervention	Low	High
5. Fabrication of functionally	Easy	Complex
6. Amount of noise and	Low	High
7. Cost-complexity ratio	Constant	Complexity-dependent

The main AM technologies used to produce bio-metallic medical components are powder bed fusion (PBF), directed energy deposition (DED), sheet lamination, metal extrusion, and binder jetting. From these technologies, PBF and DED are the most relevant and widely used. PBF uses a metal powder that is selectively melted or sintered using an energy source to generate the desired layer shape; PBF machines are classified in laser (LPBF) or electron beam (EPBF) depending on the used energy source.¹⁵ DED uses a concentrated energy source that interacts with one or multiple nozzles that feed the material needed for each layer. Other novel techniques involve the combination of metal printing with other materials (*i.e.*, multi-material AM). When used appropriately, AM processes are able to produce parts with mechanical properties similar or even superior to other manufacturing techniques. Table 1-2 summarizes some of the key mechanical properties of the most used medical-grade metals fabricated using AM and other relevant techniques.¹¹

Table 1-2: Key mechanical properties of the most used medical-grade metals fabricated using AM.

	316L			Ti6Al4V			CoCrMo		
	LPBF	DED	Forgin	LPBF	DED	Casting	LPB	EPBF	Casting
Ultimate tensile strength (MPa)	480-760	533-685	450-818	973-1407	920-1163	934-1173	951-1308	1450	591-759
Yield strength (MPa)	350-640	235-485	150-230	885-1333	850-1105	862-999	562-884	510	296-568

1.3 Common characteristics of AM-fabricated biomedical components

AM-fabricated biomedical components share common characteristics that can be exploited when designing quality assurance and quality control systems. In particular, these characteristics allow the use of low-energy, cost-effective, x-ray based, non-destructive testing (NDT) and are the following:

- **Size:** the majority of prosthetic devices that are produced with AM for clinical applications restore underlying anatomy that is relatively small. For example, a cranial plate covering a large area of the skull ($> 100 \text{ cm}^2$)¹⁶ will only measure 15 by 7 by 2 cm. Fig 1-1 shows an example of a cranial plate imaged using 80 kVp with a preclinical CT scanner. In contrast, prosthetic devices used to restore large anatomic defects are usually manufactured using conventional techniques.
- **Porosity:** AM allows the production of highly porous medical components, thanks to the introduction of lattice structures in their design. These porous lattices reduce the density and weight of the medical component, and can be used to promote osteointegration, or for drug delivery.^{7,17} Furthermore, the size and shape of the lattice can be used to modify the mechanical properties of the part, for example, to match the modulus of elasticity of the underlying bone.¹² Note that the overall porosity of the part should not be confused with the porosity of

the metal struts of the lattice unit. To avoid future confusion the term micro- porosity will be used to describe any possible voids that could be introduced in the part but that are not part of the macroscopic, prescribed design of the component. Current, AM technologies are able to reduce this unintended micro- porosity percent to less than 1%.

- Biomaterial: titanium (Ti4Al6V), cobalt-chrome (CoCrMo), and stainless steel (316L) are the most widely used alloys for biomedical applications. From them, titanium alloy remain the material of choice due to its long-term cost effectiveness and unique fatigue and corrosion resistance.¹⁸ Titanium alloys are also the biologically compatible metals with the lowest mass-attenuation coefficient, which makes Ti4Al6V parts less radio-opaque and easier to interrogate at relatively low x-ray energies (~ 80 kVp).

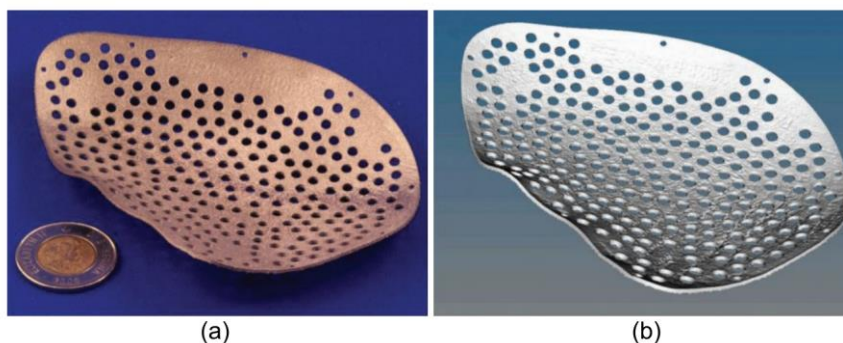


Fig 1-1. (a) titanium cranial plate, with (b) CT scan data at 80 kVp (GE Ultra, 150 μm , 16 s scan).

Photon starvation, which can occur with highly attenuating materials, can cause severe artifacts in non-destructive testing applications using computed tomographic techniques (CT). This occurs when the x-ray beam travels through a large amount of a highly attenuating material, and therefore insufficient photons reach the imaging detector. To avoid these artifacts, industrial NDT CT scanners are equipped with high-energy x-ray sources that have a greater penetration power. In this work, we hypothesize that the previously mentioned characteristics (size, porosity, and biomaterial) reduce the photon penetration requirements for successful image-based, NDT of biomedical parts. This is

achieved by reducing the total length path through a relatively low-attenuating material. More details about image-based NDT are described below.

1.4 Non-destructive testing

Non-destructive testing (NDT) allows the inspection of materials and structures without compromising their physical integrity and therefore protecting their future usefulness. Effective NDT mainly provides information related to the structure of the material, isolated discontinuities (voids, cracks, porosity, delamination), and three-dimensional internal and external measurements. It could also provide information about the mechanical and physical properties of a part and its chemical composition.¹⁹

Although 1D and 2D NDT methods are commonly used, recent developments in 3D, volumetric, x-ray-based imaging has resulted in a rapid shift towards fully three-dimensional characterization of parts and materials using x-ray computed tomography (CT). Current, state-of-the-art, industrial CT scanners are equipped with high-energy x-ray sources, and are able to produce images with high accuracy and resolution ($< 100 \mu\text{m}$). These systems were originally developed for industrial applications in the automotive and space sectors.¹⁹ Currently, the use of image-based NDT has been proposed as an effective tool to detect nonidealities in parts produced using AM.²⁰

CT scanners, for NDT, produce an image of an object placed in a high precision rotary stage between the x-ray source and an x-ray detector. In most cases, the x-ray unit generates a conic beam of polychromatic (*i.e.*, with various energies) photons that interrogate the object, generating a 2D projection image. The object is then rotated, one angular increment at the time, covering a full rotation 360° , or using a limited-angle approach (*e.g.*, 180° plus fan angle).²¹ The collected projection images are then used to reconstruct the 3D data of the object using various reconstruction algorithms. The algorithm described by Feldkamp *et al.*²² is one of the most commonly used methods for circular cone beam tomography, due to its simplicity and ease of implementation. The reconstructed volume consists of discrete volumetric elements (*i.e.*, voxels) that represent the electron density at each point of the field-of-view using grey scale values.

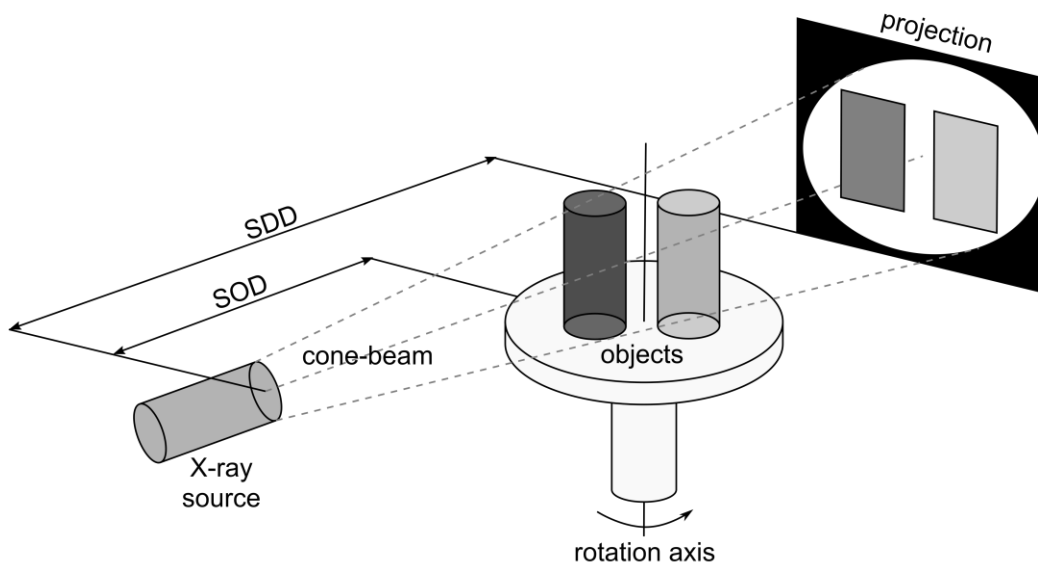


Fig 1-2. Geometry of a cone-beam CT system. The diagram shows the main parameters of a stationary source design. (SOD, source–object distance and SDD, source–detector distance).

1.4.1 Cost-effectiveness and alternatives

Industrial CT scanners for NDT present high accuracy and quality thanks to being equipped with micro-focus x-ray sources, capable of producing photons with energies >225 kVp, and high-quality flat-panel x-ray detectors. These highly specialized components, and their required supporting hardware, make these scanners expensive to purchase and operate.²³ For example, maintaining the micro focus of an x-ray source operating at high energy potentials might require sophisticated and expensive cooling systems, and the shielding required for x-ray safety at high energies might increase the weight of the scanner to the point of needing costly infrastructure.

In the medical sector, where the cost of testing has to be proportionate with the cost of the medical component, routine NDT using these scanners might become prohibitively expensive.²³ Therefore, alternatives to reduce the cost of scanning need to be explored. We propose to increase the cost-effectiveness of imaging-based NDT of medical AM components by developing a custom-built system that will operate at lower energies and

will be equipped with less costly x-ray detector technologies (*e.g.*, lens-coupled x-ray detectors).

1.4.2 Lens-coupled x-ray detectors

During the early stages of development of x-ray detectors, the idea of capturing the light emitted by a scintillating screen using traditional optics (*i.e.*, lenses) and a digital camera was explored.²⁴⁻²⁷ At that time, the light sensitivity of these lens-coupled detectors was not sufficient to ensure that the detector's noise was dominated by photon noise instead of the inherent noise of the detector (or due to a secondary "quantum sink"). This caused a loss of interest towards lens-coupled systems favoring the development of fiber-optic coupled, and flat-panel digital radiography detectors.

To understand the lack of light sensitivity of early lens-coupled systems, we must analyze two main aspects of this technology. First, the light collection efficiency of a lens is determined by its effective f-number (N_w).

$$N_w = \left(1 - \frac{m}{P}\right) \frac{f}{D} \quad (1.1)$$

where m is the lens's magnification for an object, P is the pupil magnification, f is the focal length, and D the diameter of the entrance pupil. The lens magnification (m) can be calculated using:

$$m = -\frac{q}{p} \quad (1.2)$$

where, q is the distance from the lens's back plane to the image, and p is the distance from the object to the lens's frontal plane to the image. We can evaluate that in order to image a fixed-size field-of-view (FOV) with a large aperture lens into a smaller fixed-size detector we can move the lens and the detector to increase p and decrease m . Unfortunately, this will decrease the light efficiency of the system, leaving only two options to improve it. One is to use a lens with a larger aperture, and the second is to increase the size of the detector. The other closely linked limitation of earlier stages of lens-coupled detectors was the small size of the camera's sensor, which limited the use of

this technology for small-scale applications.^{24,28} Additionally, the charge-coupled devices (CCD) used to digitize the captured light were more susceptible to noise than modern detector technology, which further decreased the quality of the images.

Recent advancements in digital photography and sensor technologies have made it possible to revisit the use of lens-coupled detectors for advanced, large FOV x-ray imaging applications.^{29,30} These include the development of consumer-grade, single-lens, reflex digital single-lens reflex (dSLR) cameras with large, full-frame, 36 by 24 mm image sensors, and the implementation of complementary metal oxide semiconductor (CMOS) technology rather than CCD. Sensors using CMOS technology have pixels with individual circuitry for noise control, charge integration, and readout, which significantly improves the sensor's noise susceptibility. Furthermore, modern CMOS sensors include an active-reset circuit that can operate in parallel and further reduce the levels of readout noise. Finally, since thermal noise has a variance that is proportional to bandwidth, the pixel-by-pixel parallel processing of this type of sensor makes them less susceptible to thermal noise, as well.

In order for these lens-coupled detectors to be a feasible technology for CT, the sensitivity (n_s) of the system, in terms of electrons produced per x-ray photon, has to be larger than unity (*i.e.*, $n_s \geq 1$). The sensitivity n_s can be described by the expression:

$$n_s = g_1 g_2 n_c \quad (1.3)$$

where, g_1 is the conversion factor of the scintillating screen (*i.e.*, the number of optical photons emitted by absorbed x-ray photon), g_2 is the optical coupling efficiency of the lens, and n_c is the quantum efficiency of the detector (*i.e.*, the number of electrons generated by captured light photons).³¹

For a single lens system, the coupling efficiency is given by Miller³² and Maidment and Yaffe³³

$$g_2 = \frac{t}{4F^2(m+1)^2} \quad (1.4)$$

where t is the optical transmission factor for the lens, F is the ‘f-number’ of the lens, and m is the demagnification factor from the phosphor screen to the camera’s sensor. Therefore, for a lens-coupled system with $t = 0.8$, $F = 1.4$, and $m = 7$, the coupling efficiency will be 0.16%. Since most $\text{Gd}^2\text{O}_2\text{S}$ phosphor screens have a conversion factor around 7.5% ($g_1 = 0.075$) and most full-frame CMOS sensors a quantum efficiency of 60% ($n_c = 0.6$), in a system with these characteristics for each x-ray photon at least 2 electrons will be recorded at the sensor. This calculation makes us understand the importance of reducing demagnification by using a full-frame optical image sensor, as this number will be <1 if demagnification was larger than 10.

The development of a CT scanner, for NDT, equipped with this type of detector technology could result in a significant improvement in the cost-effectiveness of the quality control procedure, as the costs associated with these technologies are relatively low when compared with fiber-optic coupled or flat-panel detectors. There are several consumer-grade dSLR cameras, equipped with high-quality fast lenses, which can be purchased for under \$ 7500 and will be able to image fields-of-views up to 36 by 24 cm with a light sensitivity > 1 .

1.4.3 Image artifacts and limitations

Despite the choice of the detector technology included in a cone-beam CT scanner for NDT, this imaging modality is susceptible to a variety of non-idealities that are expressed in the form of artifacts in the CT reconstruction. Other artifacts can be caused by a miscalibration of the scanner’s geometry, but in this dissertation, we are assuming that the systems are well calibrated, and therefore we will discuss artifacts caused by the physics of x-ray imaging and the data acquisition process only. The most relevant sources of artifacts in the context of industrial NDT are beam hardening, scattered radiation, under-ranging, and fixed-pattern noise. These artifacts reduce the diagnostic capabilities and the quantitative nature of the NDT procedure, and therefore, all the available efforts to reduce them or eliminate them need to be considered. The most common artifacts in industrial CT are:

- Cupping artifacts: cupping artifacts are caused by both beam hardening and scattered radiation.³⁴ When imaging a cylinder of water, for example, both

phenomena cause an increase in the signal measured in the projection images towards the centre of the cylinder. This leads to a reduced CT number in the center of the reconstructed cylinder causing a radial shading artifact. Beam hardening causes cupping artifacts due to the polychromatic nature of the x-ray beam. For this case, the mean energy of the polychromatic x-ray beam increases as the low-energy photons are attenuated by the material, causing an underestimation of the material's electron density, predominantly for long path lengths through the material. Scattered radiation also causes cupping artifacts due to the shape of the scattered field, which is usually more intense in the center of the imaged object, again increasing the signal measured in the projection images in this area, and causing an underestimation of the material's electron density.

The research areas involved in the removal of cupping artifacts in CT caused by both beam hardening and scatter radiation are quite active, with new approaches and methodologies being published yearly. In this dissertation we will provide a brief framework for the reduction of cupping artifacts caused by beam hardening, and elaborate in the use of hardware based techniques for scatter radiation removal.

Beam hardening correction

The methods to correct for beam hardening can be classified into three classes: physical filtration, dual-energy methods, and algorithmic corrections.³⁵ Physical filtration involves using a thin amount of a highly attenuating material (*e.g.*, copper) to increase the mean energy of the polychromatic x-ray beam before interacting with the scanned object. Unfortunately, this filtration does not produce a monochromatic x-ray beam and beam-hardening artifacts might still be present in many cases.³⁴ Imaging the object with a dual-energy technique and obtaining two polychromatic x-ray sums makes it possible to better estimate the monochromatic x-ray sum than can be obtained from a single polychromatic measurement.³⁶ Theoretically, this dual-energy correction technique is robust, but due to the requirement of a dual-energy (*i.e.*, two x-ray sources, two detectors, or

two scans) setup the application of this technique is limited. Beam hardening can also be corrected algorithmically. For these cases, the correction can be applied to the data before or after CT reconstruction. Algorithmic preprocessing of the projection data can be accomplished by implementing a correction using a curve fit of data empirically obtained, using a calibrating object with a known material and thickness.³⁷⁻³⁹ In this dissertation, the effects of beam hardening were minimized using both filtration of the x-ray beam, and using the logarithmic correction described by Edey *et al.*³⁷

Scatter radiation correction.

Scatter radiation considerably affects cone-beam CT geometries when compared to single-slice or fan-beam geometries.⁴⁰ In some cases, scatter fluence, at the detector level, can exceed primary fluence by an order of magnitude if no scatter mitigating techniques are employed. For NDT, cone-beam geometries are desirable as they provide a more cost-efficient approach for data collection, with the drawback of increased sensitivity to scatter due to the large fields-of-view. Scatter radiation can be corrected using two distinct approaches: hardware techniques for scatter suppression and software techniques for scatter compensation.^{40,41} This being said, for practical applications, scatter radiation has to be suppressed to low levels by hardware pre-sample (*e.g.*, bow-tie filters) and post-sample (*e.g.*, anti-scatter grids) devices in order for software techniques to achieve reasonable results.⁴¹ The field of software estimation techniques for scatter correction is very active and is beyond the scope of this dissertation. In this work, we have decided to focus on a new class, described below, of post-sample devices for scatter suppression for flat-panel cone-beam CT – two-dimensional, focused, anti-scatter grids.

- Streak artifacts: dark and bright streaks that appear along the direction of a highly attenuated path can be caused by a variety of phenomena, including, beam hardening, scattered radiation, under-ranging, and Poisson noise.⁴² These artifacts are quite common for scenarios where the imaged object has various materials with a wide range of electron densities. For those cases, the dark and bright

streaks are produced between objects with high attenuation properties. Beam hardening and scattered radiation can also produce streaks parallel to the long axis of a single high-attenuation object.⁴³ Streak artifacts can be minimized by implementing beam hardening and scatter radiation correction techniques and methods to increase the dynamic range of the system (*i.e.*, to avoid under-ranging), or using iterative reconstruction methods.

In some cases, for example, when severe under-ranging or photon starvation occurs, the intensity of these streak artifacts is so large that the image becomes completely useless.⁴⁴ This extreme case of streak artifacts is caused by the dominance of detector noise levels in low signal regions of the projection images. This low signal-to-noise ratio is further exacerbated by the non-linear nature of the logarithmic conversion used prior to CT reconstruction. In this dissertation, described below, we introduce a method to increase the dynamic range and therefore mitigate photon starvation artifacts in CT-based NDT.

- Ring artifacts: The individual elements (*i.e.*, pixels) of X-ray detectors do not always respond in the exact same way to incident photons. These pixel gain variations produce fixed-pattern noise in the projection images, leading to ring artifacts in the reconstructed CT images.⁴⁵ Fixed-pattern noise can also be produced by the dark-field of the detector, and any structural defect at the detector plane due to manufacturing constrains. Anti-scatter grids are another source of ring artifacts, as their septa might modify the response of the shadowed detector elements.⁴⁶ In general, ring artifacts can be greatly minimized using a flat-field (*i.e.*, gain and offset) correction, where a map of the individual response of each pixel is used to normalize the response of the entire detector.⁴⁵ Nevertheless, beam hardening, under-ranging, scattered radiation, and noise all reduce the effectiveness of the correction, and in some cases additional ring-removal techniques have to be implemented. One example of such a technique is the use of a combined wavelet and Fourier stripe removal filter.⁴⁷ In this implementation, the CT projection images are transferred to the Radon space (*i.e.*, sinograms) where the fixed-pattern noise (which causes ring artifacts), can be isolated in the form of vertical stripes. After applying the wavelet-Fourier filter in the Radon

space, images can be transferred back to their original format, and used to generate ring-free reconstructions.⁴⁷ Another alternative is to implement more complex methods for flat-field correction, which can account for some of the non-idealities of traditional methods.⁴⁵

As previously described, cone-beam CT (CBCT) has proven to be an effective tool for NDT of metal parts. In this context, scanners designed for NDT of a wide range of materials and large fields-of-views are often called industrial micro-CT scanners. These scanners are susceptible to artifacts caused by beam hardening, scattered radiation, under-ranging, and ring artifacts. Furthermore, due to the cost of operation and purchase, these scanners are often not cost-effective for routine non-destructive testing of medical components. In this dissertation we describe the development of a low-cost dedicated scanner for NDT of medical components and two methods to reduce the detrimental effects of scattered radiation and under-ranging in CBCT. For scatter removal we describe the use of a novel anti-scatter grid design, and for under-ranging the use of high-dynamic range radiography.

1.5 Anti-scatter grids for cone-beam CT

Cone-beam CT (CBCT) systems, in contrast with fan-beam or multi-slice CT, are more susceptible to image quality loss (*e.g.*, reduced image contrast) caused by scattered photons.^{40,41} Scattered photons, in contrast to primary photons, are x-rays that upon interaction with the imaged sample are diffracted from their original path.⁴⁸ Typical anti-scatter grids are devices placed directly in front of the x-ray detector that are designed with thin septa made of a highly attenuating material (*e.g.*, lead) and separated by an interspacer made of a very low attenuating material (*e.g.*, fibre); this approach will selectively attenuate scattered photons. The use of these devices produces a reduction in the scatter-to-primary ratio (SPR).

Anti-scatter grids have been utilized in large field-of-view radiography since 1913 when Bucky described the first design.⁴⁹ Although this two-dimensional grid was able to reduce the SPR and improve image contrast the shadows of the grid septa in the image were noticeably visible. In 1920, Potter solved this limitation by modifying the geometry

of the grid to be only one-dimensional (*i.e.*, with uni-directional parallel lead strips) and by moving the device perpendicular to the direction of the strips during image acquisition in order to successfully fade the shadows of the grid septa.⁵⁰ Since then, the field of scatter rejection using anti-scatter grids has evolved greatly.

Two important concepts for the description of an anti-scatter grid are its primary and scatter transmission properties. The perfect grid will have a primary transmission of 100% with a 0% scatter transmission.⁵¹ Modern designs for anti-scatter grids take into account features that improve the transmission characteristics of the grid while maintaining their scatter rejection capabilities. In general, grid primary transmission is affected by: (1) the grid septa, which directly blocks primary photons, and (2) interseptal fillers, which attenuate the primary photons, reducing their fluence at the detector.⁵¹ Traditional non-focused grids, which have grid septa perpendicular to the detector, exacerbate grid shadows as the angle of incidence of the primary photons decreases due to the conical shape of the x-ray beam. Therefore, focusing or tilting the grid septa to conform with the geometry of the x-ray beam is desirable to increase the primary transmission of the grid. Primary transmission can also be improved by using materials with very low x-ray attenuation (*e.g.*, carbon fibre) or by removing the need for interseptal support, which is usually necessary for grids made of lead. Using materials with a low x-ray attenuation, to improve primary transmission, is limited by the height of the grid's septa. For example, modern carbon-fibre-spaced anti-scatter grids only achieve a primary transmission of 65 to 70% when the grid septa are 100 μm thick and 10 mm tall.⁵² Finally, primary transmission can be improved by reducing the thickness of the grid septa as much as possible. This last strategy to increase primary transmission is highly dependent of the grid manufacturing technique. Recent developments in additive manufacturing allow the fabrication of two-dimensional, focused, anti-scatter grids (Fig 1-3) with thin metal septa ($\sim 100 \mu\text{m}$), and without the need for interseptal support.^{45,46,51,53-56}

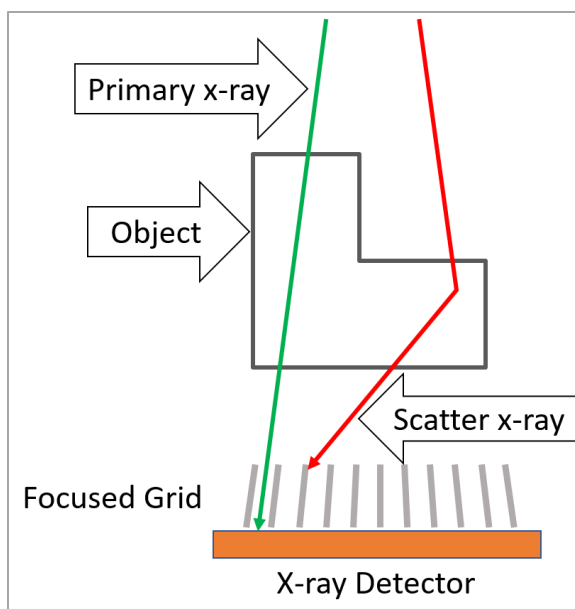


Fig 1-3. Illustration of a focused anti-scatter grid. Each grid channel has a unique angle aligned towards the focal spot of the CBCT geometry.

There are a few important concepts for the design of two-dimensional, focused, anti-scatter grids (2D-ASGs) that have an impact in both primary and scatter transmission. The first concept is the grid ratio, which is defined as the ratio between the height of the grid septa and the width of the interseptal space. Grid ratio reduces scatter transmission by restricting the path of scattered photons through the grid channels.⁵³ The second concept, grid pitch, is defined as the total size of a grid unit, which is equal to the interseptal space plus the septal thickness. An increase in grid pitch improves primary transmission at the expense of requiring a taller grid to maintain grid ratio. Generally speaking, traditional grids are designed to have grid ratios between 10-20 with grid pitches in the order of a few millimeters (1-5 mm). Experimental data has shown that 2D-ASGs provide greater scatter rejection than 1D-ASGs at lower grid ratios (~ 10) and can offer effective improvements in image contrast while maintaining a primary transmission $> 70\%$, which is the average transmission for a traditional 1D-ASG.

As previously mentioned, one of the limitations of the use of anti-scatter grids has to do with the introduction of septal shadows in the projection images (*i.e.*, grid line artifacts). For the case of two-dimensional focused anti-scatter grids, the use of moving

mechanisms is not as effective as for one-dimensional grids. This is because moving the 2D-ASG will cause a focal misalignment between the grid septa and the x-ray source, which will reduce primary transmission. It is also challenging to implement a motion pattern that will effectively “blur” septa in two dimensions; simple linear motion is not sufficient. For these reasons, grid line artifacts (GLA) caused by 2D-ASGs should preferably be removed using image processing methods. Failure to remove GLA will introduce fixed-pattern noise into the projection images, which will cause severe ring artifacts in the CT reconstructions.⁴⁶

The fabrication of modern 2D-ASGs is closely linked to AM of highly attenuating metals (*e.g.*, tungsten). This is because the grid material plays a key role when describing the scatter rejection capabilities of the device.^{51,54} Recent research has shown that for high-energy applications tungsten is the material of choice due to its high electron density.^{51,54} In this dissertation we explore the use of cobalt-chrome as an alternative for applications where the x-ray energies are not in the high end of diagnostic energies (~ 80 kVp). We describe the design, manufacturing, implementation, and evaluation of a cobalt-chrome, 10:1 grid ratio, large-area, 2D-ASG for scatter reduction in CBCT. We exploit the maximum printing area available in one of the metal 3D printers available in our facilities (AM-400; Renishaw plc, New Mills Wotton-under-Edge, UK).

1.6 High-dynamic range radiography

One of the strategies for making image-based NDT more cost-effective in biomedical applications is the use of x-ray sources operating at lower energy potentials (~ 80 kVp). As previously described, most medical devices will have shared characteristics that reduce penetration requirements of the x-ray beam. Nevertheless, the use of low-energies increases the potential for photon-starvation and under-ranging artifacts. If a fabricated component has large portions of solid metal (even if it has a low electron density) the pixels in the projection images may become obscured, producing severe artifacts in the reconstructed CT volume.⁵⁷ Intuitively, the expression:

$$I_x = I_0 e^{-\mu x} \quad (1.5)$$

where I_x is the intensity at depth of x in a material, I_0 is the original intensity, and μ is the linear attenuation coefficient, ensures that increasing the integration time (ms) or the exposure (mA) should improve the signal in the obscured region of the image. Unfortunately, this will overexpose the pixels where there is no object in the field-of-view, due to the finite dynamic range of the x-ray detector.⁵⁷

High-dynamic-range radiography can be utilized to extend the dynamic range of the detector, by acquiring two sets of data, one with a low integration time/exposure, and a second with a large integration time/exposure. The valid data in both images can be used to generate a composite image with an extended dynamic range and reduced under-ranging artifacts.⁵⁷⁻⁵⁹

1.7 Objectives

The objectives of this thesis are to:

1. Develop an optimized, cost-effective, micro-CT system for non-destructive testing of titanium alloy biomedical components using: (1) an 80 kVp portable x-ray source; and (2) a scintillating-screen, lens-coupled to a dSLR camera.
2. Design, manufacture, implement, and evaluate a large-area, highly collimated, anti-scatter grid, using additive manufacturing in cobalt-chrome, for the purpose of scatter reduction in flat-panel detector based micro-CT systems.
3. Develop a protocol to reduce image artifacts due to photon starvation, when imaging highly attenuating materials in cone-beam CT, by implementing multiple exposure high-dynamic-range radiography.

1.8 Thesis outline

This thesis describes the design of protocols, and the fabrication of apparatus for high-quality, cost-effective, non-destructive testing of biomedical components fabricated using additive manufacturing using CT imaging. In this work we also include the development of an anti-scatter device with the potential to improve image quality in CBCT by removing scatter-related image artifacts, and the description of a high-dynamic range

radiography method to reduce CT image artifacts caused by photon-starvation and under-ranging.

Chapter 2: Cost-effective micro-CT imaging of medical components fabricated with additive manufacturing - describes the design, fabrication, and evaluation of a low-cost, micro-CT system. The system cost was minimized by describing the potential use of an off-the-shelf, portable, low-energy (80 kVp) x-ray source. The cost was further reduced through the application of a consumer-grade, dSLR camera that was lens-coupled to a phosphor scintillating screen functioning as the detector and digitalization system of the scanner. This original research exploits recent advancements in digital photography and full-frame digital detectors to revisit the concept of lens-coupled x-ray radiography. Additionally, it presents a novel strategy to maximize light sensitivity by using a tilted-detector geometry than permits the camera to operate with as large an aperture as possible. This tilted detector geometry allows the camera to reside on the same side of the scintillator as the source, which removes the effects of x-rays directly incident on the camera CMOS sensor. Finally, the effect of direct x-ray capture on the camera sensor is also reduced in this configuration.

Chapter 3: High-dynamic-range micro-CT for non-destructive testing of titanium parts fabricated using additive manufacturing (AM) - relatively low-energy (*i.e.*, ~80 kVp) micro-CT is a viable method for non-destructive testing of AM objects made of titanium and other relatively-soft metals. However, this technique may still suffer from image artefacts due to photon starvation in thick objects. This original research describes a novel implementation of high-dynamic-range radiography used to ameliorate the effects of photon starvation in micro-CT imaging. We describe and implement a method employing variable exposure time for this purpose. The method was evaluated using a set of novel AM titanium phantoms. One of the phantoms was designed to test the maximum x-ray penetration through AM titanium objects. A second set of phantoms – employing a gyroid-based geometry – was conceived, designed, and manufactured to evaluate the effect of porosity.

Chapter 4: 3D printed large-area grid for scatter reduction in cone-beam CT - using a bench-top scanner developed in house; this chapter describes the improvements in

image quality measured by contrast-to-noise ratio and reduction of linearity-based cupping artifacts, achieved by using a large-area, anti-scatter grid, manufactured using AM. This original research describes the challenges and novel strategies involved in the design, manufacturing, implementation, and evaluation of a cobalt-chrome, anti-scatter grid in flat-panel-based, cone-beam CT. We describe the challenges and solutions for the additive-manufacturing of a large-area 2D-ASG. We also describe the post-processing and image corrections required to remove image artifacts, such as rings, associated with the 2D-ASG. Improvements in image quality were assessed using a comprehensive micro-CT quality-assurance imaging phantom.

Chapter 5: **General discussion and conclusions** - this chapter contextualizes the previous chapters' overall conclusions and the overall accomplishments of the various experiments. It involves an in-depth analysis of the practical implementation of cost-effective non-destructive testing in additive manufacturing of medical devices and components. It lays out the limitations of these technologies and any future work required in the field.

1.9 References

1. Srivastava M, Rathee S, Maheshwari S, Kundra T. *Additive Manufacturing: Fundamentals and Advancements*. CRC Press; 2019.
2. Javaid M, Haleem A. Additive manufacturing applications in medical cases: A literature based review. *Alexandria Journal of Medicine*. 2018;54(4):411-422.
3. Yan Q, Dong H, Su J, et al. A review of 3D printing technology for medical applications. *Engineering*. 2018;4(5):729-742.
4. Pillai S, Upadhyay A, Khayambashi P, et al. Dental 3D-Printing: Transferring Art from the Laboratories to the Clinics. *Polymers*. 2021;13(1):157.
5. Chua CK, Wong CH, Yeong WY. *Standards, quality control, and measurement sciences in 3D printing and additive manufacturing*. Academic Press; 2017.
6. Lowther M, Louth S, Davey A, et al. Clinical, industrial, and research perspectives on powder bed fusion additively manufactured metal implants. *Additive Manufacturing*. 2019;28:565-584.

7. Mahmoud D, Elbestawi MA. Lattice structures and functionally graded materials applications in additive manufacturing of orthopedic implants: a review. *Journal of Manufacturing and Materials Processing*. 2017;1(2):13.
8. Liu Y, Wang W, Zhang L-C. Additive manufacturing techniques and their biomedical applications. *Family Medicine and Community Health*. 2017;5(4):286-298.
9. Chua CK, Leong KF, An J. Introduction to rapid prototyping of biomaterials. In: *Rapid prototyping of biomaterials*. Elsevier; 2020:1-15.
10. Ferrage L, Bertrand G, Lenormand P, Grossin D, Ben-Nissan B. A review of the additive manufacturing (3DP) of bioceramics: alumina, zirconia (PSZ) and hydroxyapatite. *Journal of the Australian Ceramic Society*. 2017;53(1):11-20.
11. Vandenbroucke B, Kruth JP. Selective laser melting of biocompatible metals for rapid manufacturing of medical parts. *Rapid Prototyping Journal*. 2007.
12. Li C, Pisignano D, Zhao Y, Xue J. Advances in medical applications of additive manufacturing. *Engineering*. 2020.
13. Fousová M, Vojtěch D, Kubásek J, Jablonská E, Fojt J. Promising characteristics of gradient porosity Ti-6Al-4V alloy prepared by SLM process. *Journal of the mechanical behavior of biomedical materials*. 2017;69:368-376.
14. Gibson I, Rosen D, Stucker B, Khorasani M. Design for additive manufacturing. In: *Additive manufacturing technologies*. Springer; 2021:555-607.
15. Gibson I, Rosen DW, Stucker B, Khorasani M. Additive manufacturing technologies. In: Vol 17. Springer; 2021:125-170.
16. Dean D, Min K-J, Bond A. Computer aided design of large-format prefabricated cranial plates. *Journal of Craniofacial Surgery*. 2003;14(6):819-832.
17. Mohammed A, Elshaer A, Sareh P, Elsayed M, Hassanin H. Additive manufacturing technologies for drug delivery applications. *International journal of pharmaceutics*. 2020;580:119245.
18. Harun W, Kamariah M, Muhamad N, Ghani S, Ahmad F, Mohamed Z. A review of powder additive manufacturing processes for metallic biomaterials. *Powder Technology*. 2018;327:128-151.
19. Kastner J, Heinzl C. X-ray computed tomography for non-destructive testing and materials characterization. In: *Integrated Imaging and Vision Techniques for Industrial Inspection*. Springer; 2015:227-250.

20. Khosravani MR, Reinicke T. On the use of X-ray computed tomography in assessment of 3D-printed components. *Journal of Nondestructive Evaluation*. 2020;39(4):1-17.
21. Silver MD. A method for including redundant data in computed tomography. *Medical Physics*. 2000;27(4):773-774.
22. Feldkamp LA, Davis LC, Kress JW. Practical cone-beam algorithm. *Josa a*. 1984;1(6):612-619.
23. du Plessis A, le Roux SG, Guelpa A. Comparison of medical and industrial X-ray computed tomography for non-destructive testing. *Case Studies in Nondestructive Testing and Evaluation*. 2016;6:17-25.
24. Kim HK, Ahn JK, Cho G. Development of a lens-coupled CMOS detector for an X-ray inspection system. *Nuclear Instruments and Methods in Physics Research Section A: Accelerators, Spectrometers, Detectors and Associated Equipment*. 2005;545(1-2):210-216.
25. Madden TJ, McGuigan W, Molitsky MJ, Naday I, McArthur A, Westbrook EM. Lens-Coupled CCD detector for x-ray crystallography. Paper presented at: 2006 IEEE Nuclear Science Symposium Conference Record2006.
26. Tate MW, Chamberlain D, Gruner SM. Area x-ray detector based on a lens-coupled charge-coupled device. *Review of scientific instruments*. 2005;76(8):081301.
27. Uesugi K, Hoshino M, Yagi N. Comparison of lens-and fiber-coupled CCD detectors for X-ray computed tomography. *Journal of synchrotron radiation*. 2011;18(2):217-223.
28. Lee SW, Kim HK, Cho G, Shin YH, Won YY. A 3-D X-ray microtomographic system with a CMOS image sensor. *IEEE transactions on nuclear science*. 2001;48(4):1503-1505.
29. George A, Chen PY, Morales-Martinez A, et al. Geometric calibration and correction for a lens-coupled detector in x-ray phase-contrast imaging. *Journal of Medical Imaging*. 2017;4(1):013507.
30. Panna A, Gomella A, Harmon K, et al. Performance of low-cost X-ray area detectors with consumer digital cameras. *Journal of Instrumentation*. 2015;10(05):T05005.
31. Yu T, Boone JM. Lens coupling efficiency: Derivation and application under differing geometrical assumptions. *Medical physics*. 1997;24(4):565-570.
32. Miller L. Transfer characteristics and spectral response of television camera tubes. In: *Photoelectronic Imaging Devices*. Springer; 1971:267-290.

33. Maidment AD, Yaffe MJ. Analysis of signal propagation in optically coupled detectors for digital mammography: II. Lens and fibre optics. *Physics in Medicine & Biology*. 1996;41(3):475.
34. Zhang L, Gao H, Li S, Chen Z, Xing Y. Cupping artifacts analysis and correction for a FPD-based cone-beam CT. Paper presented at: Computational Imaging IV2006.
35. Kak AC, Slaney M. *Principles of computerized tomographic imaging*. SIAM; 2001.
36. Coleman A, Sinclair M. A beam-hardening correction using dual-energy computed tomography. *Physics in Medicine & Biology*. 1985;30(11):1251.
37. Edey D, Pollmann S, Lorusso D, Drangova M, Flemming R, Holdsworth D. Extending the dynamic range of biomedical micro-computed tomography for application to geomaterials. *Journal of X-ray science and technology*. 2019;27(5):919-934.
38. Herman GT. Correction for beam hardening in computed tomography. *Physics in Medicine & Biology*. 1979;24(1):81.
39. Chen C-Y, Chuang K-S, Wu J, Lin H-R, Li M-J. Beam hardening correction for computed tomography images using a postreconstruction method and equivalent tissue concept. *Journal of digital imaging*. 2001;14(2):54-61.
40. Rührnschopf EP, Klingenberg K. A general framework and review of scatter correction methods in x-ray cone-beam computerized tomography. Part 1: Scatter compensation approaches. *Medical physics*. 2011;38(7):4296-4311.
41. Rührnschopf and EP, Klingenberg K. A general framework and review of scatter correction methods in cone beam CT. Part 2: scatter estimation approaches. *Medical physics*. 2011;38(9):5186-5199.
42. Boas FE, Fleischmann D. CT artifacts: causes and reduction techniques. *Imaging Med*. 2012;4(2):229-240.
43. Hsieh J. *Computed tomography: principles, design, artifacts, and recent advances*. Vol 114: SPIE press; 2003.
44. Mori I, Machida Y, Osanai M, Inuma K. Photon starvation artifacts of X-ray CT: their true cause and a solution. *Radiological physics and technology*. 2013;6(1):130-141.
45. Altunbas C, Lai CJ, Zhong Y, Shaw CC. Reduction of ring artifacts in CBCT: Detection and correction of pixel gain variations in flat panel detectors. *Medical physics*. 2014;41(9).

46. Alexeev T, Kavanagh B, Miften M, Altunbas C. Novel ring artifact suppression method for CBCT imaging with two-dimensional antiscatter grids. *Medical physics*. 2019.
47. Münch B, Trtik P, Marone F, Stampanoni M. Stripe and ring artifact removal with combined wavelet—Fourier filtering. *Optics express*. 2009;17(10):8567-8591.
48. Nagarajappa AK, Dwivedi N, Tiwari R. Artifacts: The downturn of CBCT image. *Journal of International Society of Preventive & Community Dentistry*. 2015;5(6):440.
49. Bucky G. Über die Ausschaltung der im Objekt entstehenden Sekundärstrahlen bei Röntgenaufnahmen. *Verh Dtsch Ront Ges*. 1913;9:30.
50. Potter HE. The Bucky diaphragm principle applied to roentgenography. *Archives of Radiology and Electrotherapy*. 1921;25(10):310-315.
51. Altunbas C, Kavanagh B, Alexeev T, Miften M. Transmission characteristics of a two dimensional antiscatter grid prototype for CBCT. *Medical physics*. 2017;44(8):11.
52. Zhou A, Tan Q, White GL, Davidson R. New antiscatter grid design by optimization of strip thickness and height. *International Journal of Imaging Systems and Technology*. 2021;31(3):1294-1299.
53. Altunbas C, Alexeev T, Miften M, Kavanagh B. Effect of grid geometry on the transmission properties of 2D grids for flat detectors in CBCT. *Physics in Medicine & Biology*. 2019;64(22):225006.
54. Alexeev T, Kavanagh B, Miften M, Altunbas C. Two-dimensional antiscatter grid: A novel scatter rejection device for Cone-beam computed tomography. *Medical physics*. 2018;45(2):529-534.
55. Park Y, Alexeev T, Miller B, Miften M, Altunbas C. Evaluation of scatter rejection and correction performance of 2D antiscatter grids in cone beam computed tomography [published online ahead of print 2021/02/09]. *Med Phys*. 2021;48(4):1846-1858.
56. Yu Z, Park Y, Altunbas C. Simultaneous scatter rejection and correction method using 2D antiscatter grids for CBCT [published online ahead of print 2020/04/22]. *Proc SPIE Int Soc Opt Eng*. 2020;11312.
57. Sisniega A, Abella M, Desco M, Vaquero J. Dual-exposure technique for extending the dynamic range of x-ray flat panel detectors. *Physics in Medicine & Biology*. 2013;59(2):421.
58. Sukovic P, Clinthorne NH. A method for extending the dynamic range of flat panel imagers for use in cone beam computed tomography. Paper presented at:

2001 IEEE Nuclear Science Symposium Conference Record (Cat. No. 01CH37310)2001.

59. Li Y, Han Y, Chen P. X-ray energy self-adaption high dynamic range (HDR) imaging based on linear constraints with variable energy. *IEEE Photonics Journal*. 2017;10(2):1-14.

Chapter 2

2 Cost-effective micro-CT system for non-destructive testing of titanium 3D printed medical components

(Under review - submitted to Plos One on October 14, 2021)

Micro-CT imaging can be used as an effective method for non-destructive testing (NDT) of metal 3D printed parts – including titanium biomedical components fabricated using laser powder-bed-fusion (LPBF). Unfortunately, the cost of commercially available micro-CT scanners renders routine NDT for biomedical applications prohibitively expensive. This study describes the design, manufacturing, and implementation of a cost-effective scanner tailored for NDT of medium-size, titanium, 3D printed, biomedical components. The main elements of the scanner; which include a low-energy (80 kVp), portable, x-ray unit, and a low-cost lens-coupled detector; can be acquired with a budget less than \$ 11000 USD. The low-cost detector system uses a rare-earth phosphor screen, lens-coupled to a dSLR camera (Nikon D800) in a front-lit tilted configuration. This strategy takes advantage of the improved light-sensitivity of modern, full-frame, CMOS camera sensors and minimizes source-to-detector distance, in order to maximize x-ray fluence. The imaging performance of the system is characterized using a state-of-the-art, CT, quality-assurance phantom, and two titanium, 3D-printed, test specimens. Our results show that our cost-effective scanner can survey the porosity and cracks in titanium parts with thicknesses of up to 13 mm of solid metal. Quantitatively, the scanner produced geometrically-stable reconstructions, with a voxel size of 118 μm , and noise levels under 55 HU. The cost-effective scanner was able to estimate the porosity of a 17 mm diameter, titanium, 3D-printed, cylindrical lattice structure, with a 0.3 % relative error. We believe our scanner will facilitate the implementation of titanium, LPBF-printed components for biomedical applications by incorporating routine, cost-effective NDT as part of the process control and validation steps of medical-device, quality-management systems. By reducing the cost of the x-ray detector and shielding, we can ensure that the scan cost will be commensurate with the overall cost of the validated component.

2.1 Introduction

Bench-top micro-CT scanners are widely used for non-destructive testing (NDT) of parts in the automotive, aerospace, pharmaceutical, and medical industries.^{1,2} The main components of these scanners are the x-ray source, the x-ray detector, and a rotary stage that are all enclosed in an x-ray shielded cabinet.³ With prices ranging from 100,000 to over 1 million USD dollars,^{4,5} industrial micro-CT scanners for NDT are equipped with high-energy (160-450 kVp) x-ray tubes that require heavy x-ray shielding, additional hardware (*e.g.*, power generators or cooling systems), and robust infrastructure to operate safely. For these high-energy systems, x-ray filtration is employed to reduce x-ray penetration, in order to scan samples made of various materials with a wide range of radiopacity (*i.e.*, plastics, ceramics, and metals). Additionally, these scanners are equipped with large-area, digital, flat-panel, x-ray detectors that allow for scanning of medium-to-large sized objects, that are characteristic of the automotive and aerospace industry.^{1,2,4} For applications where the cost of analysis must be commensurate with the cost of the part, these NDT tools become prohibitively expensive for routine use.⁴ For example, in the medical industry, the cost of scanning a \$300 part should not exceed more than approximately 10% of its cost, or \$30.

Scanning costs can be reduced using micro-CT scanners designed with task-specific, x-ray tube and detector combinations.¹ For example, de Oliveira *et al.*⁶ have described a low-cost (~ \$35,000) scanner for small-sized specimens (< 10 cm) using a low-energy, x-ray tube in a fan-beam configuration, and an x-ray detector made in-house comprised of a series of commercial photodiode arrays. Their low-cost detector had only one row of 512 (0.3 x 0.6 mm) photodiodes, which constrained the reconstruction volume of the scanner to a single slice. To avoid this limitation, industrial and commercially available micro-CT scanners typically use a cone-beam geometry and two-dimensional, flat-panel detectors, which can be very expensive. Dramatically reducing the cost of a medium-sized, high-definition detector is a very effective strategy for reducing the overall system cost, and thus making routine NDT of medical components feasible.

Micro-CT is an excellent NDT tool to investigate the internal integrity (*e.g.*, porosity and cracks) of a part, as well as its dimensional accuracy.⁷ In the case of medical components,

the required spatial resolution for a CT volume needs to be on the order of 0.1 mm in order to visualize any critical defects.⁸ This can be achieved through the use of flat-panel detectors with sufficiently-small pixel pitch, or the use of geometric magnification of the sample. Lens-coupled detector systems have been investigated in the past as an alternative, but have lacked the necessary light sensitivity or field-of-view, as they have been limited to small-scale imaging applications.⁹⁻¹² Recent advancements in full-frame CMOS imaging technology have shown promise in reaching the light sensitivity, field-of-view size, and spatial resolution required for computed tomography.¹³ Panna *et al.*¹⁴ have demonstrated the use of consumer-grade, digital cameras that are lens-coupled to x-ray phosphor screens as a viable way of constructing high-definition, medium-sized, x-ray detectors. They also demonstrated that, by placing the digital camera in front of the phosphor screen, in a front-lit, tilted configuration, these lens-coupled detectors are less susceptible to diffusion and attenuation of light in the phosphor, and are able to perform as well as modern digital flat-panel detectors.

In this study, we describe the first implementation of a low-energy (80 kVp), micro-CT system, equipped with a medium-sized, front-lit, lens-coupled detector, as a cost-effective alternative for NDT of medical components. We describe the necessary hardware and software required to acquire high-quality, micro-CT data and we characterize the performance of the scanner using a state-of-the-art quality assurance phantom.¹⁵ Finally, we demonstrate the use of this novel device to inspect two titanium, 3D-printed, test objects – one to evaluate the performance of the system while imaging highly-porous lattice structures, and the other to characterize x-ray penetration limits in this commonly-used, medical-grade alloy.

2.2 Methods

2.2.1 System Geometry Description

As previously mentioned, the basic components of a micro-CT scanner are an x-ray tube, a rotational stage, and an x-ray detector. These components in our low-cost, CT system were enclosed in a frame constructed using off-the-shelf 2 x 2 cm aluminum extrusion profiles and connectors. This 104 x 50 x 54 cm enclosure included opaque, non-reflective

panels that create a light-tight environment inside the frame, preventing any external light from interfering with the lens-coupled detector system. The panels were secured in position using the T-slot rail of the extrusion profiles. One side of the frame lacked a solid panel, but instead had an opaque, non-reflective fabric to facilitate access to the rotary stage for specimen loading. This fabric was secured in place during data acquisition using custom-made plastic clips.

Fig 2-1 describes the schematics of the frame and the internal components of the low-cost, micro-CT system. The configuration of the x-ray source, phosphor screen, and the camera-lens assembly is similar to the tilted-screen, front-lit configuration described by Panna *et al.*¹⁴ with the addition of a 2 mm thick, lead plate placed in between the rotary stage and the camera to prevent direct interactions between the camera CMOS sensor and any primary or scattered x-rays. The camera-lens assembly was mounted to the frame using two supporting 2 x 2 x 50 cm aluminum profiles and a 4 x 8 x 50 cm C-beam, linear railing with a sliding, gantry plate that allowed camera-to-screen distance adjustments. The phosphor screen was secured to one end of the C-beam using an acrylic sheet and two, 3D-printed, PLA clips. Underneath the acrylic sheet, a custom, 3D-printed, hinge joint allowed for the adjustment of the phosphor-screen tilt. All of the other joints and connectors allowed partial disassembly of the system, as well as adjustments to various geometric parameters (source-to-object distance (SOD), object-to-detector distance (ODD), detector-screen tilt angle, and camera-to-screen distance) making the design of our low-cost micro-CT system versatile, portable, flexible, and easily upgradable.

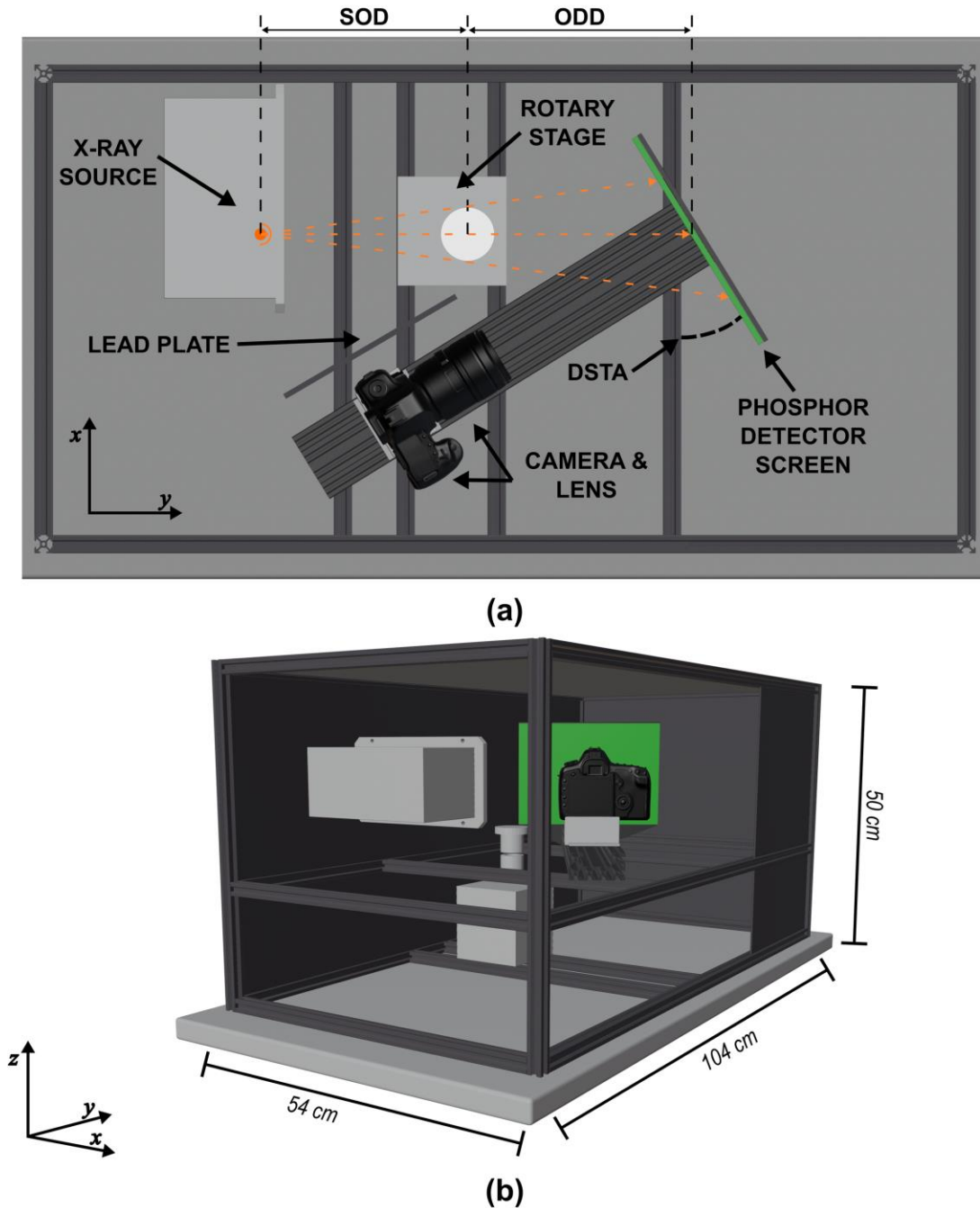


Fig 2-1. Geometry of the micro-CT System. (a) Top view depicting the arrangement of the internal components of the system: x-ray source, rotary stage, phosphor detector screen, detector-screen tilt angle (DSTA), lead plate, camera, lens, source-to-object distance (SOD), and object-to-detector distance (ODD). The orange dotted-lines represent the trajectory of the polychromatic, cone-shaped, x-ray beam. (b) Perspective view of the system showing the arrangement of the various 2 x 2 cm

aluminum extrusion profiles. One of the opaque panels was removed from the 3D rendering to allow visualization of the internal components.

2.2.2 Internal Components and Experimental Setup

The schematic in Fig 2-1, shows the configuration of the proposed system, including a portable, x-ray source with a 33 μm focal spot, capable of running at a maximum tube potential of 80 kVp and a maximum current of 0.5 mA (Sourceblock SR-80-500), placed in a close-assembly (*i.e.*, source-to-detector distance (SDD) of approximately 30 cm) to maximize x-ray fluence at the detector plane. Unfortunately, due to regulatory restrictions and reduced research capacity caused by the COVID-19 pandemic, we were unable to operate that x-ray source and instead used a general purpose, ceiling-mounted, x-ray source (Proteus XR/a, GE Medical Systems). The SDD for this configuration was 60 cm and images were captured at 80 kVp, and 10 mA. Fig 2-2 shows the experimental setup using the general purpose, ceiling-mounted, x-ray source. The x-ray protocol used with the general-purpose x-ray source was adapted to match the exposure levels that could be achieved with the proposed portable x-ray source. Table 2-1 summarizes the differences between the two x-ray units and the exposure matching protocol settings. Note that to match the dose-rate per unit of time (R/h), the exposure time was reduced by a factor of five.

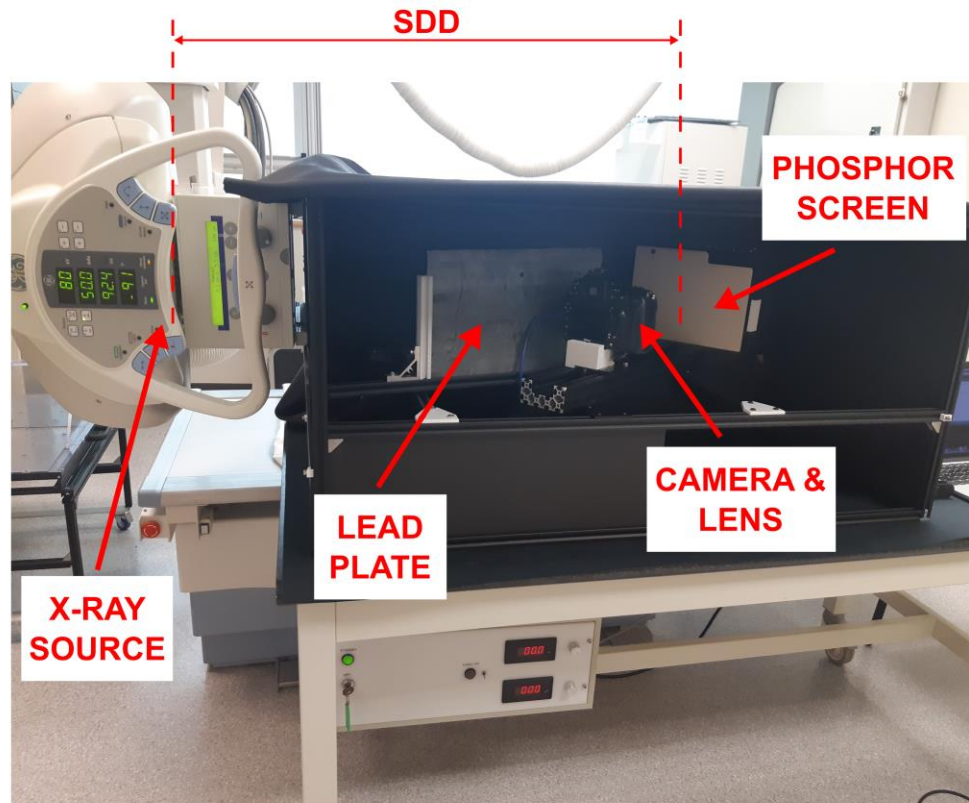


Fig 2-2. Experimental Setup using the General-Purpose X-ray Source. Note that the rotary stage is not visible as it is hidden behind the lead plate. The source-to-detector distance (SDD) was 60 cm.

Table 2-1. X-ray source comparisons and exposure-level matching, x-ray protocols.

	Portable x-ray Unit		General Purpose x-ray Unit	
	Source-Ray/SR-80-500		GE Medical Systems/Proteus XR/a	
	Unit	Protocol	Unit	Protocol
X-ray tube-potential (kVp)	35-80	80	40-150	80
X-ray tube-current (mA)	0.5	0.5	10-400	10
Focal spot size (mm)	0.033	0.033	0.6	0.6
Source-to-detector distance (cm)	-	30	-	60
Dose-rate* (R/h)	-	343.92	-	1717.97
Exposure time (s)	-	4	-	0.8
Tube-current exposure-time product (mAs)	-	2	-	8

**Dose-rates were calculated using Rad Pro Calculator version 3.26*

The rotational stage for the system was fabricated in-house and operated under a closed-loop, stepper-motor control with $< 5 \mu\text{m}$ precision. For each scan, 360 images were acquired at 1° angular increments. The stage was placed 30 cm from the x-ray source (source-to-object distance, SOD) and 30 cm from the phosphor screen central axis (object-to-detector distance, ODD). The magnification factor (M) of the system was calculated to be:

$$M = \frac{SDD}{SOD} = \frac{60 \text{ cm}}{30 \text{ cm}} = 0.5 \quad (2.1)$$

The x-ray detector was comprised of a 18 x 24 cm $\text{Gd}_2\text{O}_2\text{S} : \text{Tb}$ phosphor screen (Lanex Min-R 2000, Eastman Kodak Company), a fast, high-quality lens (35 mm, f1.4 prime Nikkor), and a full-frame detector, dSLR camera (Nikon D800). The camera-to-screen distance was set to 23 cm and the CMOS sensor focus was visually optimized prior data acquisition. Images were captured with the widest aperture setting (focal ratio of f/1.4) in order to maximize light collection. The camera exposure time was set to 4 s to match the exposure time required when using the proposed SR-800-500 x-ray source. This ensured that the appropriate amount of electronic noise (*i.e.*, dark-field) was included during data

acquisition and subsequent CT reconstruction. Finally, ISO sensitivity was set to 1600 ISO to cover the full dynamic range (14 bits) of the Nikon D800 camera.

2.2.3 Geometric Calibration and CT Reconstruction

For these experiments, the Nikon D800 captured RAW 6208 x 4924 pixels, 14-bit dynamic range, images in 5:4 mode (30 by 24 mm sensor area). These images contained the pixel-by-pixel intensity values of all three-color channels (*i.e.*, red, green, and blue) arranged in a RGGB Bayer pattern. The intensity values of each channel were averaged to generate a 3104 x 2462 image. Fig 2-3 shows an overview of the image acquisition and post-processing steps required prior to CT reconstruction.

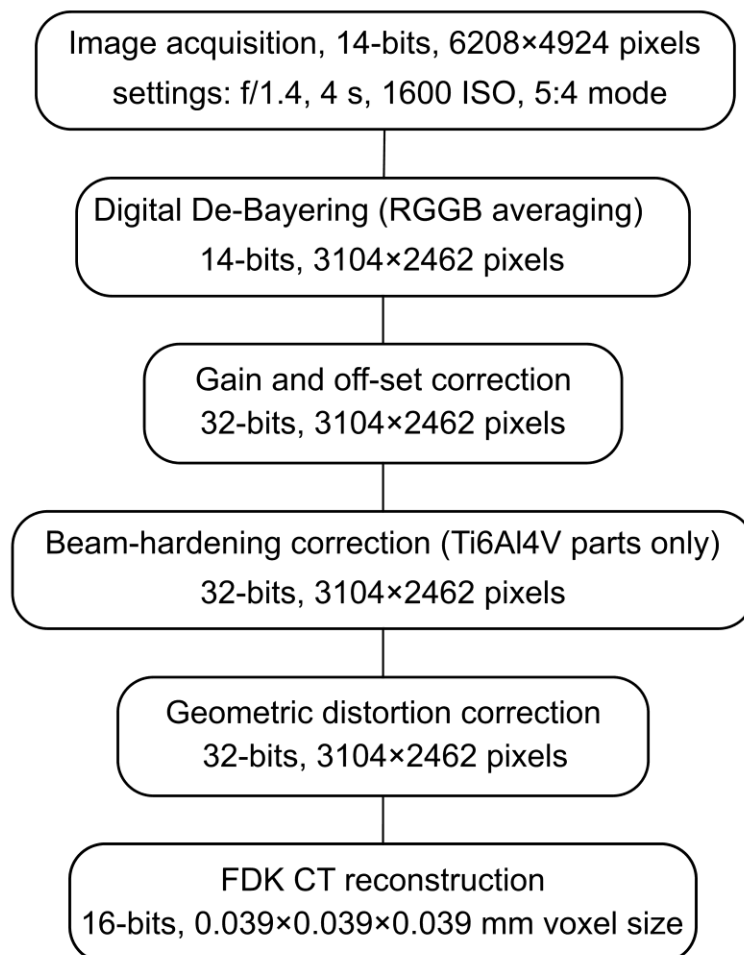


Fig 2-3. Summary of image processing steps required between projection data acquisition and CT reconstruction.

The image quality of any CT reconstruction depends on precise calibration of the imaging system. If the object space is not mapped correctly with the projection data, the reconstructions will have reduced spatial resolution, as well as image artefacts.¹⁶ In our system, this could be caused mainly by the geometric distortion of the object due to the tilted, front-lit configuration of the phosphor, and by source-detector alignment errors. Fortunately, both geometric distortion and source-detector alignment are tractable problems.

Lens, and perspective, geometrical-distortion corrections are routinely implemented in photogrammetry and industrial metrology.¹⁷ Additionally, we have demonstrated that similar corrections can be applied in radiography to increase spatial resolution using two orthogonal views of a tilted, x-ray detector.¹⁸ Our correction involved capturing a projection image of a precisely-fabricated, 80 x 80 mm grid containing 17 rows by 17 columns of 0.5 mm diameter, high-contrast, metal marker beads. The centroid of each marker bead was determined to subpixel accuracy and used to correct the image based on the *a priori* knowledge about the Cartesian grid.¹⁹ Source and detector alignment was estimated using a ring-shaped, high-contrast object that was placed 80 mm from the plane of the Cartesian grid toward the x-ray source. Proper alignment of this ring and the central marker of the grid was confirmed before data acquisition (Fig 2-4). The accuracy of the correction was evaluated, primarily, by imaging a cylindrical phantom with a series of high-contrast metal beads placed on the outer surface of the cylinder parallel to its longitudinal axis. The rotational path of the centroid of each marker was compared to their expected elliptical trajectory in one, full rotation of the rotational stage. Additionally, the roundness scores of the ring-shaped marker were calculated according to equation (2.2) and provided an additional, two-dimensional evaluation of the geometric correction.

$$roundness (R) = \frac{4 \times area}{\pi \times major\ axis^2} \quad (2.2)$$

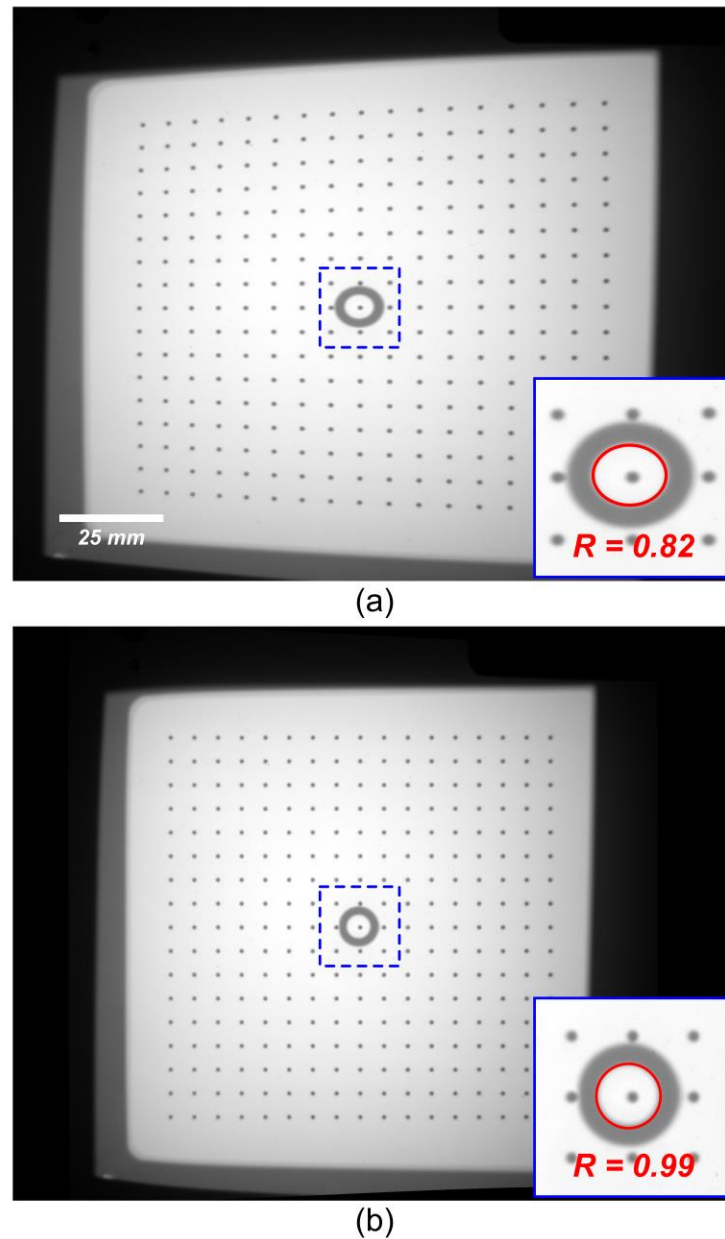


Fig 2-4. Assessment of geometric distortion correction resulting from the tilted-detector configuration. (a) shows the un-corrected, raw data of the Cartesian calibration grid. (b) corrected image of the Cartesian calibration grid.

For each data set, 360 projection images were acquired to perform a micro-CT reconstruction with a widely-employed Feldkamp, Davis and Kress (FDK), filtered-backprojection algorithm. Beam-hardening correction, following the protocol described by Edey *et al.*²⁰, was applied for the titanium specimens only. For all reconstructions, CT

numbers were linearly re-scaled into Hounsfield (HU) units. The voxel spacing of the original reconstruction matrix was $39.3 \times 39.3 \times 39.3 \mu\text{m}$. Following a quantitative assessment of the spatial resolution of the system, described below, all reconstructions were spatially averaged to $118 \times 118 \times 118 \mu\text{m}$ to improve the signal-to-noise characteristics of the data.

2.2.4 Phantoms

2.2.4.1 Quality Assurance Phantom

Fig 2-5 shows the three phantoms used in this study. The quantitative performance of the system was evaluated using a comprehensive micro-CT, quality-assurance phantom (Fig 2-5A) designed and described by Du *et al.*¹⁵ The different sections of the QA phantom were used to assess spatial resolution, geometric accuracy, CT number accuracy, linearity, uniformity, and noise.

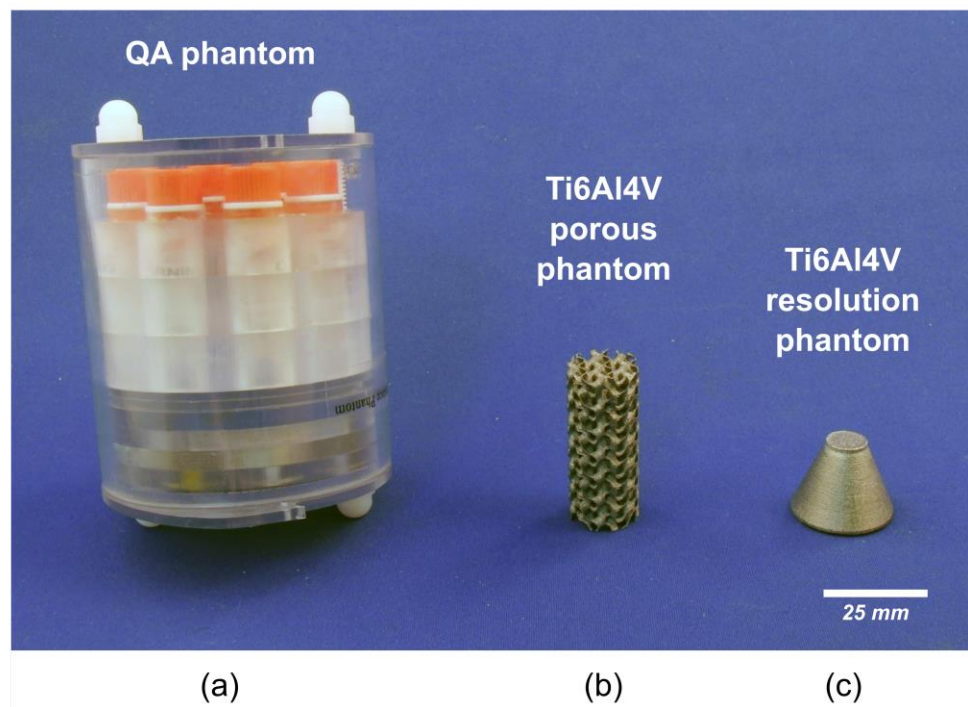


Fig 2-5 Physical appearance of the imaged phantoms for this study. (a) comprehensive quality assurance CT phantom, (b) porous, gyroid-based,

cylindrical, titanium-alloy (Ti6Al4V) phantom, and (c) titanium-alloy (Ti6Al4V) resolution phantom.

2.2.4.2 Porous Scaffold Phantom

To assess the capability of the system to visualize internal voids in a commonly-used, medical-grade alloy, two titanium (Ti6Al4V ELI-0406, Renishaw plc, United Kingdom, particle size 15-45 μm) test specimens were manufactured with a metal 3D printer (AM400, Renishaw plc, Wotton-under-Edge, United Kingdom) at the Additive Design in Surgical Solutions facility (ADEISS, London, Canada). The first titanium test specimen (Fig 2-5B and Fig 2-6) was a porous, cylindrical scaffold, 17 mm in diameter and 40 mm in length. The internal porosity of the scaffold was designed in Blender (Version 2.79, blender.org, Amsterdam, Netherlands) using a 6 mm³, sheet-based, gyroid unit cell. The prescribed porosity of the porous scaffold was 79.68% and was achieved by modifying the wall thickness of the gyroid unit to 0.4 mm (Fig 2-6C,D).

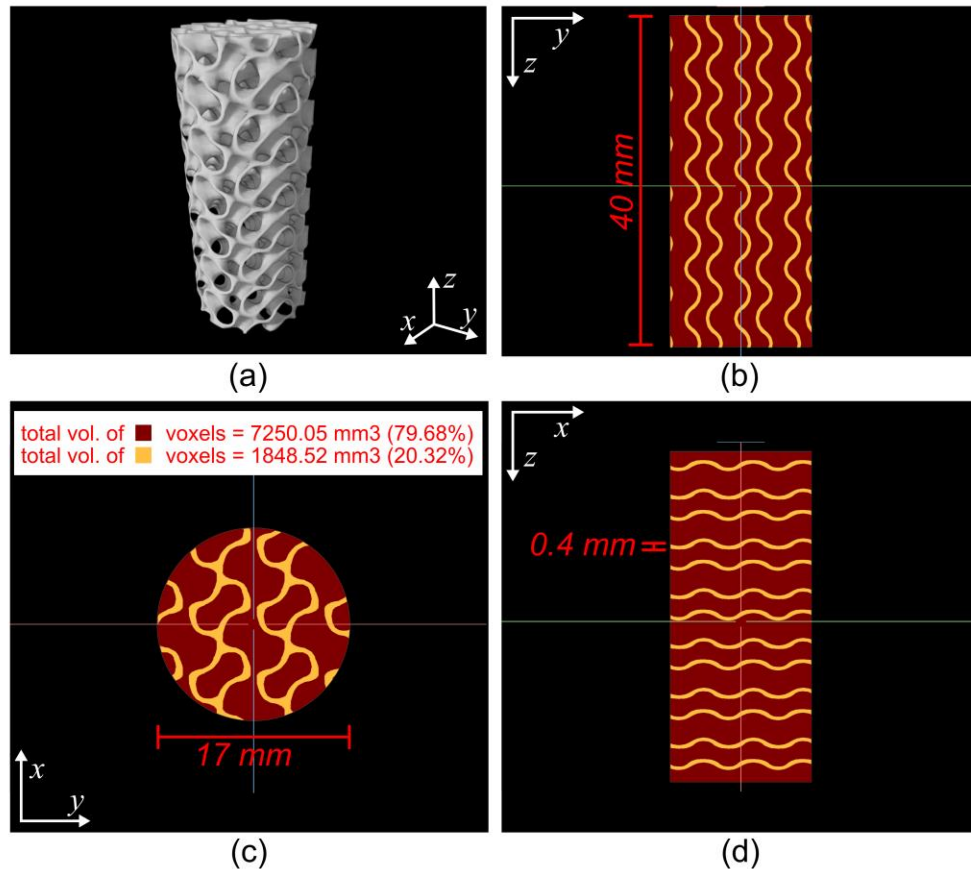


Fig 2-6 Computer-aided design (CAD) of the porous, gyroid-based, cylindrical, titanium-alloy (Ti6Al4V) scaffold. (a) perspective view of 3D rendering of the CAD. (b) Trans-coronal synthetic slice of the porous cylinder CAD. (c) Trans-sagittal synthetic slice of the porous cylinder CAD. (d) Transaxial synthetic slice of the porous cylinder CAD. (b),(c), and (d) are color coded to depict the titanium-alloy (yellow) and internal porosity (red) regions of the scaffold.

2.2.4.3 Titanium Resolution Phantom

The second titanium test specimen (Fig 2-5C and Fig 2-7) was a truncated cone, 17 mm high, with a 25 mm diameter base, and a 10 mm diameter top. Incorporated into the design were a series of internal cavities or voids which, in cross-sectional view, were seen as: a set of five bar patterns (formed from alternating regions of titanium and air with spacing varying from 1.66 to 10 lp/mm); a set of five circular air cavities with diameters varying from 0.025 to 0.3 mm; and a set of five rectangular air cavities 3 mm wide with varying thicknesses from 0.025 to 0.3 mm. These internal cavities extended from the top of the truncated cone to the base along the phantom's longitudinal axis. The top and the base of the truncated cone were two, 1 mm thick, disk-shaped regions. Fig 2-7 shows a detailed schematic of this titanium resolution phantom that was designed to assess the ability of the low-cost micro-CT system to resolve features of various sizes inside a solid object as the cumulative, x-ray, path length across the material increases. The x-ray, path length increases as the diameter of the cross-sectional area of the cone increases towards the base of the phantom.

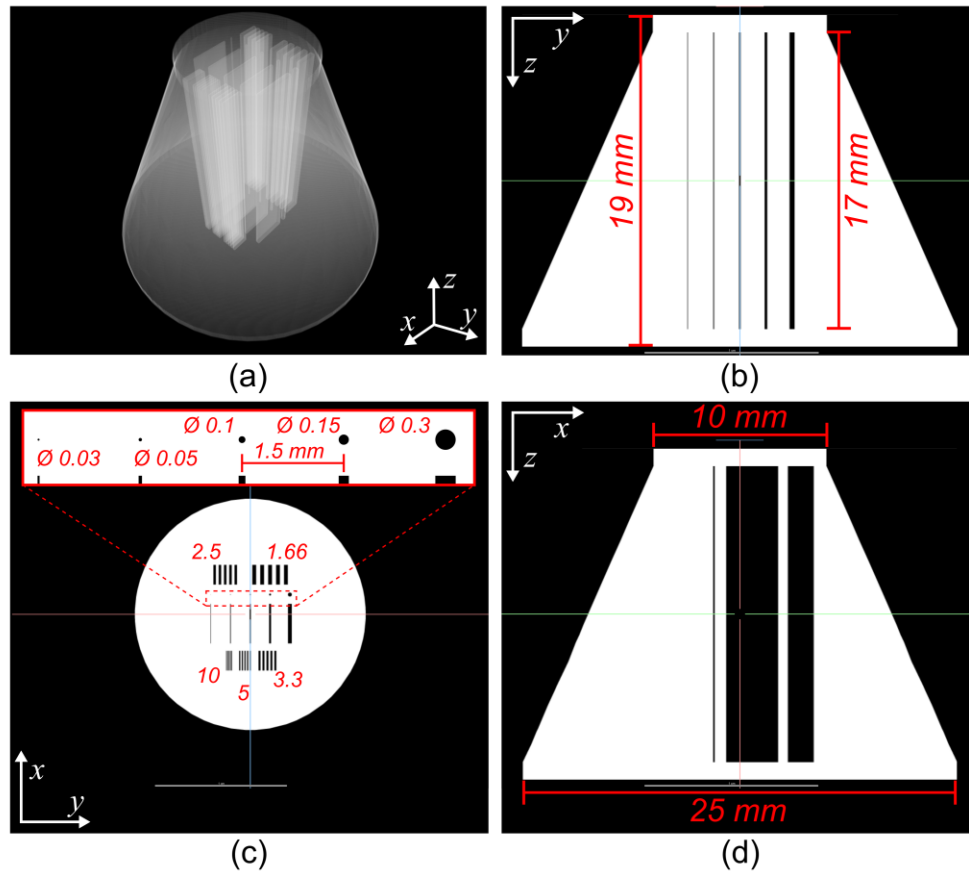


Fig 2-7 Computer-aided design (CAD) of the resolution titanium-alloy (Ti6Al4V) phantom. (a) translucent perspective view of 3D rendering of the phantom's CAD. (b) Trans-coronal synthetic slice of the phantom's CAD. (c) Trans-sagittal synthetic slice of the phantom's CAD depicting details of the internal voids. The bar patterns are described in lp mm^{-1} all the other measurements are shown in mm (d) Transaxial synthetic slice of the phantom's CAD.

2.2.5 Data Analysis

The spatial resolution of the micro-CT scanner was quantitatively measured over a range of spatial frequencies, using two different methods to calculate the MTF of the system. The first method used the slanted-edge plate of the QA phantom and the algorithm described by Judy.²¹ The second method, described by Anam *et al.*,²² used a cross-sectional reconstruction of a 0.1 mm diameter copper wire that was wrapped around one of the plates of the QA phantom. The spatial resolution was qualitatively evaluated using

a different plate of the QA phantom that included four spiral coils fabricated with alternating aluminum and Mylar sheets with various thicknesses of 150, 200, 300, and 500 μm – corresponding to 3.3, 2.5, 1.6, and 1 lp/mm, respectively. Using Droege's method,²³ the modulation parameter was calculated using the standard deviation of pixel values in a region-of-interest (ROI) within the coils. A set of these modulation parameters were useful to verify the MTF calculation for our system.

Geometric accuracy was determined using another plate within the QA phantom containing five beads placed at precisely known locations. The 3D, sub-voxel, weighted centroid of each bead was calculated using standard methods and the distances from each centroid to that of all the other neighboring beads were measured in voxels. The known distances between beads were used to calculate the true, in-plane, voxel size of the reconstructions.

The CT number evaluation and linearity of the system were measured using two other plates of the QA phantom designed for these purposes. The CT number of each of the eight materials was reported by measuring the mean grey-scale intensity in Hounsfield units (HU) within a 1.5 x 1.5 x 1.5 mm ROI placed in the center of each material sample. Linearity was determined by vials of iodinated contrast agent (Omnipaque 300, GE Healthcare, Oakville, ON), with concentrations varying from 0.9375 to 30 mg ml⁻¹. A linear-regression analysis was used to determine the relationship between the signal intensity and iodine concentration.

The uniformity of the system was qualitatively evaluated using the uniformity plate of the QA phantom and a radial signal profile taken through the center of a homogeneous region covering the central reconstructed slice. Ten slices were averaged to improve the noise characteristics of the data and allow proper visualization of any non-uniformities. This plate was also used to quantitatively report uniformity and noise using four ROIs located at the periphery of the plate as well as one ROI located in the center. The uniformity percent and the average of the measured standard deviations for each ROI is reported.

An ROI of the titanium porous scaffold was segmented from the beam-hardening-corrected reconstruction using Dragonfly software, version 2020.2 (Object Research

Systems Inc, Montreal, Canada) and a standard full-width-at-half-maximum (FWHM) threshold in order to determine the volume of titanium excluding the surrounding air. The centroid of each slice, perpendicular to the longitudinal axis of the sample, was used to draw a circular mask fitting the bounding box of the titanium ROI. These circular masks were combined to generate a cylindrical ROI that represented 100% of the volume of the titanium scaffold with the surrounding air excluded. The percentage porosity of the reconstructed sample was then calculated using:

$$CT \text{ scaffold porosity} = \left(1 - \frac{\text{titanium ROI volume}}{\text{cylindrical ROI volume}}\right) \times 100 \quad (2.3)$$

This CT-derived porosity fraction was compared with the gravimetrically-determined, porosity fraction of the 3D printed sample, which was determined by weighing the printed scaffold using a high-precision scale (BP3100P, Sartorius, Göttingen, Germany, 0.01 g accuracy) and comparing it with the mass of a solid titanium cylinder.

The x-ray path-length limit for titanium was measured using the titanium resolution phantom. This limit was determined by measuring the diameter of the phantom at the height of the cone where its internal features – the centrally located voids – were no longer visible in a lateral cross-sectional view. The phantom was also used to qualitatively evaluate the spatial resolution of the system when imaging highly radio-opaque materials.

2.3 Results

2.3.1 Cost-effectiveness analysis

Several private companies selling micro-CT, NDT devices were surveyed and reported scanner prices ranging from \$ 260,000 for a small field-of-view scanner to over \$ 750,000 for a large field-of-view scanner. Table 2-2 details the costs of all the off-the-shelf components of our proposed low-cost scanner. Thanks to the use of a relatively low-energy source (80 kVp), the calculated shielding requirements for routine use of our proposed system were significantly lower than other scanners operating at higher energies. For instance, reduction of the radiation measurements caused by primary x-rays

behind the phosphor screen to the required 0.005 mSv/h can be achieved using an 8.4 mm lead plate. Additional shielding will be required to enclose the portable x-ray source, as the Sourceblock SR-80-500 unit is sold without x-ray protection. Fortunately, lead-based x-ray protection is not costly, unless its weight impacts other aspects of the design of the CT scanner.

Table 2-2. Summary of the estimated costs for the main components of our low-cost CT scanner.

Component	Cost (USD)
Sourceblock SR-80-500 (portable x-ray unit)	\$ 4495
Nikon D800 dSLR camera	\$ 3000
Nikkor 35 mm f/1.4 lens	\$ 1100
Phosphor screen	\$ 30
Rotary stage and frame	\$ 600
X-ray shielding	\$ 1500
Total costs:	\$ 10725

Scan time is another important aspect to consider for the cost-effectiveness of routine NDT. Time consuming NDT might cause prohibitively long delays in some clinical applications or significantly increase the cost per scan. In our experiments, the total scan time per projection image was 7.5 seconds (*i.e.*, 45 minutes for 360 projection images). From these 7.5 seconds, 4 s were utilized for data acquisition, and 3.5 s were required for data transfer from the Nikon camera to the computer over USB 3.0.

2.3.2 Geometric correction

The mean deviation from the ideal trajectory was measured (1.14 ± 1.34 pixels) showing that the correction rendered trajectories with deviations within the spatial resolution of the detector – which was mainly limited by penumbral blur of the focal-spot (~ 0.3 mm). Fig 2-8. Results of geometric calibration evaluation using a cylindrical phantom with four radiopaque marker beads. (a) x-ray projection radiograph of the phantom; (b) uncorrected and corrected elliptical trajectories prescribed by the phantom’s markers over the course of one full rotation of the rotary stage. (c) close-up of uncorrected and corrected elliptical

trajectories of the top-most marker bead. The corrected position of the markers aligns with the ideal trajectory calculated using a sinusoidal best fit. shows a projection image of the phantom as well as the measured and expected elliptical trajectories of each marker.

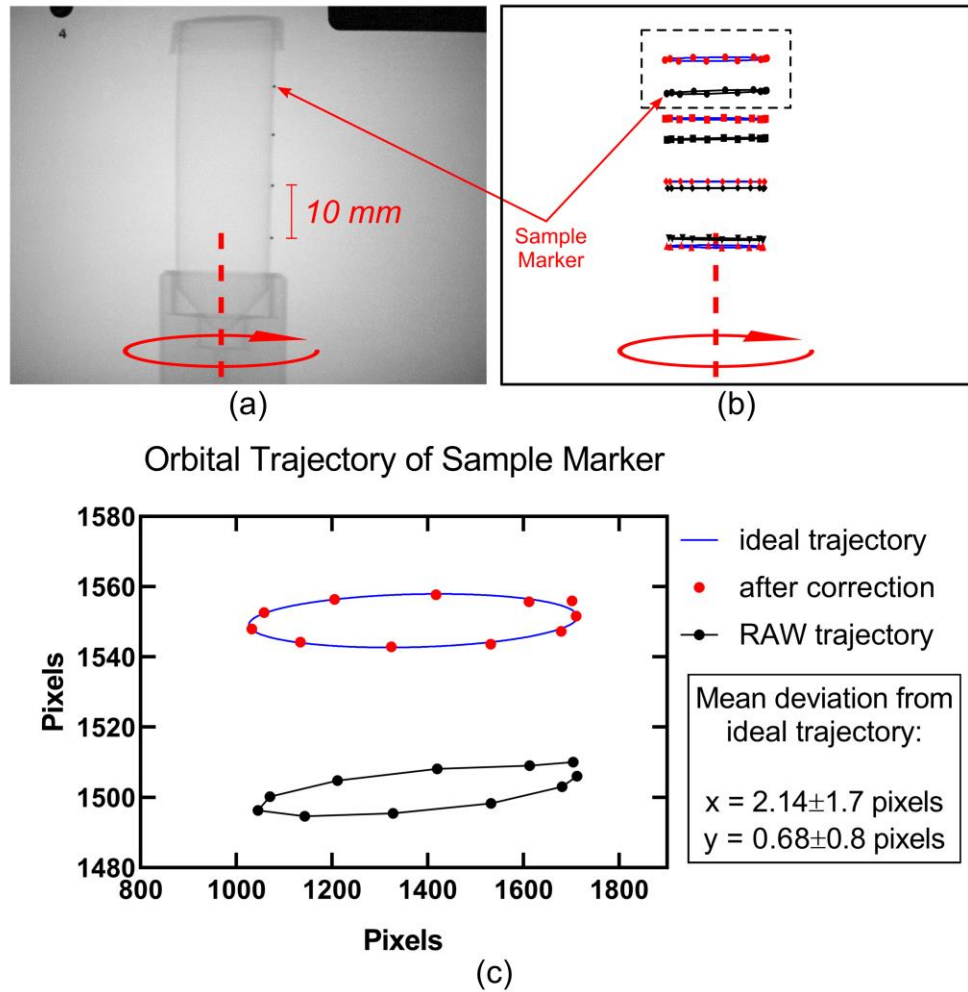
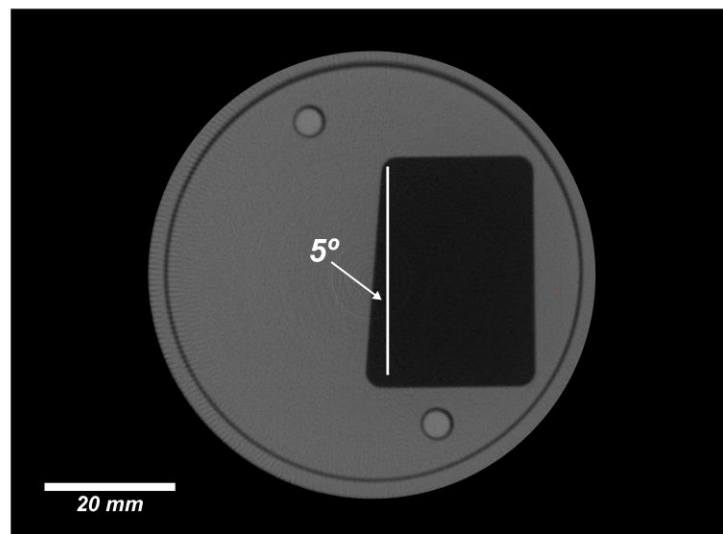


Fig 2-8. Results of geometric calibration evaluation using a cylindrical phantom with four radiopaque marker beads. (a) x-ray projection radiograph of the phantom; (b) uncorrected and corrected elliptical trajectories prescribed by the phantom's markers over the course of one full rotation of the rotary stage. (c) close-up of uncorrected and corrected elliptical trajectories of the top-most marker bead. The corrected position of the markers aligns with the ideal trajectory calculated using a sinusoidal best fit.

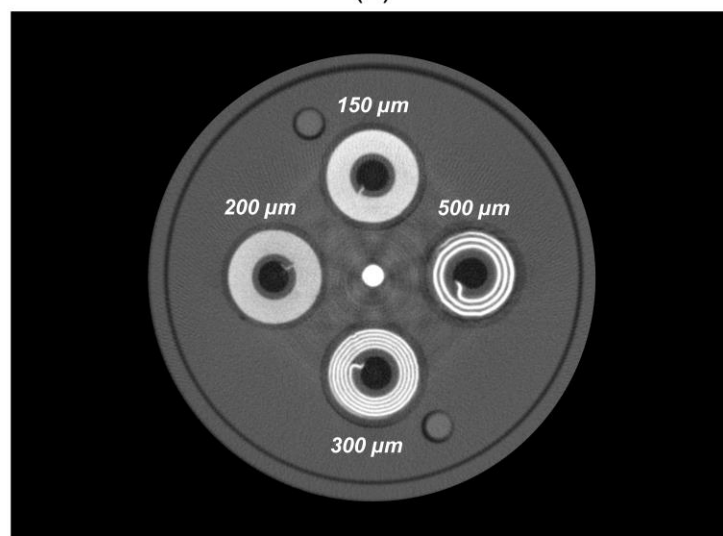
2.3.3 Imaging Characteristics of the System

2.3.3.1 Spatial resolution

The spatial resolution of the system was quantitatively evaluated by calculating the pre-sampled MTF of the system using the reconstructed image of the slanted-edge plate of the QA phantom (Fig 2-9A). The resolution limit at the 10% level was reached at 2.12 line pairs per mm, which corresponds to a spatial resolution of 235 μm . The same results were observed and confirmed when calculating the MTF of the system using the wire-based methodology (Fig 2-10).



(a)



(b)

Fig 2-9. Evaluation of spatial resolution of the cost-efficient CT scanner. (a) a single reconstructed transaxial-slice CT image of the slanted-edge plate of the CT quality assurance phantom. (b) reconstructed transaxial-slice CT image of the resolution coil plate of the CT quality assurance phantom illustrating the qualitative display of resolution coils.

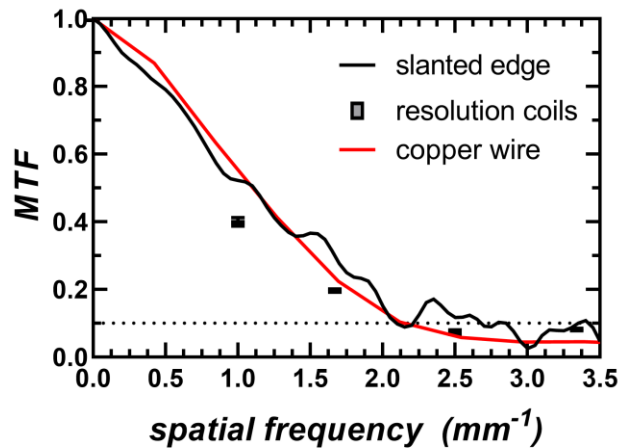


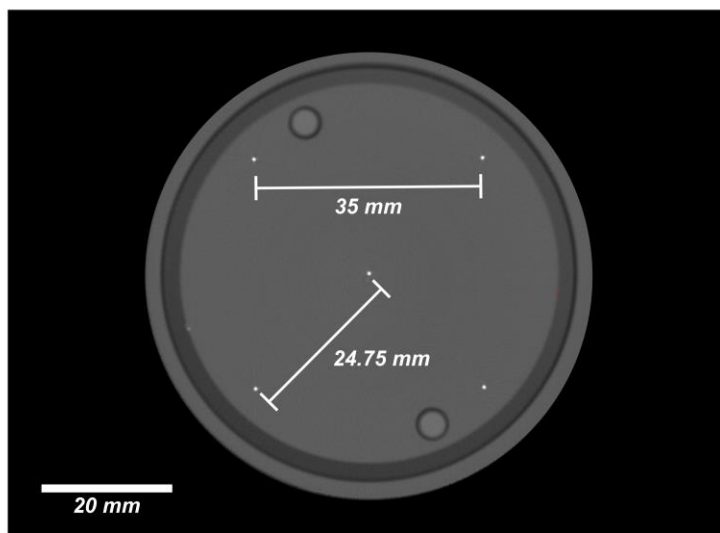
Fig 2-10. Modulation transfer function (MTF) of the cost-effective CT scanner measured from the slanted-edge plate, the resolution coil plate, and the copper wire of the CT quality assurance phantom. The 10% MTF level was reached at 2.12 mm^{-1} , corresponding to a spatial resolution of $235\text{ }\mu\text{m}$.

Qualitatively, it was observed that only the $300\text{ }\mu\text{m}$ and the $500\text{ }\mu\text{m}$ coil patterns were resolved as they represented spatial frequencies of 1.6 and 1 line pairs per mm respectively (Fig 2-9B). The MTF estimates using the standard deviation of ROIs inside the coil patterns closely agreed with the other quantitative MTF calculation methods (Fig 2-10).

2.3.3.2 Geometric accuracy

The average, in-plane, voxel spacing of the CT reconstructions ($118.39 \pm 0.20\text{ }\mu\text{m}$) was calculated by dividing the known distance between beads in the geometric accuracy plate of the QA phantom (Fig 2-11) by the measured inter-bead distance in voxels. Table 2-3 shows the sub-voxel, Euclidean distances between the centroids of all five beads of the

geometric-accuracy plate of the QA phantom. The mean, sub-voxel, physical distances for all three known inter-bead configurations (35, 24.75, and 49.5 mm) were 295.63 ± 0.46 , 209.05 ± 0.46 , and 418.10 ± 0.16 voxels respectively. The small standard deviation between the measured Euclidian distances shows the high geometric accuracy of the CT reconstructions achieved by our low-cost CT system.



(a)

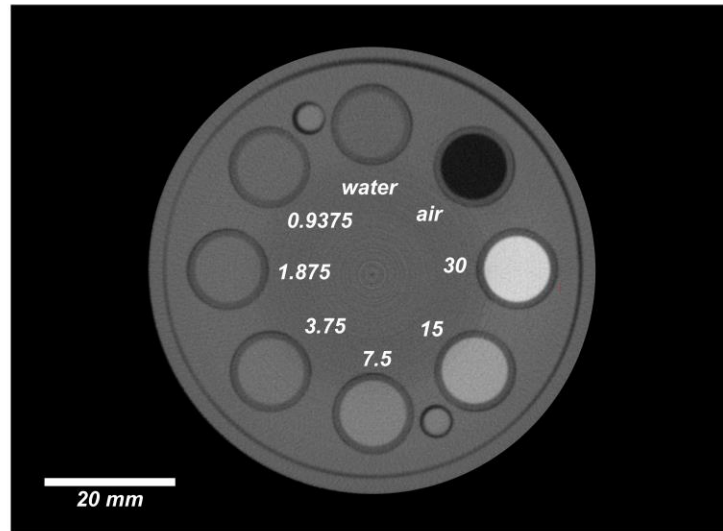
Fig 2-11. Reconstructed transaxial-slice CT image of the geometric-accuracy plate of the CT quality assurance phantom with four beads located at the periphery and 35 mm apart and one central bead at a distance of 24.75 mm from the other four.

Table 2-3. Sub-voxel, Euclidean distances between the centroids of all five beads of the geometric accuracy plate of the CT quality assurance phantom.

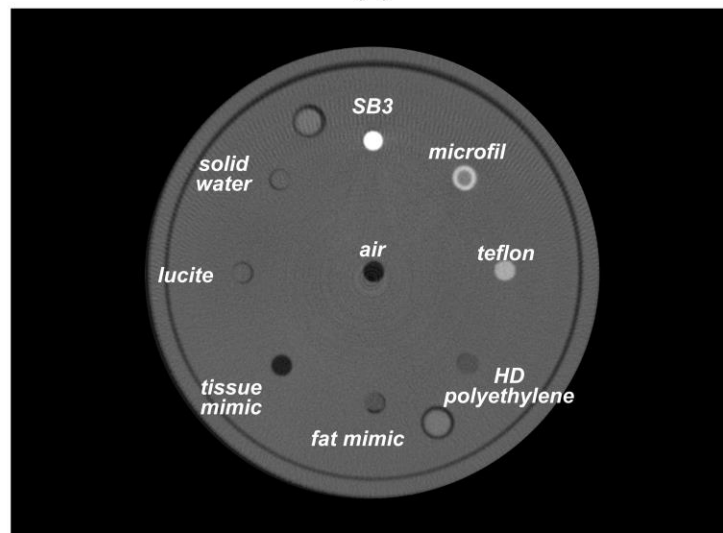
	Central	Periphery 1	Periphery 2	Periphery 3	Periphery 4
Central bead	0	209.00	209.76	208.93	208.48
Periphery 1	209.00	0	295.58	417.93	295.61
Periphery 2	209.76	295.58	0	296.39	418.25
Periphery 3	208.93	417.93	296.39	0	294.96
Periphery 4	208.48	295.61	418.25	294.96	0

2.3.3.3 Linearity

Linearity ($p < 0.001$) was calculated using the measured intensity values of ROIs placed within vials filled with various concentrations of iodine (Fig 2-12A). Fig 2-13 shows the relationship between signal intensity (S) and iodine concentration (C), as well as the result of a linear regression between these variables $S = 54.62 \text{ (ml mg}^{-1}) \times C + 26.4 \text{ (HU)}$, where C is the iodine concentration in mg ml^{-1} ($R^2 = 0.9998$). Although the y-intercept 26.4 HU was statistically different than zero its value was within the noise range ($54.48 \pm 4.6 \text{ HU}$) meaning that the system's CT numbers were well calibrated.



(a)



(b)

Fig 2-12. Reconstructed transaxial-slice CT images of the linearity plate (a) with air, water, and various concentrations of iodine shown in ml mg^{-1} ; and the CT number evaluation plate (b) of the CT quality assurance phantom.

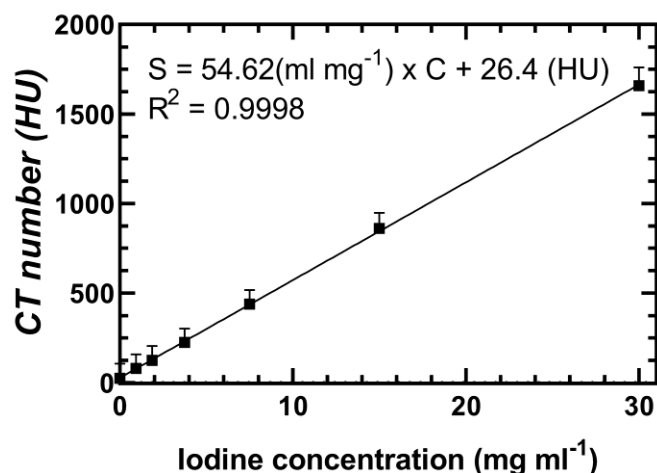
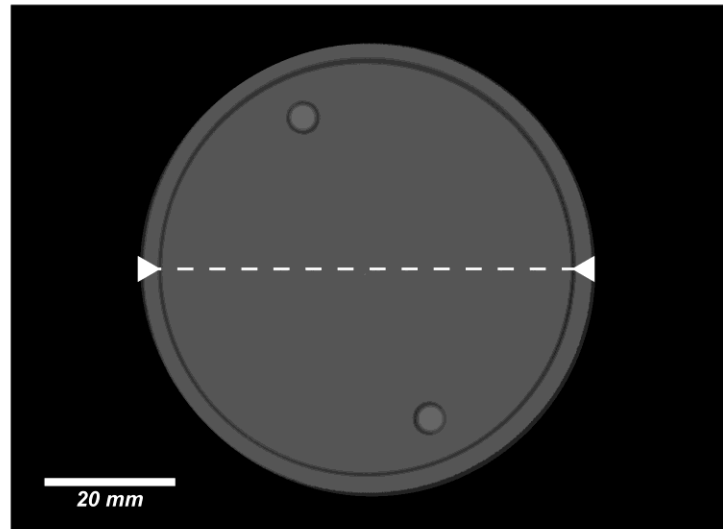


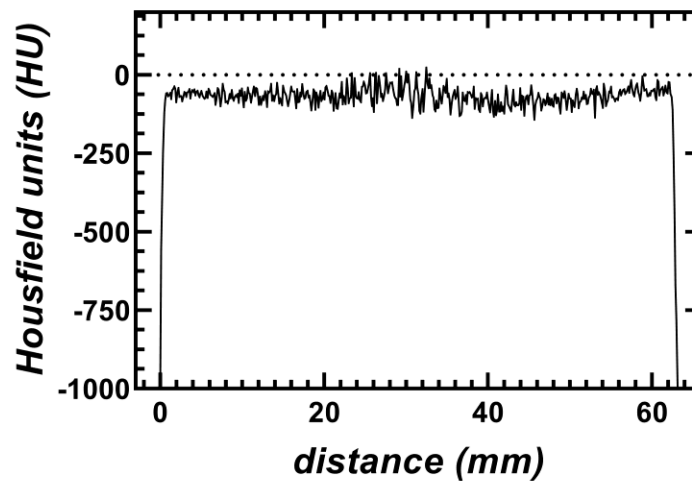
Fig 2-13. Plot of measured CT number within ROIs placed in each iodine vial versus known iodine concentration within the linearity plate of the CT quality assurance phantom. A significant linear correlation is seen between CT number in HU and iodine concentration in mg ml⁻¹.

2.3.3.4 Uniformity and noise

Quantitatively, the difference in CT numbers between the periphery of the QA phantom and the center was 1.73% (~ 18 HU). Qualitatively, the uniformity of the system was assessed with the radial signal profiles taken through the center of the uniformity plate of the QA phantom (Fig 2-14B). Noise (54.48 ± 4.6 HU) was characterized using the average standard deviation of the five ROIs used for the uniformity analysis. Noise increased up to 82 HU for ROIs within materials with higher attenuation coefficients such as the highest-concentration (30 mg ml^{-1}) iodine solution of the linearity plate. This is a good indicative that the system is dominated by photon noise.



(a)



(b)

Fig 2-14. (a) Reconstructed transaxial-slice CT image of the uniformity plate of the CT quality assurance phantom. (b) Radial signal profile taken through the center of the uniformity plate as illustrated by the white dotted-line in (a).

2.3.4 Titanium metal-alloy (Ti6Al4V) phantoms

2.3.4.1 Porous gyroid-based scaffold

As shown in Fig 2-15A, our low-cost CT system produced a CT reconstruction of the 17 x 40 mm titanium-alloy, porous cylinder that closely matched the prescribed CAD design. Inspection of the reconstructed slices clearly shows the gyroid-based, internal

structure of the scaffold, allowing full interrogation of the reconstructed volume (Fig 2-15B,D-F). Fig 2-15C shows how the threshold value was determined in order to segment the titanium ROI using the FWHM method. The total porosity of the construct (84.26%) was calculated by subtracting the volume of the titanium ROI (1429.95 mm³) from the volume of the bounding, cylindrical ROI (9081.95 mm³). The outline of the cylindrical ROI corresponding to 100% of the volume of the part is shown in Fig 2-15F.

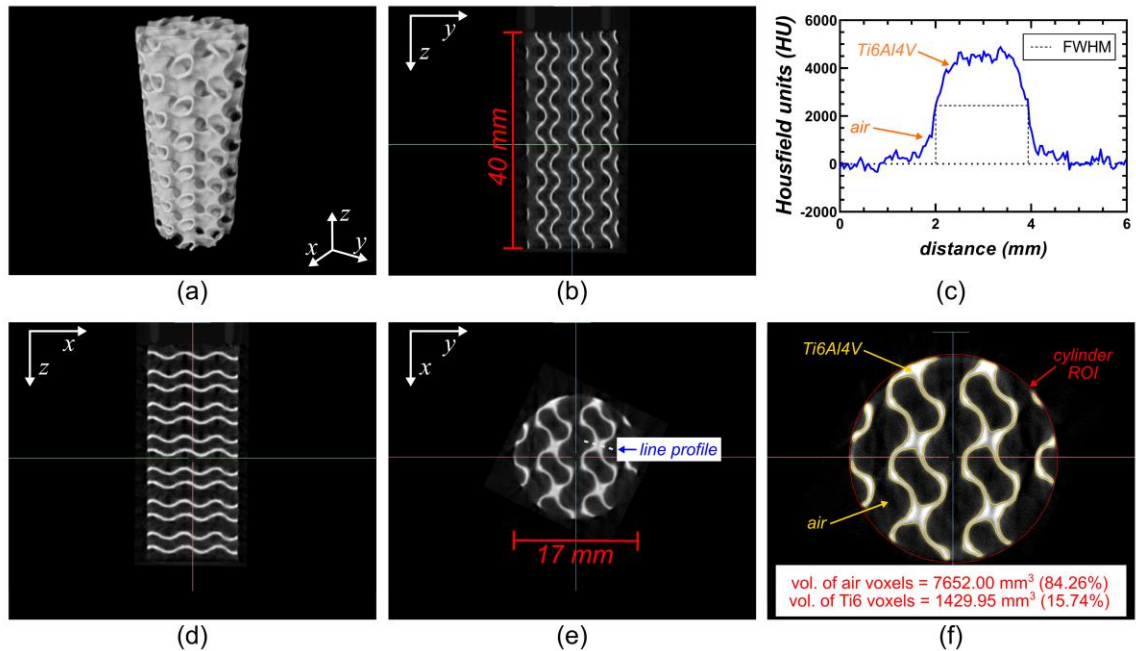


Fig 2-15. CT reconstruction of the porous, gyroid-based, cylindrical, titanium-alloy (Ti6Al4V) scaffold using the cost-effective CT scanner. (a) perspective view of volumetric rendering using the FWHM threshold used to segment titanium. (b) Trans-coronal slice CT reconstruction of the porous cylinder. (c) Signal profile across a wall of the porous cylinder used to determine the FWHM threshold for segmentation. (d) Trans-sagittal slice CT reconstruction of the porous cylinder. (e) Transaxial slice CT reconstruction of the porous cylinder and line profile used for (c). (f) close-up version of (e) illustrating boundaries between the titanium and air ROIs used to measure the porosity of the porous, cylindrical, titanium scaffold.

The porosity of the gyroid-based, titanium-alloy scaffold was also measured using the mass of a solid cylinder (17 x 40 mm) that was printed at the same time as the scaffold.

The mass of the solid cylinder was found to be 38.86 g and the mass of the porous scaffold 6.26 g, leading to a calculated porosity of:

$$\text{porosity \%} = \left(1 - \frac{\text{scaffold mass}}{\text{solid mass}}\right) \times 100 = \left(1 - \frac{6.26 \text{ g}}{38.86 \text{ g}}\right) \times 100 = 83.89\%$$

2.3.4.2 Titanium-alloy resolution phantom

Fig 2-16 shows the CT reconstruction of the conical, titanium-alloy resolution phantom. Fig 2-16B,D show severe photon starvation artifacts starting around the 13 mm diameter mark and worsening at greater diameters. Below this level, most of the internal features of the phantom were still resolved with the exception of the cylindrical voids with diameters smaller than 0.1 mm, and the 10 lp/mm bar patterns.

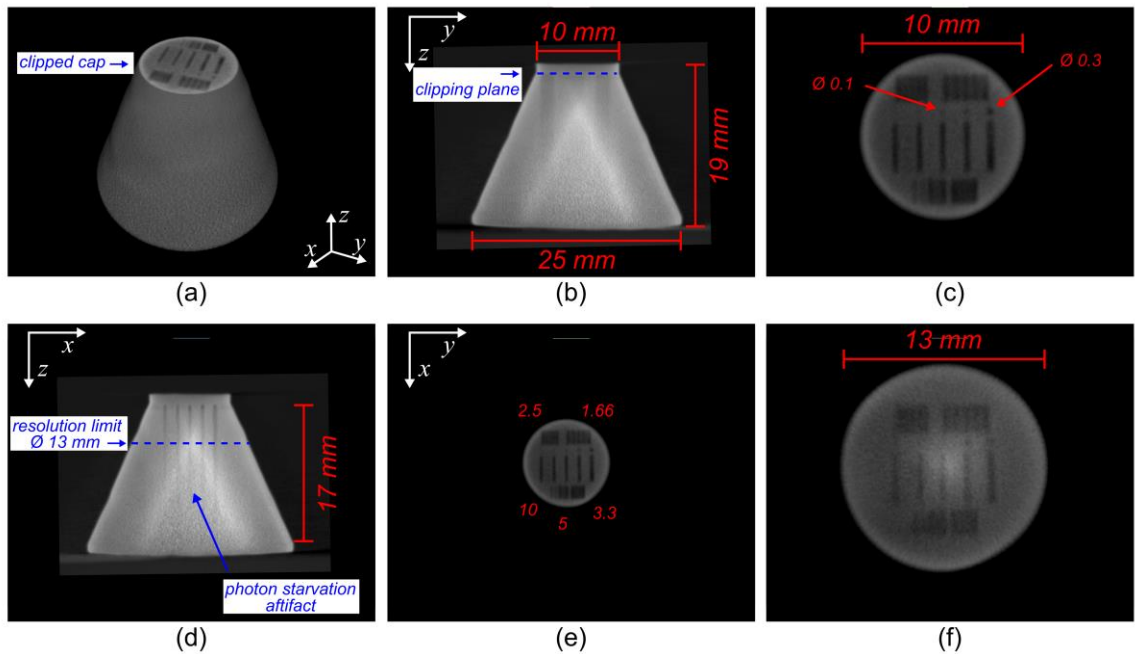


Fig 2-16. Beam-hardening corrected CT reconstruction of the titanium-alloy resolution phantom using the cost-effective CT scanner. (a) Volumetric rendering of the phantom with the top cap clipped to reveal the internal-void features of the resolution phantom. (b) Transcoronal slice of the resolution phantom showing the relative position of the clipping plane for (a). (c) Close-up of (e) illustrating the internal features of the phantom at the level of the clipping plane where the outer

diameter of the object is 10 mm. (d) Transsagittal slice of the resolution phantom showing the level where the resolution limit was reached. (e) Transaxial slice of the resolution phantom showing details of the internal features of the phantom. (f) Transaxial slice at the level of the resolution limit where the external diameter of the phantom was 13 mm. At diameters greater than this, internal-void features are difficult to distinguish, and photon starvation artifacts start to dominate.

2.4 Discussion

Non-destructive testing of porous, titanium-alloy, 3D-printed parts is possible using a low-cost, micro-CT scanner fabricated with off-the-shelf components. The cost-effectiveness of the proposed system takes advantage of some of the design constraints characteristic of most medical devices – which include high-porosity, small size, and relatively-low x-ray attenuating materials. We have demonstrated that routine NDT of titanium, 3D-printed, medium-sized, highly-porous, medical components is feasible using our proposed cost-effective CT system.

This novel CT system includes a low-cost, lens-coupled, x-ray detector comprised of a consumer-grade, dSLR camera and a phosphor screen. The consumer grade dSLR camera and an appropriately chosen lens exploit the front-lit configuration described by Panna *et al.*,¹⁴ where the light emitted by the phosphor is more effectively captured than in other configurations.^{9,10,13,14,24} Other advantages of this configuration include: (1) a reduced optical diffusion of the captured light as it does not need to pass through the phosphor to be detected (*i.e.*, reduced light scattering within the phosphor); (2) improved spatial resolution in one-plane due to the tilted configuration of the phosphor screen; (3) no bright-pixels in the captured images as the camera sensor can be positioned out of the direct x-ray beam path and properly shielded; and (4) a significant reduction in cost compared to similar-sized, digital, flat-panel detectors.

In our experiments, spatial resolution (0.235 mm) was mainly limited by penumbral blur due to the focal-spot size (~ 0.3 mm), but we believe that this could be easily resolved by using an x-ray source with a smaller focal-spot. For instance, if an x-ray source like the proposed Sourceblock SR-80-500 were to be used, then the focal-spot blur will be ten

times lower. This will allow taking better advantage of the high resolution of the camera, lens, and the phosphor screen. Further improvements in spatial resolution could be achieved by removing the RGGB Bayer filter included in the Nikon D800 dSLR camera as in our implementation only the green channels used the full 14-bit dynamic range of the camera's detector. This modification could also improve the light sensitivity of the detector, as the added filters reduce the quantum efficiency of the underlying pixels. Our selection of a color-camera was based on cost and availability considerations as similar true black and white cameras are more expensive and difficult to source.

Although we decided to capture a field-of-view covering the full area of the (18 by 24 cm) phosphor screen, both the detector-to-source distance and the object-to-detector distance could be adapted for smaller objects. This will increase the intensity of the captured light requiring lower ISO sensitivity values to cover the full dynamic range of the CMOS detector. Lower ISO values are desirable as signal-to-noise will be reduced by half for each ISO speed setting or "f-stop". Furthermore, the camera could be set to capture smaller regions of the CMOS detector. For example, the Nikon D800 has a 24 by 16 mm DX mode, which could reduce read-out and post-processing times.

Changes in the geometry of the system, to accommodate various specimen sizes, or following assembly of the system, will require the acquisition of new geometric calibration images. In our experience this process was not time-consuming, except for the manual segmentation of the markers of the calibration grid. A more sophisticated and automated segmentation algorithm would be recommended in case of regular modifications to the geometry of the system. Another alternative would be to acquire calibration images for a set of pre-calibrated geometries using additional repositioning hardware. The geometric accuracy of the reconstructions in this study shows that our geometric calibration strategy was successful. Future work includes the manufacturing of a calibration grid with a larger coverage of the phosphor screen. We anticipate that geometric calibration might be more challenging at the edges of the full-frame image, as non-linear lens aberrations are more pronounced in this area of the image – especially when using large lens aperture settings.¹²

The quantitative metrics of our low-cost micro-CT, with the exception of spatial resolution, closely matched the benchmarks of other commercially available micro-CT scanners.¹⁵ Furthermore, our system may be able to outperform scanners that use other detector technologies, as these are often more susceptible to CT ring artifacts. Ring artifacts are caused by non-linear response of the x-ray detector elements (*i.e.*, fixed-pattern noise), which can be caused by defects of the detector itself, or the readout electronics.²⁵ In our lens-coupled, detector system, fixed-pattern noise is more likely to arise from discontinuities or defects in the surface of the phosphor screen and less likely to be present at the level of the camera's sensor. This is due to the high degree of quality control in the commercial, digital-photography industry, where faulty detectors are unlikely to be sold.

Additive manufacturing has gained popularity in the medical and dental sectors thanks to its ability to produce highly-porous, but strong, medical components. We have demonstrated that our system is able to interrogate titanium-alloy objects up to a total x-ray path length through titanium of 13 mm. This was shown by the accurate volumetric representation of a 17 mm diameter, gyroid-based, 80% porous scaffold. Furthermore, thanks to the relatively high difference between the CT number of air and titanium, internal-void features or defects were identifiable below the spatial resolution limits of the system. Fig 2-16C, E shows how voids below the resolution of the system were still noticeable due to partial-volume effects. Although these detected defects were not geometrically accurate, in practice, they show that the system could be effective at flagging internal defects, such as cracks or voids, that – if unnoticed – could seriously compromise the mechanical integrity of the 3D printed part.

Although our main objective was to demonstrate that our system could be used for routine NDT of titanium-alloy, 3D-printed parts, we believe its flexibility, portability, and versatility can be exploited in other applications. For example, the system could be used for volumetric imaging of archaeological samples in remote sites. In such cases, the included, full-frame, dSLR camera could also be used independently for sample documentation or 3D photogrammetry. Space exploration missions could also exploit our

proposed strategy, which, again, will allow the included camera to be employed in a variety of tasks.

As previously mentioned, our scanner could be used as a portable solution for non-destructive testing in remote sites. In this case, the required shielding might interfere with the transportation of the equipment and therefore the scanner might not be safe to operate under normal conditions. A solution for this scenario will be to define a designated controlled area where no personnel might be present. Similar strategies are often implemented in industrial, temporary sites or large-animal, veterinary radiography. Wireless-interlock technology could be used to define a perimeter at the boundary of the designated controlled area to avoid accidental exposure to ionizing radiation.

Another advantage of our system is that it can be easily updated. For instance, the system's camera could be periodically replaced as digital photography technology continues to evolve. Newer technologies could improve spatial resolution, reduce data transferring time, add additional capabilities to the system, or increase the lifespan of the image acquisition hardware. For example, mirrorless cameras do not require shutter replacement or maintenance, which may be needed for the Nikon D800 after 200,000 actuations. Additionally, the use of a mirrorless camera could enhance the fluoroscopy capabilities of our system, as these cameras may be better suited for video streaming. Finally, as demonstrated by our use of a general-purpose, x-ray source, we believe that our hardware, data-acquisition techniques, post-processing, and data reconstruction are compatible with most commercially available, x-ray units, which adds another layer of flexibility to our scanner.

From a cost-effectiveness standpoint, the main components of our scanner can be purchased at a fraction of the cost of commercially available, micro-CT scanners with comparable imaging characteristics. Even considering that in the industry the cost of the components might only represent a third of the cost of the device (\$ 85000 for a \$ 260000 scanner) our costs (< \$ 11000) are still significantly lower. We believe the cost-per-scan will be significantly lower when using our proposed CT scanner design, and will provide a cost-effective solution for non-destructive testing of medium-sized, titanium-alloy,

medical components. Furthermore, the possibility of using the included dSLR camera for other quality assurance tasks could further warrant the cost-effectiveness of the equipment. For example, the camera could be refocused to image the part directly and be used for photogrammetry, surface inspection, and geometric evaluation. Finally, the modular nature of the design will allow updates, upgrades, and replacement of individual components of the scanner without the need to replace the entire unit.

2.5 Conclusion

We have successfully designed, fabricated, and implemented a low-energy (80 kVp), micro-CT scanner for cost-effective, routine, non-destructive testing of porous, 3D-printed, titanium-alloy, medical components. We achieved cost-effective CT reconstructions of titanium, 3D-printed samples by acquiring data at lower x-ray potential and using a low-cost, lens-coupled, detector system. These reconstructions closely matched the geometric accuracy, uniformity, and linearity of relatively expensive commercial micro-CT scanners.

For our low-cost detector system, we utilized a phosphor screen, lens-coupled to a commercially available, consumer-grade, full-frame dSLR camera using a front-lit, tilted configuration. This configuration provided the light-collection efficiency required for CT imaging. The camera's sensor size (24 by 36 mm), the sensor technology (CMOS), and the lens light-transmission (f/1.4 fast lens) were key factors to ensure that the noise characteristics of the detector were dominated by photon counting statistics, rather than electronic or quantum noise.

Geometric distortions in the projection images acquired using the tilted-detector, lens-coupled, phosphor screen were successfully corrected using a Cartesian calibration grid. The effectiveness of the correction was evaluated at the level of the projection images and by assessing the performance of the scanner using a state-of-the-art, CT, quality assurance phantom. The performance evaluation of the system showed quantitatively accurate and geometrically stable reconstructions, with acceptable noise levels, and image quality.

The proposed design for our cost-effective scanner allowed non-destructive evaluation of medium-sized, titanium-alloy, 3D-printed parts with a thickness up to 13 mm of solid metal. Since this evaluation was done using test-objects, future work includes non-destructive testing of medical components with clinically relevant geometries. We anticipate that components with large amounts of solid metal will require a modified imaging protocol to overcome the penetration limits of the 80 kVp x-ray source.

2.6 Acknowledgments

Support for this project came from the Canadian Institutes of Health Research (Foundation Grant FDN 148474) and the Ontario Research Fund (Research Excellence RE-077-66). D.W.H. is the Dr. Sandy Kirkley Chair in Musculoskeletal Research within the Schulich School of Medicine & Dentistry at Western University. S.F.C. is supported in part by a Transdisciplinary Bone & Joint Training Award from the Collaborative Training Program in Musculoskeletal Health Research at The University of Western Ontario. The authors would also like to thank the technical staff at ADEISS for their assistance with the manufacturing of the titanium, 3D printed, phantoms used for this study, and Hristo Nikolov for his technical support conditioning the CT quality assurance phantom prior data acquisition and manufacturing of the scanner's frame.

2.7 References

1. De Chiffre L, Carmignato S, Kruth J-P, Schmitt R, Weckenmann A. Industrial applications of computed tomography. *CIRP annals*. 2014;63(2):655-677.
2. Ewert U, Fuchs T. Progress in Digital Industrial Radiology. Pt. 2, Computed tomography (CT). *Badania Nieniszczące i Diagnostyka*. 2017.
3. Warnett JM, Titarenko V, Kiraci E, et al. Towards in-process x-ray CT for dimensional metrology. *Measurement Science and Technology*. 2016;27(3):035401.
4. du Plessis A, le Roux SG, Guelpa A. Comparison of medical and industrial X-ray computed tomography for non-destructive testing. *Case Studies in Nondestructive Testing and Evaluation*. 2016;6:17-25.
5. Liao C-W, Fuh L-J, Shen Y-W, et al. Self-assembled micro-computed tomography for dental education. *PloS one*. 2018;13(12):e0209698.

6. de Oliveira Jr JM, Martins ACG. Construction and Test of Low Cost X-Ray Tomography Scanner for Physical-Chemical Analysis and Nondestructive Inspections. Paper presented at: AIP Conference Proceedings2009.
7. du Plessis A, Campbell N. Metrology of additively manufactured lattice structures by X-ray tomography. *Transactions on Additive Manufacturing Meets Medicine*. 2020;2(1).
8. du Plessis A, le Roux SG, Booysen G, Els J. Quality control of a laser additive manufactured medical implant by X-ray tomography. *3D Printing and Additive Manufacturing*. 2016;3(3):175-182.
9. Kim HK, Ahn JK, Cho G. Development of a lens-coupled CMOS detector for an X-ray inspection system. *Nuclear Instruments and Methods in Physics Research Section A: Accelerators, Spectrometers, Detectors and Associated Equipment*. 2005;545(1-2):210-216.
10. Lee SW, Kim HK, Cho G, Shin YH, Won YY. A 3-D X-ray microtomographic system with a CMOS image sensor. *IEEE transactions on nuclear science*. 2001;48(4):1503-1505.
11. Madden TJ, McGuigan W, Molitsky MJ, Naday I, McArthur A, Westbrook EM. Lens-Coupled CCD detector for x-ray crystallography. Paper presented at: 2006 IEEE Nuclear Science Symposium Conference Record2006.
12. Tate MW, Chamberlain D, Gruner SM. Area x-ray detector based on a lens-coupled charge-coupled device. *Review of scientific instruments*. 2005;76(8):081301.
13. Fan HX. *Lens-coupled x-ray imaging systems*, The University of Arizona; 2015.
14. Panna A, Gomella A, Harmon K, et al. Performance of low-cost X-ray area detectors with consumer digital cameras. *Journal of Instrumentation*. 2015;10(05):T05005.
15. Du LY, Umoh J, Nikolov HN, Pollmann SI, Lee T-Y, Holdsworth DW. A quality assurance phantom for the performance evaluation of volumetric micro-CT systems. *Physics in Medicine & Biology*. 2007;52(23):7087.
16. Li X, Zhang D, Liu B. A generic geometric calibration method for tomographic imaging systems with flat-panel detectors—A detailed implementation guide. *Medical physics*. 2010;37(7Part1):3844-3854.
17. Heikkila J. Geometric camera calibration using circular control points. *IEEE Transactions on pattern analysis and machine intelligence*. 2000;22(10):1066-1077.

18. Pollmann SI, Norley CJ, Yuan X, Holdsworth DW. Resolution enhancement of computed radiography images using two orthogonal tilts. Paper presented at: Medical Imaging 2012: Physics of Medical Imaging 2012.
19. Fahrig R, Moreau M, Holdsworth D. Three-dimensional computed tomographic reconstruction using a C-arm mounted XRII: Correction of image intensifier distortion. *Medical physics*. 1997;24(7):1097-1106.
20. Edey D, Pollmann S, Lorusso D, Drangova M, Flemming R, Holdsworth D. Extending the dynamic range of biomedical micro-computed tomography for application to geomaterials. *Journal of X-ray science and technology*. 2019;27(5):919-934.
21. Judy PF. The line spread function and modulation transfer function of a computed tomographic scanner. *Medical physics*. 1976;3(4):233-236.
22. Anam C, Fujibuchi T, Haryanto F, et al. Automated MTF measurement in CT images with a simple wire phantom. *Polish Journal of Medical Physics and Engineering*. 2019;25(3):179-187.
23. Droege RT, Morin RL. A practical method to measure the MTF of CT scanners. *Medical physics*. 1982;9(5):758-760.
24. Uesugi K, Hoshino M, Yagi N. Comparison of lens- and fiber-coupled CCD detectors for X-ray computed tomography. *Journal of synchrotron radiation*. 2011;18(2):217-223.
25. Šalplachta J, Zikmund T, Zemek M, et al. Complete Ring Artifacts Reduction Procedure for Lab-Based X-ray Nano CT Systems. *Sensors*. 2021;21(1):238.

Chapter 3

3 High-dynamic-range micro-CT for non-destructive testing of titanium 3D-printed medical components

(Submitted to the Journal of Medical Imaging on March 03, 2022)

Industrial micro-CT scanners are suitable for non-destructive testing (NDT) of metal, 3D-printed, medical components. Typically, these scanners are equipped with high-energy sources that require heavy x-ray shielding and costly infrastructure to operate safely, making routine NDT of medical components prohibitively expensive. Alternatively, portable fixed-current, low-cost x-ray units could be successfully implemented to perform CT-based NDT of 3D-printed medical parts in a sub-set of cases, provided that there is sufficient x-ray transmission for the CT reconstruction. A lack of signal (*i.e.*, low signal-to-noise ratio or SNR) – caused by areas of high attenuation in 2D-projection images of dense metal objects – leads to photon starvation and "under-ranging" artifacts that can make image-based NDT unreliable. Here we present the implementation of a dual-exposure technique devised to extend the dynamic range of a commercially available CT scanner equipped with a low-cost, fixed-current, low-energy (80 kVp) x-ray unit, increasing the SNR of high attenuation areas for NDT of titanium-alloy 3D-printed medical components. Our high-dynamic-range (HDR-CT) technique adequately combines projection images acquired at two exposure levels by modifying the integration-times of each protocol. Additionally, we evaluate the performance and describe the limitations of this dual-exposure HDR-CT technique by imaging a series of titanium-alloy test samples. One of the test samples was a resolution and conspicuity phantom specifically designed to assess the improvements in void visualization of the proposed methodology. The other test samples were four porous cylinders, 17 mm in diameter and 40 mm in length, with 60, 70, 80, and 90% nominal internal porosities. Our results demonstrate that the 12-bit native dynamic range of the CT scanner was increased to effective values of between 14 and 16 bits, generating reconstructions with improved contrast-to-noise and improved void conspicuity, when compared to conventional CT.

3.1 Introduction

Industrial micro-CT scanners are an effective tool for non-destructive testing (NDT) of parts fabricated for the automotive, aerospace, pharmaceutical, and medical industries.^{1,2} However, in some cases, routine NDT using these scanners can become prohibitively expensive.³ This is mainly due to the relatively-high cost of these scanners that are equipped with: high-energy x-ray sources (160 – 450 kVp); heavy x-ray shielding; and sophisticated, additional hardware. The Nikon XT H 225 industrial scanner is an example of such a system, weighing in at more than 2400 kg and costing more than \$750 000. On this system, NDT of a medium-sized, titanium, 3D-printed, part will typically cost over 50% of the manufacturing cost of the part.

Advancements in metal additive-manufacturing, more specifically, laser, powder-bed fusion (LPBF), have enabled the manufacturing of complex, bio-compatible, and mechanically-advantageous, medical components.⁴ These biocompatible components have common physical characteristics that make them more suitable for image-based NDT using x-ray sources at lower – and thereby more cost-effective – energies (80 kVp). These characteristics include: small-to-medium size; relatively low attenuation, biocompatible metals; porous constructs; and organic geometries or natural shapes. In most cases, these characteristics reduce the required x-ray penetration to resolve internal features in the part when using computed tomographic (CT) techniques. However, in other cases, the design of the part might include large portions of solid metal, making low-energy NDT unreliable.

Objects with large portions of solid metal are difficult to interrogate using a fixed x-ray exposure, due to the wide range of intensities over the full field-of-view. In these cases, the imaging parameters (*i.e.*, exposure time, kVp and tube current) are optimized so that the exposure does not exceed the dynamic range (DR) of the x-ray detector. As a result, areas of high-attenuation may become obscured in 2D projection images and will present an insufficient signal-to-noise ratio (SNR) – leading to photon starvation and “under-ranging” artifacts in the CT reconstruction. If the exposure time and/or tube current were increased in order to achieve sufficient SNR in these high-attenuating areas, the regions

of low-attenuation will exceed the dynamic range of the detector (*i.e.*, will be saturated), which will preclude accurate CT reconstruction.

To address this issue, several approaches have been proposed. Most involve hardware modifications to the x-ray detector, which are intended to extend the dynamic range of the device. For example, a detector could include multiple sensors, with different x-ray sensitivity, inside a single pixel.⁵ These specialized detectors could also be manufactured with special scintillators and pixel designs.⁶ Alternatively, software-based methods have also been proposed, in which case, the detector technology does not need to be altered. These techniques to extend the DR of optical detectors are based on the acquisition of multiple images with different x-ray energies or exposure levels.⁷⁻⁹ In both cases, at least two images – one with high energy/exposure and one with low energy/exposure – are combined in order to generate a composite, high-dynamic-range (HDR) projection. If appropriately combined, these projection images can be used to reconstruct volumetric data with improved image quality and diminished CT image artifacts.

Previously described, dual-exposure, high-dynamic-range CT (HDR-CT) methods have been designed for imaging of samples made of various materials with relatively-high differences in x-ray attenuation, at a lower energy (50 kVp), and multiple tube currents (mA).⁹ Therefore, it is still unclear if the same methodology can be used to improve the image quality of CT-based NDT of solid medical-grade alloys using an 80 kVp x-ray energy and a fixed-current (mA) protocol. It is also unclear what the limitations of fixed mA, dual-exposure, HDR-CT will be, as a method to diminish photon-starvation artifacts when imaging biomedical alloys.

In this study, we describe the first implementation of lower-energy (80 kVp), dual-exposure, HDR-CT for NDT of medical components fabricated in medical-grade, titanium alloy using LPBF. We describe the hardware and software required to acquire and process HDR projection data, and to obtain HDR-CT reconstructions using a commercially available, micro-CT scanner. We demonstrate the advantages of this novel technique by inspecting a series of 3D-printed, 17 mm diameter, cylindrical, porous scaffolds designed to have a range of internal porosity fraction (*e.g.*, 60, 70, 80, and

90%). Finally, we evaluate the performance limits of this technique by imaging a customized 3D printed titanium-alloy resolution phantom, which was designed to evaluate the penetration limits of HDR-CT for NDT of parts fabricated in this commonly used, medical-grade alloy.

3.2 Methods

3.2.1 Scanned Test Samples

Fig 3-1 shows the five test samples scanned for this study. They were manufactured in titanium-alloy (Ti6Al4V ELI-0406, Renishaw plc, United Kingdom, particle size 15-45 μm) using a laser powder-bed fusion 3D-printer for metal alloys (AM400, Renishaw plc, Wotton-under-Edge, United Kingdom) at the Additive Design in Surgical Solutions facility (ADEISS) in London, Canada.

Four objects were designed as cylinders, 17 mm in diameter and 40 mm in length, with nominal internal porosities of 60, 70, 80, and 90%. The internal porosity of these cylindrical test objects was achieved by modifying the thickness of a 6 mm³, sheet-based, gyroid unit. The computer-assisted design (CAD) for these test objects was performed in Blender (Version 2.79, blender.org, Amsterdam, Netherlands).

The other test sample was designed as a truncated cone, 17 mm high, with a 25 mm diameter base, and a 10 mm diameter top. Internally, it incorporated several series of deliberately prescribed voids of various widths, corresponding to a range of line-pairs (1.6 to 10 mm⁻¹), which extended from the top of the truncated cone to its base, along its longitudinal (*i.e.*, central) axis. It also incorporated a series of voids of various widths, centrally located, to determine void conspicuity. This resolution phantom was designed to evaluate the ability of the CT reconstructions to resolve known internal features of various sizes within the object as the cumulative x-ray path-length through the metal increases. Fig 3-2 shows the detailed schematics of this titanium-alloy resolution and conspicuity phantom.

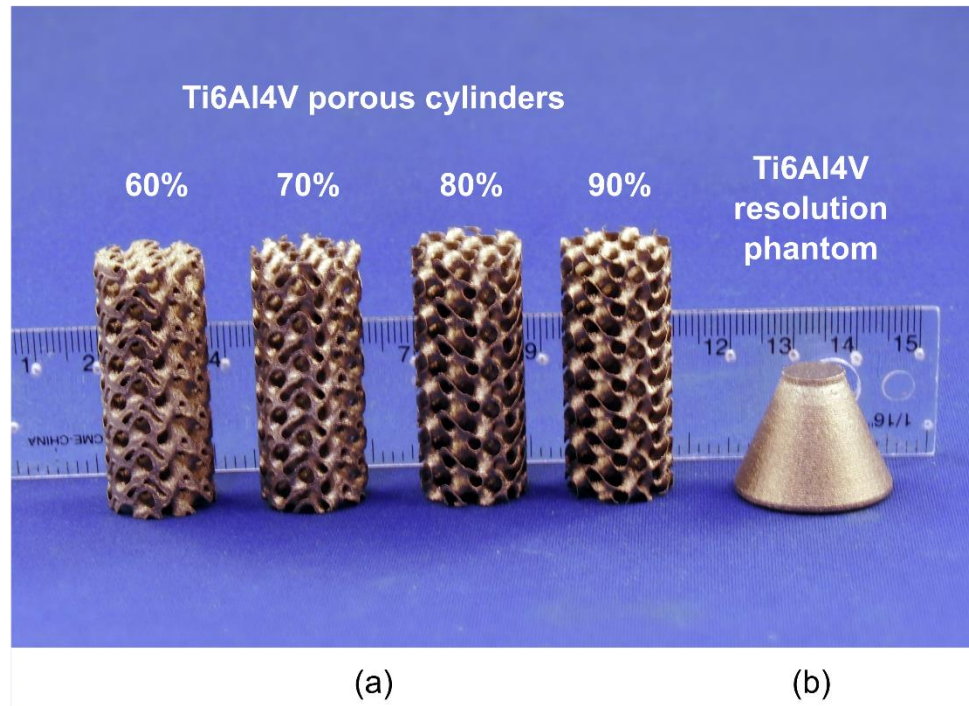


Fig 3-1. Test samples scanned in this project. (a) Titanium-alloy, gyroid-based, cylindrical samples with porosity fractions of 60, 70, 80 and 90%. (b) Titanium-alloy, resolution and conspicuity phantom. The internal features of this resolution phantom are described in Fig 3-2.

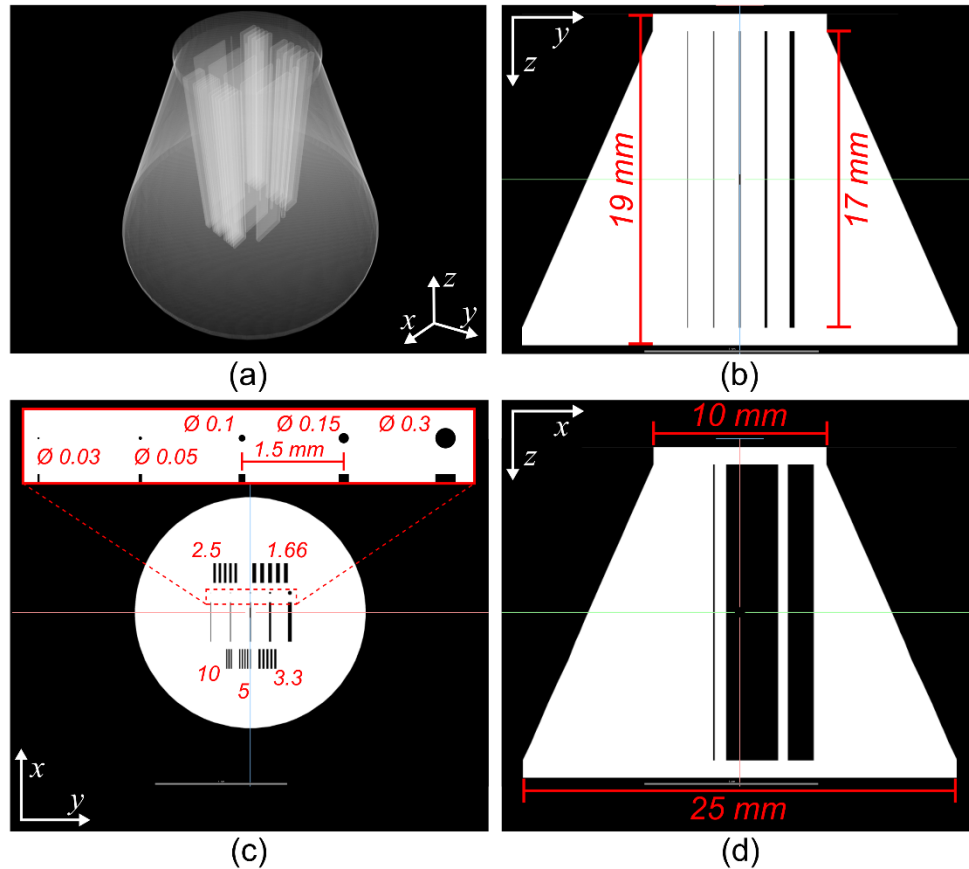


Fig 3-2. Detailed schematics of the titanium-alloy, resolution and conspicuity phantom. (a) Perspective view of the 3D-rendering of the computer-assisted design (CAD) with a transparency filter. (b) Central, trans-coronal, synthetic slice of the phantom's CAD. (c) Central, trans-axial, synthetic slice of the phantom's CAD illustrating the details of the internal voids. The bar patterns are described in lp mm^{-1} . All other measurements are shown in mm. (d) Central, trans-sagittal, synthetic slice of the phantom's CAD.

3.2.2 Dual-exposure Data Acquisition

Four image acquisition protocols with increasing integration times were designed to image the titanium-alloy, 3D-printed samples for this study. The micro-CT scanner (eXplore Locus RS X-ray, GE Healthcare; London, Canada) operated at a peak tube potential of 80 kVp and a fixed tube current of 400 μA . The first protocol had an integration time of 261.3 ms, which was optimized for the 12 bit x-ray detector, so that,

in an unattenuated region of the field-of-view the intensity values for each pixel did not exceed the maximum value of the detector (*i.e.*, intensity $< 2^{12} = 4096$ analog-to-digital units, ADU) of the eXplore Locus RS scanner. Unfortunately, it also meant that, during data acquisition, pixels obscured by highly attenuating regions on the image were underexposed. The integration time of the other three protocols were designed to have nominally 4, 8 and 16 (2^2 , 2^3 , and 2^4 respectively) times the exposure of the first protocol. For simplicity, in this manuscript we will refer to these protocols using the exposure value (EV) bracketing convention that is common to HDR optical photography. Here, EV0 represents the non-saturated, short acquisition that is optimized for the 12-bit detector, and EVn represents acquisitions with exposures that are nominally “2ⁿ” times the EV0 exposure. Table 3-1 summarizes the acquisition parameters for each EV protocol at 80 kVp and 400 μ A.

Table 3-1. Dual-exposure HDR protocols for the eXplore Locus RS X-ray scanner.

	EV0	EV2	EV3	EV4
Prescribed Integration Time (ms)	200	981	2026	4116
True Integration Time (ms)	261.3	1044	2090.6	4182.3
EVn-to-EV0 Exposure Ratio	1	4	8	16
Exposure Value/Bracketing (f-stop equivalent)	0	2	3	4

The integration times prescribed into the scanner’s control interface differed from the true integration times. X-ray exposure times were measured with a custom sensor timer circuit, comprised of a phototransistor (APDS-9930) in contact with a small phosphor scintillator (Lanex regular); timing was achieved with an interrupt-driven microprocessor (Arduino Uno). It was empirically observed that true integration times were, on average, 65 ms longer than the nominal prescribed times in the protocol. Therefore, the prescribed integration times for EV0, EV2, EV3, and EV4 were revised to be 200, 981, 2026, and 4116 ms, respectively.

For each protocol, the objects were placed in the field-of-view of the scanner using a custom-made holder in order to circumvent the re-homing of the specimen loading bed of the eXplore Locus RS scanner. This precaution was implemented because it was

determined that the linear bed mechanism was not able to return to the initial scanning position with sufficient accuracy, which resulted in registration errors when combining projection images for HDR radiography.

Each protocol, starting at EV0, collected a total of 200 projection images at 1-degree angular increments. For each subsequent EV protocol, the projection images were inspected to ensure that the EVn images were not completely saturated and that they included at least 50% of the sample's valid data. Dark-field images, required for offset correction, for each protocol were acquired in a way that matched that of each EV condition. Finally, only one bright-field image was acquired using the EV0 protocol, and this bright-field image was scaled appropriately for use with each HDR-CT reconstruction.

3.2.3 Dual-exposure HDR Projection Data Post-processing

HDR projection images were generated by combining pairs of EV0 and EVn data. Dark noise in each image of the pair was corrected using dark-fields (*i.e.*, images acquired with no x-rays on) acquired with their respective EV0 and EVn integration times. This was necessary to address the time-dependent aspect of dark-noise intensity. Next, the EV0 image was multiplied by a scaling factor (EVnf) in order to increase its signal value to match EVn. The scaling factor was calculated on a per-projection basis using the following formula:

$$EVnf = \frac{\text{mean intensity of EVn valid data}}{\text{mean intensity of EV0 valid data}} \quad (3.1)$$

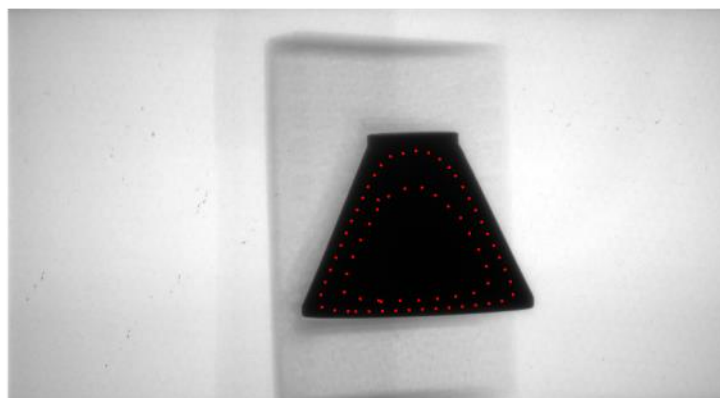
where both EV0 and EVn valid data were selected using a mask that included only pixels with intensities less than 95% of the saturation value in EVn, prior to dark-noise correction. For each pair, the dark-corrected, bright-field image acquired using the EV0 protocol was multiplied by the average of the set of EVnf values to synthesize a bright-field for the EVn acquisition. This “synthetic” bright-field image was later used to flat-field (*i.e.*, gain) correct the HDR projection images and to calculate the per-pixel I_0 values required for the CT reconstruction.

The final step was to combine the dark-noise corrected and intensity-matched EV0 (IM EV0) projection images with the corresponding set of dark-noise corrected EVn projections, using only valid data optimized from each. From visual inspection of thresholded EVn projections, it was determined that the EVn data was valid below 95% of the saturation value in those images. Similarly, for the intensity-matched EV0 projections, it was determined that regions in the EV0 images below the 75% saturation value were underexposed due to photon starvation at the detector, and should thus be discarded. Thus, pixels in EV0 image above the 75% saturation value were considered valid. For pixels values between these two thresholds (t_{95} and t_{75}), where both EV0 and EVn contained valid data, their intensities ($I_{x,y}$) were assigned using a weighted average using the following formula:

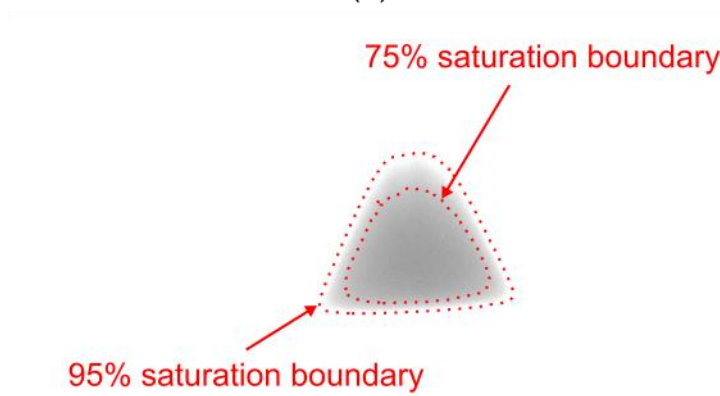
$$I_{x,y} = \left(\sin \left(\frac{EV0_{x,y} - t_{95}}{t_{95} - t_{75}} \right) \right)^2 EV0_{x,y} + \left(\cos \left(\frac{EV0_{x,y} - t_{95}}{t_{95} - t_{75}} \right) \right)^2 EVn_{x,y} \quad (3.2)$$

This $\sin^2 + \cos^2$ functional combination was chosen to minimize image stitching artifacts between the two data sets and to reduce the likelihood of discontinuity artifacts in the CT reconstructions, which have been described in the literature as a common limitation of HDR-CT.^{9,10} Fig 3-3A illustrates the location of the threshold boundaries in an EV0 projection image of the titanium-alloy resolution phantom, and Fig 3-3B shows the same boundaries in a EV4 projection image.

The final post-processing step, before CT reconstruction, involved the implementation of a combined, wavelet-Fourier, ring-artifact removal filter, following the protocol described by Münch *et al.*¹¹ This additional processing step was required to compensate for the reduced efficacy of the gain-and-offset correction achieved using the intensity-matched bright-field only.



(a)



(b)

Fig 3-3. Projection images used to generate HDR data illustrating the location of the 95% saturation and 75% saturation threshold boundaries. (a) Projection image of the titanium-alloy, resolution phantom acquired using the EV0 protocol. (b) Projection image of the titanium-alloy, resolution phantom acquired using the EV4 protocol.

3.2.4 CT Reconstruction and Data Analysis

The 200 projection images collected with the EV0 protocol and each of the HDR pairs (EV0, EVn) were used to perform CT reconstructions using a limited view, Parker-weighted, Feldkamp, Davis, and Kress (FDK), filtered-backprojection algorithm.¹² The voxel spacing of the reconstruction matrix was 90 x 90 x 90 μm . Prior to CT reconstruction, the projection images for the cylindrical samples were corrected for beam-hardening using the protocol described by Edey *et al.*¹³ Note that it was not possible to implement this correction in the reconstruction of the resolution phantom,

because the phantom diameter exceeded the thickness of the calibration object used for the beam-hardening correction. Furthermore, the correction parameters were different for each HDR image set, which made it difficult to compare the improvements in conspicuity with increasing penetration depth in this phantom that were due to HDR-CT alone.

Improvements in conspicuity with increasing penetration depth were assessed using the titanium-alloy resolution and conspicuity phantom described in Fig 3-2. Conspicuity was qualitatively evaluated using a trans-coronal CT slice plane perpendicular to the prismatic voids located inside the central region of the phantom – similar to the synthetic slice in Fig 3-2B. Visualization window and level were optimized by visual inspection to depict the best contrast for the EV0 reconstruction, which was compared with the HDR pairs.

The cylindrical test samples were used to evaluate the HDR-CT technique for highly porous geometries. These reconstructions were visually inspected in trans-sagittal CT slices in order to visualize any discontinuity artifacts caused by the HDR stitching. These slices were also interrogated using a line profile across the walls of the gyroid unit to evaluate improvements in image quality and signal-to-noise ratio between the conventional DR and the HDR volumes.

3.3 Results

3.3.1 Generation of HDR Projection Images

HDR projection images were successfully generated for all test samples, with the exception of the 90% porous cylinder, due to the high degree of overexposure of the projection images for protocols with integration times longer than that of EV0. Table 3-2 provides a summary of the EV0, EVn pairs used to generate HDR-CT reconstructions for each test sample. The 12-bit dynamic range (4096 ADU) of the detector was effectively extended to 14.18 (18514 ADU), 15.24 (38625 ADU), and 16.29 bits (80118 ADU) for EV2, EV3, and EV4 respectively.

Table 3-2. Summary of HDR-CT protocol-pairs per test sample.

	Conventional DR	EV0-EV2	EV0-EV3	EV0-EV4
DR hardware and (effective)	4096 ADU (12-bit detector)	18514 ADU (14.18 bits)	38625 ADU (15.24 bits)	80118 ADU (16.29 bits)
90% porous cylinder	Yes	No	No	No
80% porous cylinder	Yes	Yes	No	No
70% porous cylinder	Yes	Yes	Yes	No
60% porous cylinder	Yes	Yes	Yes	No
Resolution phantom	Yes	Yes	Yes	Yes

The intensity of the pixels ($HDR_{x,y}$) of a HDR EV0, EVn projection image pair were assigned following three conditions:

- If the pixel intensity in EVn, prior to dark correction, was greater than 95% of the saturation value, then it was categorized as invalid, and therefore, was assigned the value of the intensity-matched, dark-corrected EV0 image;
- If the pixel intensity value in EVn, prior to dark correction, was less than 75% of the saturation value, then it was categorized as valid, and therefore, was assigned the value of the dark-corrected EVn image;
- If the pixel intensity value in EVn, prior to dark correction, was in between 75% and 95% of the saturation value, then it was categorized as valid in both EV0 and EVn images, and therefore, was assigned a weighted-average value using the $\sin^2 + \cos^2 = 1$ identity, following Equation 3.2.

Fig 3-4 illustrates angle-dependent variations in the factors used to match EV0 intensity values for the 60% porous cylinder and the resolution and conspicuity phantom to each corresponding EVn on a per projection basis. These scaling factors showed the same variability between samples, and the variability trend described a specific signature for each object.

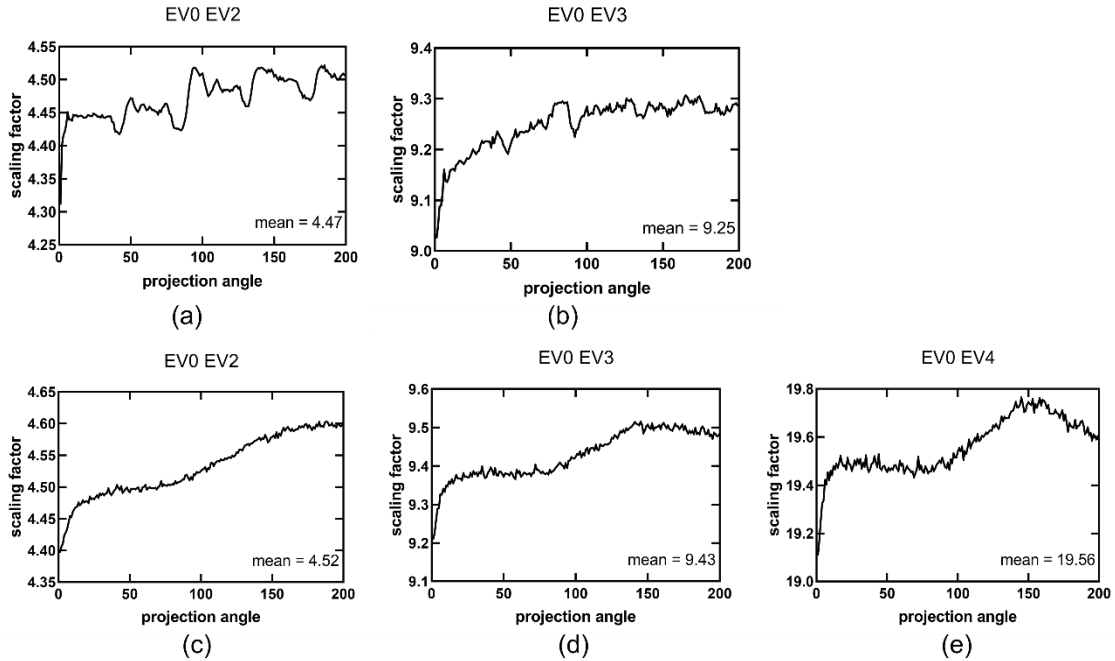


Fig 3-4. Scaling factors (Equation 3.1) for matching the intensity of EV0 projection images to EV_n as a function of projection angle for the 60% porosity cylinder for: (a) the EV0, EV2 HDR pair and (b) the EV0, EV3 HDR pair, and for the resolution and conspicuity phantom for: (c) the EV0, EV2 HDR pair; (d) the EV0, EV3 HDR pair; and (e) the EV0, EV4 HDR pair.

The EV0, EV_n combination strategy, in projection images, demonstrated the ability to remove any visually obvious stitching artifacts. Fig 3-5 shows the results of this procedure for one of the projection images of the resolution and conspicuity phantom, obtained using the EV0 and EV4 protocols. This figure illustrates that the EV0 data has been appropriately scaled to closely match the intensity values of EV4 below the 75% saturation threshold (t_{75}). Furthermore, the intensity-matched EV0 (IM EV0) data over the 95% saturation threshold (t_{95}) properly extrapolates the intensity values of EV4 for the region in EV4 where pixels reach the saturation point. The HDR intensity values in between the t_{75} and t_{95} thresholds were calculated using the previously described $\sin^2 + \cos^2 = 1$ identity (Equation 3.2). Fig 3-5C illustrates the effectiveness of this strategy in the combination of the two datasets, mainly due to the behavior of the identity near the thresholds, which ensured that the combined pixel values were properly weighted

between the IM EV0 and the EV4 data. Specifically, the intensity value of a combined HDR pixel was heavily weighted towards EV0 near the t_{95} threshold, and heavily weighted towards EV4 near the t_{75} threshold, with a smooth transition.

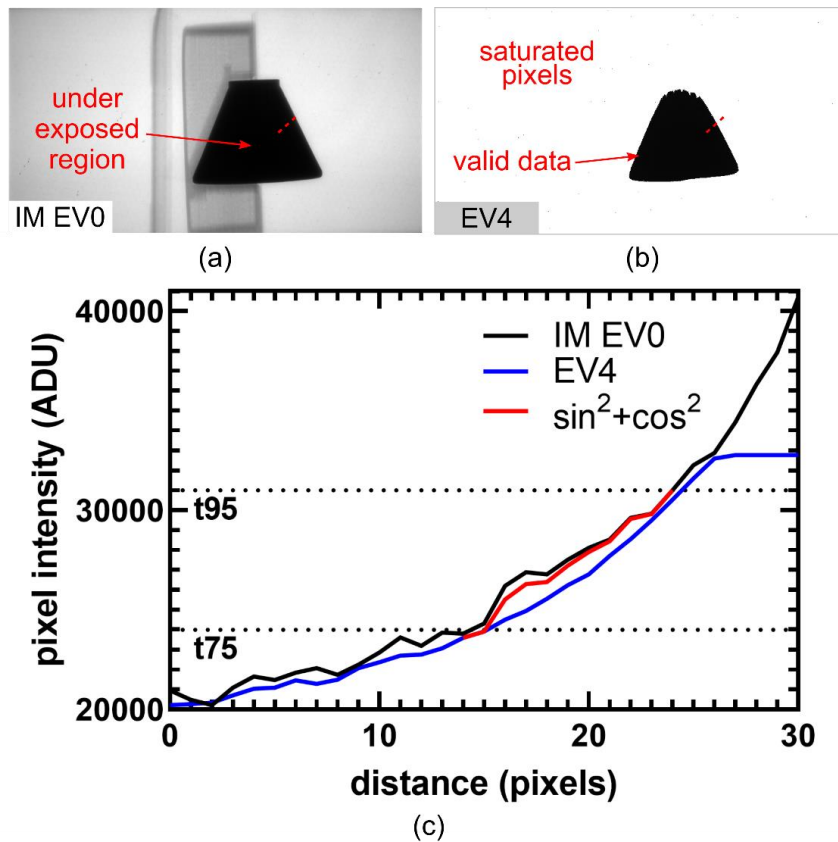


Fig 3-5. HDR strategy for the combination of EV0 with EVn projection images. (a) Dark-corrected, EV0 projection image of the resolution and conspicuity phantom, scaled to match the intensity values of EV4 (*i.e.*, intensity-matched, IM EV0). Due to a long ray path through the metal in the central region of the phantom, pixels were underexposed in the EV0 image and were discarded from the final HDR projection image. (b) Corresponding, dark-corrected EV4 projection, showing regions with saturated pixels and valid data. (c) Line profile through pixels marked by the red-dotted line in (a) and (b) showing the $\sin^2 + \cos^2$, weighted-average combination strategy for pixels with intensity values between the 95% (t_{95}) and 75% (t_{75}) saturation thresholds.

3.3.2 HDR-CT of Porous Cylindrical Samples

Fig 3-6 and Fig 3-7 depict trans-axial slices of the HDR reconstructed volumes using various combinations of EV0 and EVn scans. In all cases, the conventional-DR (i.e. single-exposure) reconstructions exhibit reduced image quality, mainly due to a reduced signal-to-noise ratio (SNR) within the titanium-alloy regions in the conventional-DR reconstruction. For the 60% porous, cylinder the differences in SNR between the EV0 EV2 and the EV0 EV3 HDR reconstructions were not as significant as the differences between the HDR and the conventional-DR volumes.

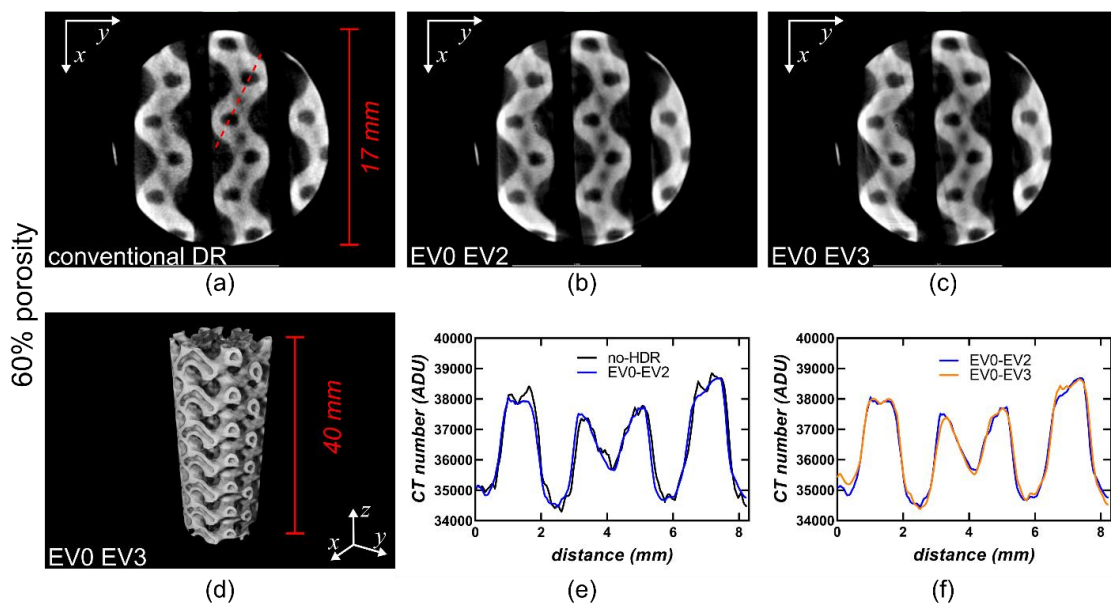


Fig 3-6. Results of the CT reconstructions for the 60% titanium-alloy, porous cylinder. (a), (b) and (c) show a trans-axial slice through the data for the conventional-DR, the EV0 EV2 pair, and the EV0 EV3 pair, respectively. (d) Shows a 3D-rendering of the data in a perspective view. (e) and (f) show the voxel values through a line-profile following the red-dotted line in (a) to compare the differences in signal-to-noise ratio between datasets.

Fig 3-7 illustrates the SNR improvement for the 70% and 80% porous cylinders between the conventional-DR reconstructions and the HDR reconstructions with the longest integration times for each object. The improvements in SNR were more pronounced for the 70% porous cylinder, whereas for the 80% porous cylinder, the improvements in

image quality were barely noticeable. These results indicate that for samples with low total x-ray path-lengths through solid metal HDR might not be necessary.

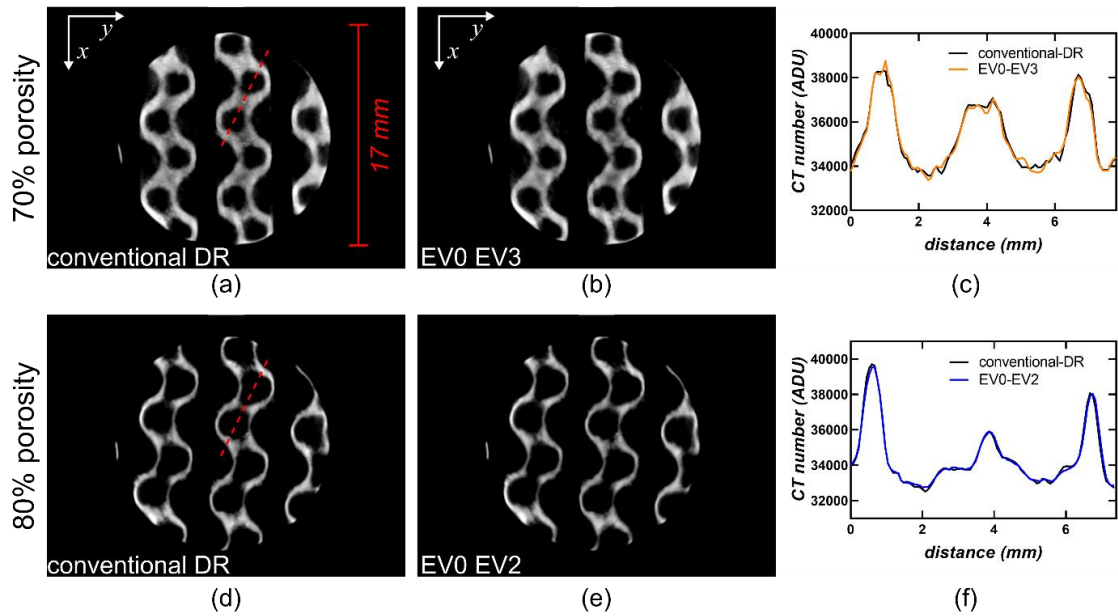


Fig 3-7. Results of the CT reconstructions for the 70% and 80% titanium-alloy, porous cylinders. (a) and (b) show a trans-axial slice through the 70% porous, cylinder for the conventional-DR and the EV0 EV3 pair, respectively. (d) and (e) show a trans-axial slice through the 80% porous, cylinder for the conventional-DR and the EV0 EV2 pair, respectively. (c) and (f) show the voxel values through a line-profile following the red-dotted line in (a) and (d) to compare the differences in signal-to-noise ratio between the respective datasets.

3.3.3 HDR-CT of Resolution Phantom

The resolution and conspicuity phantom was specifically designed to evaluate the visualization of internal voids for varying total x-ray path-lengths through a block of solid titanium-alloy. This was assessed using a trans-coronal, slice placed at the center of the phantom and perpendicular to the prismatic voids that ran through its longitudinal axis. The diameter of the phantom, at the void conspicuity limit for the 30 μm wide prism, was used as a reference to describe the total x-ray path-length limit for each CT reconstruction. The void conspicuity limit was reached at a diameter of 14.45 mm for the

conventional-DR reconstruction. The EV0 EV2 HDR reconstruction improved this conspicuity limit up to 16.08 mm, and the EV0 EV3 HDR up to 19.84 mm. For the EV0 EV4 reconstruction, further improvements to the void conspicuity limit would be challenging to assess. Unfortunately, the EV0 EV4 reconstruction suffered from artifacts caused by the increased dark-noise collected at this 16x longer exposure. Fig 3-8F shows the improved CT number accuracy in a profile-line through the voxels located along the longitudinal axis of the phantom, and within one of the prismatic voids, which contributes to the observed improvements in void visualization for the HDR-CT reconstructions.

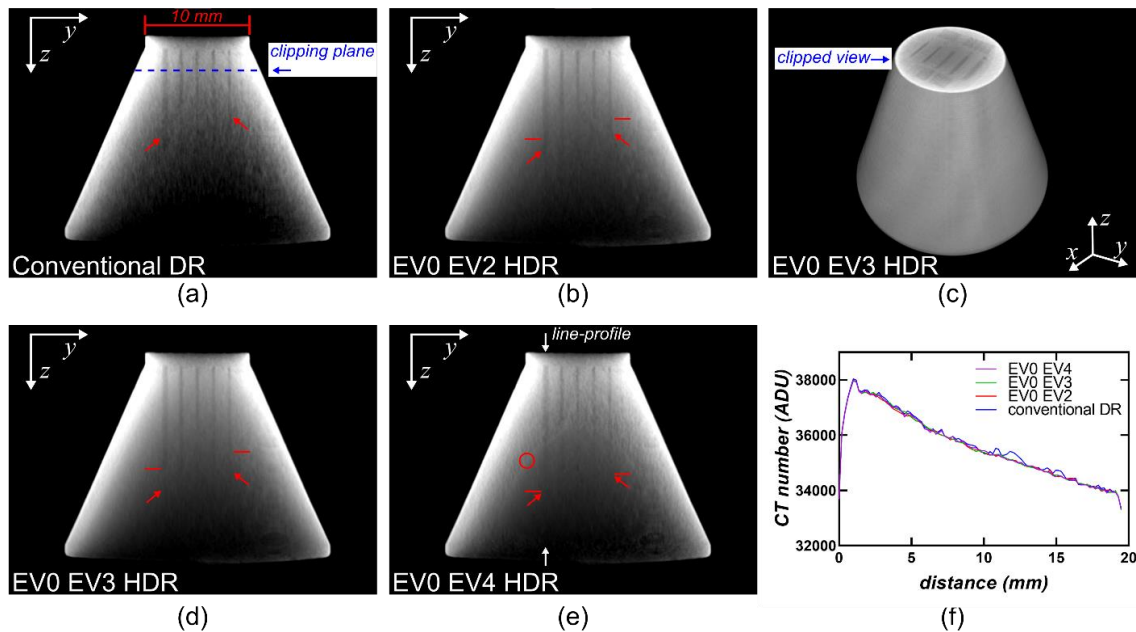


Fig 3-8. CT reconstructions for the resolution and conspicuity phantom. (a), (b), (d), and (e) show a trans-coronal slice through the reconstructed data for the conventional-DR, the EV0 EV2, the EV0 EV3, and EV0 EV4 pairs, respectively. The red arrows in these images describe the location of the void conspicuity limit for the 30 μ m wide and the 300 μ m wide prismatic voids. The red horizontal lines mark the void conspicuity limit reached by the immediately shorter HDR reconstruction. The red circle in (e) shows the location of a discontinuity artifact for the EV0 EV4 dataset. (c) Shows a 3D rendering of a perspective view of the EV0 EV3 HDR reconstruction with the top portion of the phantom clipped at the level marked in

(a). (f) Shows the intensity values of voxels in a profile-line located along the longitudinal axis of the phantom, and within the 300 μm wide prismatic void.

3.4 Discussion

The use of a low-energy (80 kVp) x-ray source for imaging-based, non-destructive testing (NDT) of medium-sized, titanium-alloy, biomedical components is a promising alternative for routine, cost-effective, quality control in the additive manufacturing industry. Unfortunately, this solution suffers from limitations due to the low dynamic range (DR) of commercially available micro-CT scanners. Here, we demonstrate that NDT can be enhanced by implementing a software-based, dual-exposure, HDR radiography technique that requires no hardware modifications to the scanner. This integration-time-dependent HDR strategy takes advantage of the linear response of the x-ray detector, which allows the extension of its dynamic range by modifying the data acquisition process, and strategically combining two images with varying integration times – *i.e.*, a short integration-time EV0, and a long integration-time EVn. We have demonstrated that the dynamic range of a micro-CT scanner with a 12-bit detector can be extended up to an effective 16 bits, resulting in CT reconstructions of test samples with improved contrast-to-noise characteristics.

Our novel HDR method was designed under the constraint that cost-effective, routine, NDT is more likely to be achieved using x-ray sources with a relatively low-cost, requiring minimal infrastructure. These x-ray sources operate at lower energies (< 80 kVp) and at fixed (*i.e.*, maximum) tube currents. For this reason, our implementation of an integration-time-dependent, dual-exposure, HDR-CT technique differs from the strategies described by Sisniega⁹ and Chen,⁷ who instead, modified the imaging conditions by varying the tube current, and tube energy respectively. Although our results showed that the reconstructions that included data acquired with 4x (EV0 EV2) and 8x (EV0 EV3) the integration time of a conventional-DR CT (EV0) presented improved image quality, for longer integration times, 16x (EV0 EV4), the proposed technique was susceptible to artifacts related to increased dark-noise, image lag and ghosting.¹⁴ Image lag and ghosting was especially detrimental for cases where the pixel switched from an over-saturated state to linear response from one projection image to the other, which

could last up to 4.5 seconds. Artifacts generated due to image lag and ghosting are likely to be system specific, and some detector technologies might be less susceptible to both phenomena.

Discontinuity artifacts in HDR-CT reconstructions have been described as one of the main limitations of dual-exposure, HDR techniques.⁷⁻¹⁰ During the development of our methodology, several strategies were tested to combine the EV0 and EVn pairs, but the described $\sin^2 + \cos^2$, weighted-average strategy was the only one to render acceptable results. We believe this is, in part, due to the significant differences in the signal-to-noise ratio between the EV0 and the EVn datasets. Any direct stitching between EVn data and intensity-matched EV0 data produced noticeable discontinuity artifacts in the CT reconstructions. Avoiding these discontinuity artifacts was especially challenging for the EV0 EV4 HDR pair, as the interface between valid and overexposed data was always located within the body of the scanned part. For this reason, we do not recommend the acquisition of EVn images where a significant portion of the object in the projection images is overexposed.

Another potential source of these discontinuity artifacts is the incorrect matching of EV0 and EVn intensity values. In our experiments, the best strategy was to calculate the mean intensity of pixels containing valid data in both data sets using a view-angle dependent approach. Fig 3-4 illustrates how the scaling factors varied as a function of projection angle for the resolution and conspicuity phantom data. It was observed that these fluctuations in scaling factors followed a similar trend for the various EVn datasets, but were highly object dependent. We hypothesize that these fluctuations are caused by the complex relationship between the object geometry and image lag and ghosting artifacts. Fortunately, both of our strategies to prevent discontinuity artifacts yielded good results, with the exception of the EV0 EV4 HDR pair, where artifacts were still conspicuous in some regions of the reconstructed volume.

The improvements in image quality in the HDR-CT reconstructions were derived from a higher signal-to-noise ratio in the areas of the image that were otherwise obscured by large volumes of titanium-alloy in our test samples. For instance, in the case of the

resolution and conspicuity phantom, HDR-CT increased void conspicuity from an x-ray path length of 14.45 mm (in conventional-DR), up to 19.8 mm through solid titanium-alloy. This 37% improvement in penetration depth for 80 kVp, fixed-current NDT could be a critical improvement for the evaluation of medium-sized medical components that otherwise will suffer from photon-starvation artifacts in regions with a total x-ray path length over 19.8 mm. Fortunately, most medium-sized, titanium-alloy, 3D-printed, medical components are designed with internal geometries with a high porosity fraction. In such cases, which are similar to the porous cylinders imaged in this study, the degree to which the integration times are extended could be dictated by the density of the object and the path length through which the x-rays must travel.

3.5 Conclusion

We have successfully implemented a low-energy (80 kVp), fixed tube-current, HDR-CT strategy for cost-effective, routine, non-destructive testing of titanium-alloy 3D-printed parts. We were able to generate high-dynamic-range CT reconstructions of titanium-alloy 3D-printed samples by successfully combining projection images acquired at two exposure levels, achieved by modifying the integration-times of each protocol. These projection images increased the dynamic range of the x-ray detector from its native 12 bits to effective values of 14.18, 15.24, and 16.29 bits. The CT reconstructions generated using these high-dynamic-range projection images showed improved contrast-to-noise and an improved void visualization, when compared to conventional dynamic-range CT.

Projection images acquired with a short integration-time were successfully combined with their long integration-time pairs, using two strategies (1) by carefully scaling the intensity values of the short-timed exposure in a per projection-angle basis, and (2) by smoothing the transition between data sets across a range of intensity values using an appropriate weighted average.

The proposed exposure-time dependent, dual-exposure, HDR-CT method improved the contrast-to-noise and performance of NDT for medium-sized, titanium-alloy, 3D printed parts. Furthermore, this technique provided a 37% improvement in conspicuity of internal defects in a resolution phantom, in comparison to conventional-DR CT. Future work

includes the evaluation of the technique using more clinically relevant geometries, and the investigation of HDR correction for a sub-set of the projection images, as well as a more rigorous *a priori* determination of the degree to which integration times must be extended for non-destructive testing of titanium-alloy, medical components fabricated using additive manufacturing.

3.6 Acknowledgments

Support for this project came from the Canadian Institutes of Health Research (Foundation Grant FDN 148474) and the Ontario Research Fund (Research Excellence RE-077-66). D.W.H. is the Dr. Sandy Kirkley Chair in Musculoskeletal Research within the Schulich School of Medicine & Dentistry at Western University. S.F.C. is supported in part by a Transdisciplinary Bone & Joint Training Award from the Collaborative Training Program in Musculoskeletal Health Research at The University of Western Ontario. The authors would also like to thank the technical staff at ADEISS for their assistance with the manufacturing of the titanium, 3D printed, phantoms used for this study.

3.7 References

1. De Chiffre L, Carmignato S, Kruth J-P, Schmitt R, Weckenmann A. Industrial applications of computed tomography. *CIRP annals*. 2014;63(2):655-677.
2. Ewert U, Fuchs T. Progress in Digital Industrial Radiology. Pt. 2, Computed tomography (CT). *Badania Nieniszczące i Diagnostyka*. 2017.
3. du Plessis A, le Roux SG, Guelpa A. Comparison of medical and industrial X-ray computed tomography for non-destructive testing. *Case Studies in Nondestructive Testing and Evaluation*. 2016;6:17-25.
4. Lowther M, Louth S, Davey A, et al. Clinical, industrial, and research perspectives on powder bed fusion additively manufactured metal implants. *Additive Manufacturing*. 2019;28:565-584.
5. Fox T, Nisius D, Duncan M, Duncan M. Dynamic range extension of x-ray imaging system used in non-invasive inspection of contraband in vehicles, involves amplifying identical samples of x-ray beams using respective gain values, and forming x-ray image. *US Patent*. 2005.2005047546-A2005047541.

6. Nittoh K, Oyaizu E, Sakurai T, Yoshida T, Mochiki K-I. Extension of dynamic range in X-ray radiography using multi-color scintillation detector. *Nuclear Instruments and Methods in Physics Research Section A: Accelerators, Spectrometers, Detectors and Associated Equipment*. 2003;501(2-3):615-622.
7. Chen P, Han Y, Pan J. High-dynamic-range CT reconstruction based on varying tube-voltage imaging. *PLoS One*. 2015;10(11):e0141789.
8. Li Y, Han Y, Chen P. X-ray energy self-adaption high dynamic range (HDR) imaging based on linear constraints with variable energy. *IEEE Photonics Journal*. 2017;10(2):1-14.
9. Sisniega A, Abella M, Desco M, Vaquero J. Dual-exposure technique for extending the dynamic range of x-ray flat panel detectors. *Physics in Medicine & Biology*. 2013;59(2):421.
10. Sukovic P, Clinthorne NH. A method for extending the dynamic range of flat panel imagers for use in cone beam computed tomography. Paper presented at: 2001 IEEE Nuclear Science Symposium Conference Record (Cat. No. 01CH37310)2001.
11. Münch B, Trtik P, Marone F, Stampanoni M. Stripe and ring artifact removal with combined wavelet—Fourier filtering. *Optics express*. 2009;17(10):8567-8591.
12. Parker DL. Optimal short scan convolution reconstruction for fan beam CT. *Medical physics*. 1982;9(2):254-257.
13. Edey D, Pollmann S, Lorusso D, Drangova M, Flemming R, Holdsworth D. Extending the dynamic range of biomedical micro-computed tomography for application to geomaterials. *Journal of X-ray science and technology*. 2019;27(5):919-934.
14. Mail N, O'Brien P, Pang G. Lag correction model and ghosting analysis for an indirect-conversion flat-panel imager. *Journal of applied clinical medical physics*. 2007;8(3):137-146.

Chapter 4

4 3D printed large-area focused grid for scatter reduction in cone-beam CT

(Under review - submitted to Medical Physics on September 06, 2021)

Cone-beam CT (CBCT) systems acquire clinically relevant volumetric data faster than fan-beam or multi-slice CT due to their optimized beam geometry. For such systems, scattered radiation remains a source of image quality degradation leading to increased noise, image artifacts, and CT number inaccuracies. Recent advances in metal additive manufacturing allow the production of highly focused anti-scatter grids (2D-ASGs) that can be used to reduce scatter intensity, while preserving primary radiation transmission. Here, we present the first implementation of a large-area, 2D-ASG for flat-panel CBCT, including grid-line artifact removal and related improvements in image quality. A 245 x 194 x 10 mm 2D-ASG was manufactured from chrome-cobalt alloy using laser powder-bed fusion (LPBF) (AM-400; Renishaw plc, New Mills Wotton-under-Edge, UK). The 2D-ASG had a square profile with a pitch of 9.09 lines/cm and 10:1 grid-ratio. The nominal 0.1 mm grid septa were focused to a 732 mm x-ray source to optimize primary x-ray transmission and reduce grid-line shadowing at the detector. Powder-bed fusion ensured the structural stability of the ASG with no need for additional inter-septal support. The 2D-ASG was coupled to a 0.139 mm element pitch flat-panel detector (DRX 3543, Carestream Health) and proper alignment was confirmed by consistent grid-line shadow thickness across the whole detector array. A 154 mm diameter CBCT image-quality-assurance phantom was imaged using a rotary stage and a ceiling-mounted, x-ray unit (Proteus XR/a, GE Medical Systems, 80kVp, 0.5mAs). Grid-line artifacts were removed using a combination of exposure-dependent gain correction and spatial-frequency, Fourier filtering. Projections were reconstructed using a Parker-weighted, FDK algorithm and voxels were spatially averaged to 357 x 357 x 595 μm to improve the signal-to-noise characteristics of the CBCT reconstruction. Finally, in order to compare image-quality with and without scatter, the phantom was scanned again under the same CBCT conditions but with no 2D-ASG. No additional anti-scatter (*i.e.*, air-gap, bowtie

filtration) strategies were used to evaluate the effects in image quality caused by the 2D-ASG alone. The large-area, 2D-ASG prototype was successfully designed and manufactured using LPBF. CBCT image-quality improvements using the 2D-ASG included: an overall 16.37% CNR increase across the volume; up to 60.34% CNR increase for low-contrast inserts inside the contrast plate of the QA phantom; and a 65% reduction of cupping artifact in axial profiles of water-filled cross sections of the phantom. Advanced image processing strategies to remove grid line artifacts did not affect the spatial resolution or geometric accuracy of the system. LPBF can be used to manufacture highly efficient, 2D-focused ASGs that can be easily coupled to clinical, flat-panel detectors. The implementation of ASGs in CBCT leads to reduced scatter-related artifacts, improved CT number accuracy, and enhanced CNR with no increased equivalent-dose to the patient. Further improvements to image quality might be achieved with a combination of scatter-correction algorithms and iterative-reconstruction strategies. Finally, clinical applications where other scatter removal strategies are unfeasible, might now achieve superior soft-tissue visualization and quantitative capabilities.

4.1 Introduction

Cone-beam computed tomography (CBCT) emerged during the late 1990s as a volumetric, high-resolution, low-dose, imaging tool, ideally suited for guided radiation therapy, cranial angiography, and maxillofacial radiology.¹⁻³ Currently, CBCT is increasingly supplanting traditional CT modalities in many clinical applications, such as respiratory or cardiac imaging. Compared to traditional CT, CBCT maintains and improves spatial resolution while reducing costs, scanning times, and patient dose.⁴⁻⁷ However, the large field-of-view of CBCT geometries leads to increased detected scatter fraction (*i.e.*, 0.05-0.15, for fan-beam and spiral CT, versus 0.4-2.0 for CBCT), which degrades image quality, especially in high scatter-to-primary (SPR) scenarios.⁸⁻¹¹ Scatter contamination of the projection images results in tomographic reconstructions with reduced contrast-to-noise ratio (CNR), worsened CT number inaccuracies, and increased shading artifacts.¹²⁻¹⁶ Clinically, scatter-induced image artifacts and non-linearities translate into limited soft-tissue visualization,^{17,18} reduced efficacy of image-guided

interventions,^{19,20} incompatibility with quantitative analysis,^{14,21} and can lead to an inaccurate diagnosis or misdiagnosis.^{22,23}

Therefore, it is essential to include scatter-ameliorating strategies into CBCT system design, without increasing patient dose. In general, scatter-reduction strategies can be divided into two approaches: (1) hardware techniques to reject scatter and (2) software techniques to correct scatter.^{21,24,25} In practice, hardware techniques do not completely suppress the scatter reaching the detector and, similarly, no software methods correct artifacts perfectly. For these reasons, an optimal scatter correction is likely to combine both hardware and software approaches.²⁶ Hardware methods such as the air-gap technique, bowtie filters, or anti-scatter grids reduce the number of scattered x-rays reaching the detector.²⁷ Software methods derive or estimate the scatter field using models based on physical, empirical, or consistency criteria to correct the acquired projection data.²⁸ The major drawbacks of software-based methods are related to their computational intensity, which might prevent real-time applications. Additionally, they often require *a priori* knowledge of the material and density distributions of the object – requiring additional radiation dose.²⁷⁻²⁹ Model-based scatter correction methods, software-based methods, that do not require additional dose, have recently shown to provide improvements in CT number accuracy and scatter-related artifact reduction.^{27,28} Yet, these methods may not reach the levels of scatter correction required for quantitative applications.³⁰ In contrast, hardware methods do not require *a priori* knowledge about the object, but cannot always be implemented due to space restrictions (*e.g.*, air-gap) or require additional radiation dose to account for primary x-ray intensity loss (*e.g.*, traditional anti-scatter grids with inter-septal spacers).^{24,27,29,31,32} Furthermore, failure to correct artifacts introduced by a grid can compromise the potential improvements in image quality.^{33,34} However, a new generation of metal, 3D-printed, anti-scatter grids, which are the focus of this manuscript, offer a promising solution for hardware-based scatter rejection in CBCT.^{24,35}

Anti-scatter grids are mechanical devices that are placed directly in front of the x-ray detector to capture scattered photons while preserving primary x-rays.^{24,35-38} Traditionally, these grids have been manufactured using a one-dimensional array of thin

(approximately 15-46 μm), lead septa supported by aluminum or fiber spacers.^{39,40} As previously mentioned, the inter-septal support material has the disadvantage of attenuating primary x-rays that might subject the patient to a higher radiation dose in order to maintain image quality.^{27,41} Even using sophisticated fabrication methods like the ones described by Lehmann *et al.*⁴² and Goldenberg, BG *et al.*⁴³ this limitation cannot be overcome. Recent advancements in additive manufacturing (AM) and laser, powder-bed fusion (LPBF) allow the fabrication of novel, two-dimensional focused grids (2D-ASGs) that do not require inter-septal support.^{24,33,35} These 3D structures are built by selective melting of metal powder, deposited in layers, using a high-energy, power-density laser.⁴⁴⁻⁴⁶ 2D-ASGs provide improved scatter-removal characteristics over 1D-ASGs, and increase primary transmission up to as much as 70% of the incident x-ray beam.²⁴ These novel grids achieve this additional transmission by focusing the grid septa towards the x-ray source focal spot and inherently eliminate geometrical distortion of the grid shadow across the detector.^{24,38,39}

2D-ASGs prototypes have been shown to improve image contrast and reduce scatter-related artifacts for CBCT systems.^{24,35} However, uncertainties persist with regards to the impact that grid septa might have on the projection data. For instance, detector elements covered by grid-septa receive a reduced count of x-ray photons (*i.e.*, x-ray fluence), leading to grid-line artifacts. Furthermore, signal leaking from the surrounding, non-affected elements causes exposure-dependent gain variations. The combination of both effects – reduced fluence and signal leakage – renders conventional pixel-to-pixel variation correction methods ineffective.^{47,48} In such a case, the CBCT reconstruction can be affected by severe ring artifacts that impair radiological interpretation and analysis.^{33,47} Another limitation of recently investigated 2D-ASG prototypes relates to their coverage area of the detector. Although the 3D printing of focused, anti-scatter grids, for scatter rejection has been advertised by several private companies (*e.g.*, Dunlee, Nuclear-shields, H.C. Starck Solutions, Mikro Systems, and Wolfmet), to our knowledge, there is no report in the literature for the design and evaluation of a highly focused anti-scatter grid covering a significant area of a flat-panel detector in a full-beam CBCT geometry. The largest prototype described in the literature for a half-beam CBCT geometry, a grid of size 20 by 3 cm,³³ cannot be clinically implemented due to its relatively small field-of-

view. Furthermore, it remains unclear how residual stresses, which are characteristic of LPBF, might affect the fabrication of large-area grids (*e.g.*, build failure due to object-substrate delamination) or during subsequent clinical use (*e.g.*, geometric distortion or crack formation).^{44,49}

We present the complete process of design, manufacturing, and implementation of a large-area, 24.5 by 19.4 cm, focused 2D-ASG, and evaluate its quantitative effects in CBCT image quality. We first developed an open-source, parametric modelling module to generate a focused-grid, computer-aided design (CAD). Based on this CAD model, we optimized the 3D printing parameters of a commercially available laser powder-bed fusion system to achieve geometric stability and thin septa in the grid. Using clinically available equipment, we acquired CBCT data of a quality assurance phantom, and assess image quality with and without the anti-scatter device. Finally, we describe the image processing techniques required to successfully correct grid-line artifacts and describe the improvements in CBCT image contrast-to-noise ratio, CT number accuracy, and shading artifacts. Our results show that two-dimensional, focused, 3D-printed, metal grids provide an effective solution for scatter rejection in large-area CBCT.

4.2 Methods

4.2.1 2D Anti-scatter grid parametric modelling

The computational power required to create and manipulate CAD files is directly related to the number of vertices of the 3D model.⁵⁰ Large-area 2D-ASGs require many unique cells, because each cell is oriented at a unique angle along a ray between the focal spot of the x-ray source and each point on the detector. This unique angular orientation makes it impossible to simply replicate a single septal cell as a unit cell. A minimum of 12 vertices is required to define each septal cell of the 2D-ASG. Our large-area grid has 219 by 172 septal cells, requiring close to half a million vertices in the CAD file. Conventional CAD modelling packages and methods typically require at least an order of magnitude more than the minimum number of vertices in order to define the geometry sufficiently for Boolean operations. Even if the four-fold symmetry of this grid were exploited to reduce the number of vertices, this number remains computationally unwieldy.⁵¹ Additionally,

this division of the geometry into quadrants requires the extra step of geometric transformations and stitching them together into a final assembly. Fig 4-1 shows a diagram of the basic geometry and features of the novel grid design.

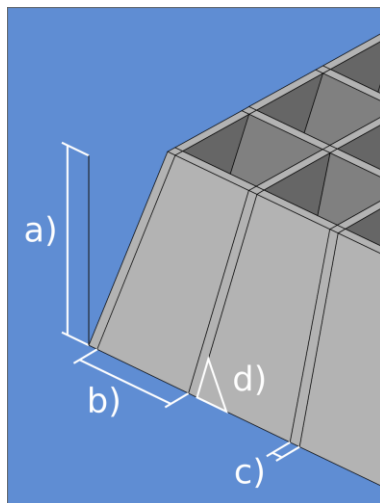


Fig 4-1. Close-up of 2D-ASG septal cell. (a) grid height, (b) element size, (c) septal thickness, and (d) inclination angle to match CBCT geometry.

Changing any geometric parameter of the grid will require recalculation and regeneration of a completely new drawing of the CAD model. Redrawing of the grid may be necessary to accommodate changes in x-ray detector dimensions, detector element pitch, and source-to-detector distance of the CBCT system, among other design constraints. In order to circumvent the computational power and modelling time challenges inherent in using conventional 3D modelling packages,⁵¹ we have designed and implemented a parametric modelling node-tree technique. This was achieved using a Python-based solution in the open-source software (Blender 2.8). The node-tree required seven user-defined parameters (Table 4-1) to generate an optimized stereolithographic file (STL) compatible with a commercial LPBF printing interface (QuantAM, Renishaw).

Table 4-1. 2D-ASG design parameters

Parametric modelling inputs	2D-ASG design parameters
Frame length	245 mm
Frame width	194 mm
Cell aperture size	1 mm
Septal thickness	0.1 mm
Frame height	10 mm
Build-plate clearance	1 mm
Focal spot distance	732 mm

Despite the advantages of the parametric tool being able to generate grids with any combination of parameters, limitations of the design are mandated by the additive manufacturing process, described below. For instance, the size of the grid frame cannot exceed the limits of the build-plate of the LPBF machine. Fine-tuning of the laser scan time is required for various combinations of powder particles and laser spot size to attain mechanically stable thin septa.⁵² In our implementation, particle size and scanning time, limited septal thickness to $\sim 100 \mu\text{m}$, and frame size to 250 by 200 mm (Fig 4-2). Prior to 3D printing, mounting flanges and a label were added to the grid frame to aid with installation and identification of the device.

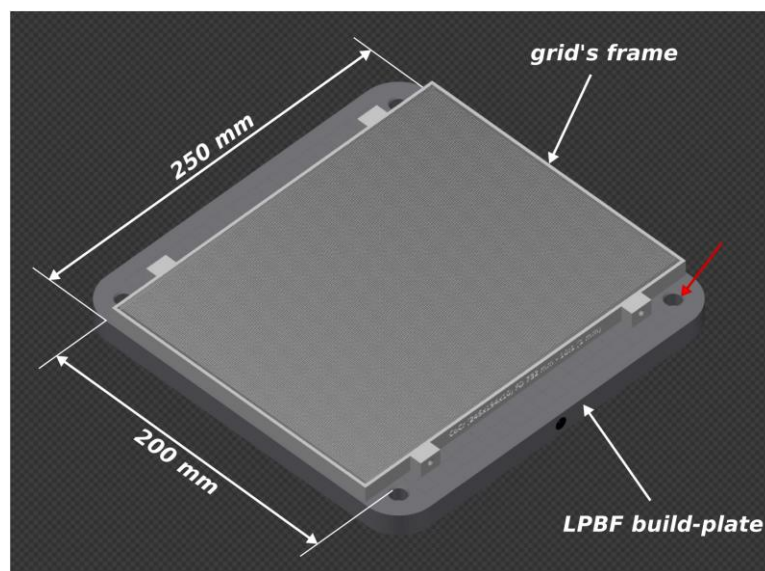


Fig 4-2. QuantAM 3D printing interface preview of grid placement in the (250x250 mm) build-plate. Red arrow shows build-plate securing clearance holes, which limited grid size in one dimension.

4.2.2 2D-ASG manufacturing

The parameters used to design our large-area grid are defined in Table 4-1. Additionally, the 2D-ASG had a grid-ratio of 10:1, a pitch of 0.909 lp/mm, and a rectangular array of 219 by 172 square elements. Grid-ratio is defined as the ratio of the height of the grid septa to the distance between them. The 2D-ASG was manufactured using a commercially available LPBF 3D printer (AM-400; Renishaw plc, New Mills Wotton-0-under-Edge, UK) in 277 layers, each 40 μm in thickness, using cobalt-chrome, metal-alloy powder (60 – 65 % Co, 25 – 35 % Cr, and 3-7 % Mo) 15-45 μm in diameter. The cobalt-chrome alloy was used due to its widespread usage in the LPBF industry and sufficiently high x-ray attenuation at relatively low energies (*i.e.*, 30 cm^{-1} at 42.4 keV).⁵³⁻
⁵⁵ Although tungsten has been commonly reported as the material of choice for 2D-ASG manufacturing,^{33,35,38} our goal was to evaluate the performance of a large-area 2D-ASG prototype using a readily available alloy. In the additive-manufacturing facility at our institution (ADEISS), cobalt-chrome is routinely used for the production of customized medical parts. Furthermore, due to the high melting point and high thermal conductivity of tungsten, the LPBF process for that material requires higher energy output,^{53,56} which

makes tungsten 2D-ASGs less accessible and more expensive.⁴⁵ Finally, our cobalt-chrome 2D-ASG was designed to only be used for clinical cases where energies up to 80 kVp are used (e.g., for peripheral cone-beam CT scanning) we do not anticipate cobalt-chrome to perform better than other metals (e.g., tungsten or lead) when higher energies are required.

Prior to building the full-size 2D-ASG, several smaller prototypes were manufactured to optimize the LPBF printing parameters. Thin septa were achieved using a “single-path” strategy (Fig 4-3B) where the ytterbium-fibre laser, operating at 100W, employed a longer-than-usual (60 μ s) dwell time and traversed each cell septa a minimum number of passes to achieve the desired thickness. Despite using a 70 μ m diameter laser focal spot size, this scanning strategy produced nominal 100 μ m walls due to expansion of the melting pool and the adhesion of surrounding powder, the latter of which is the main cause of surface roughness in LPBF.⁵⁷ To maintain the desired septal thickness and still ensure structurally stable septa, the distance between two consecutive points when the laser was on was set to 60 μ m. The laser scanning pattern across the grid frame was determined automatically by QuantAM software. The pattern had a radial configuration starting at the top-left corner of the grid frame (Fig 4-3A).

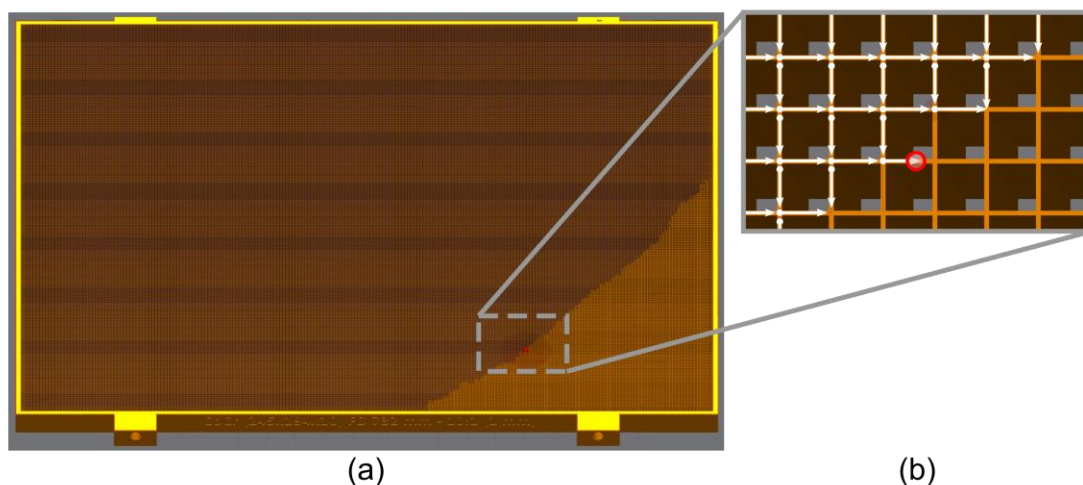


Fig 4-3. QuantAM laser scanning strategy preview for the top layer of the large-area, focused, 2D-ASG. (a) Laser scanning pattern starting at the top-left corner of the grid's frame. (b) Close-up of grid septa being consolidated with a single laser path, white arrows show the progression of laser position across the grid.

Rapid, repeated, heating and cooling cycles, which are characteristic of LPBF, are responsible for high residual stress build-up in the 3D printed part.^{49,58} The laser scanning pattern and the inherent heat-dissipating nature of the grid geometry helped minimize thermal stress during printing. After LPBF was completed, the operator removed the non-consolidated powder, and the grid was heat-treated in an argon-atmosphere oven to relieve any residual stresses. The oven set temperatures, 450 and 750 °C, were ramped up gradually over 60 minutes. Each temperature was maintained for 45 minutes with no cooling time between cycles. The oven temperature was reduced gradually at the end of the cycle allowing the part to cool-down naturally.

Wired electrical discharge machining (wire-EDM) was used to carefully detach the large area, focused, 2D-ASG from the build-plate. The designed grid-ratio of 10:1 was maintained thanks to the included 1 mm build-plate clearance (Table 4-1). The 2D-ASG exhibited strength and stability without additional inter-septal supports, and sustained no damage during regular manipulation.

4.2.3 Verification of grid septa dimensions

The 2D-ASG was inspected for dimensional accuracy and build quality using an image-based technique employing a measuring microscope (STM6, Olympus). The grid was placed on the bed of the measuring microscope and oriented perpendicular to the microscope image plane by maximizing observed pixel intensity. This was repeated over five different locations – center and peripheral edges – across the face of the 2D-ASG. The grid septa were oriented orthogonal to the image matrix of the microscope to facilitate pixel counting. Regions of interest (ROI) circumscribing the septal wall and a small region outside the wall, and excluding the septal intersections were selected and cropped. Each ROI was thresholded at the full-width-half-max (FWHM) of the intensity values to create binary images. The number of pixels across each line of the binary images, perpendicular to the septal wall, were counted and mean and standard deviation values were calculated. This technique ensures that the width of the septal wall is accurately and precisely assessed over its entire length and in all sections of the grid unit.

4.2.4 CBCT experimental setup

Cone-beam systems have, generally speaking, two different architectures. Stationary-object systems require the x-ray source and detector to be mounted on a gantry that is rotated around the object. With a stationary-source system, the object rotates in the path of the x-ray beam – often employed for small, bench-top systems. Our stationary-source design (Fig 4-4) consisted of a ceiling-mounted x-ray source (Proteus XR/a, GE Medical Systems) placed 732 mm away from a commercially available 383.5 by 459.5 by 14.7 mm, flat-panel detector with 139 μm element pitch (DRX 3543, Carestream Health). A computer-controlled, precision stage (Model PSR300, Intellidrives) was used to obtain 215 projections at one-degree angular increments for each Parker-weighted CBCT reconstruction in this study. Alignment of the detector was achieved by minimizing the width of the shadows cast by the septa of the grid on the detector. When the detector was properly aligned, the width of the septa shadows appeared both minimized and uniform across the face of the 2D-ASG.

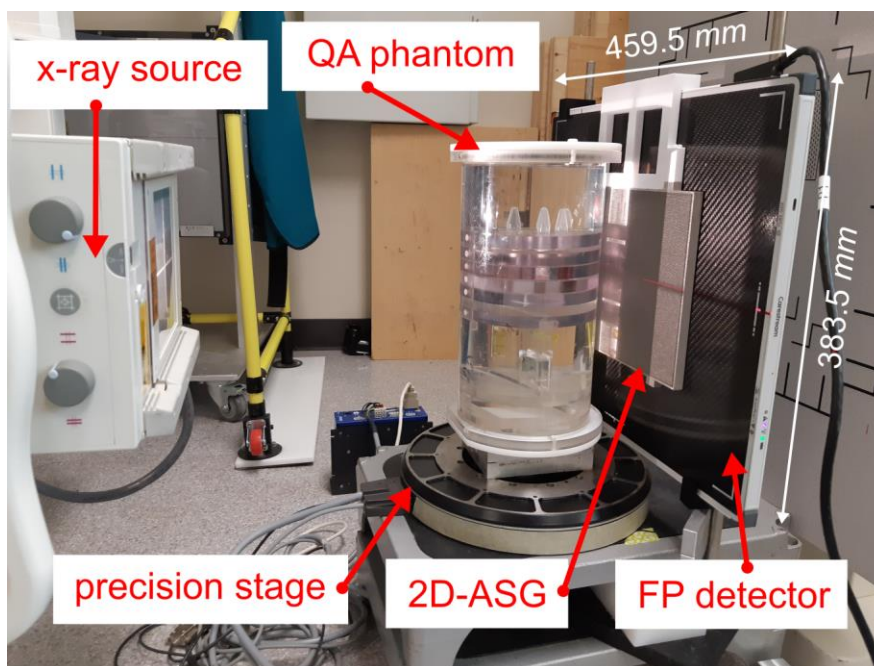


Fig 4-4. Custom, stationary-source, CBCT experimental setup. Ceiling-mounted x-ray unit, precision rotary stage, 2D-ASG, and flat-panel digital detector.

CT data of a water-filled, quality assurance phantom (Fig 4-5) was acquired, with and without the grid, at 80 kVp and 0.5 mAs to evaluate the performance of the 2D-ASG. No

other scatter-rejecting techniques were implemented in order to assess the effects of 2D-ASG alone. The 2D-ASG was placed directly in front of the detector using a custom 3D-printed clip, and primary transmission was evaluated using a primary transmission map,²⁴ $T(x, y)$, using:

$$T(x, y) = \frac{I_{grid}}{I_{no-grid}} \times 100 \quad (4.1)$$

In order to evaluate the geometric stability of the CBCT system, high-contrast, radio-opaque, 1 mm beads were attached to the QA phantom and a CT data set was acquired. As the phantom was rotated, the beads were expected to trace a sinusoidal path allowing the detection of geometric deviations. The mean deviation of beads from a best-fit sinusoid for each projection image was used to correct the phantom data prior to CBCT reconstruction.⁵⁹

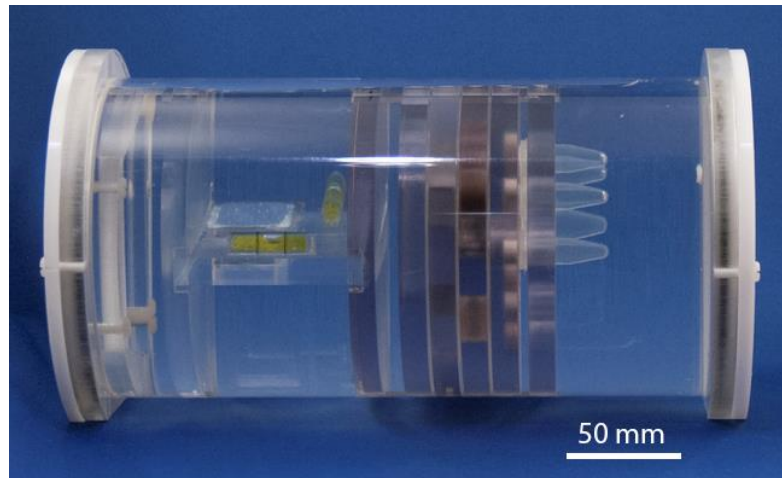


Fig 4-5. (305x154 mm) modular QA phantom used to evaluate CBCT image quality characteristics. The different sections and plates are arranged from left-to-right in the image.

4.2.5 2D low-contrast visualization

In plain 2D-projections, scatter significantly reduces low-contrast object visualization.^{11,24} We evaluated the effectiveness of the 2D-ASG to mitigate the reduction in contrast-to-noise ratio by acquiring 2D-projection radiographs of a plastic, 3D-printed, low-contrast phantom (Fig 4-6). The phantom was radiographed with and without the

2D-ASG and in the presence of a 15 cm water bath acting as a scatter source. The low-contrast phantom consisted of twenty-five cylindrical holes of various diameters and depths. Contrast-to-noise was calculated using the following.

$$CNR = \frac{|C - B|}{\sqrt{\sigma_C^2 + \sigma_B^2}} \quad (4.2)$$

Where C is the signal value of the low-contrast object and B the signal value of the object background, σ_C^2 and σ_B^2 are their respective variances.

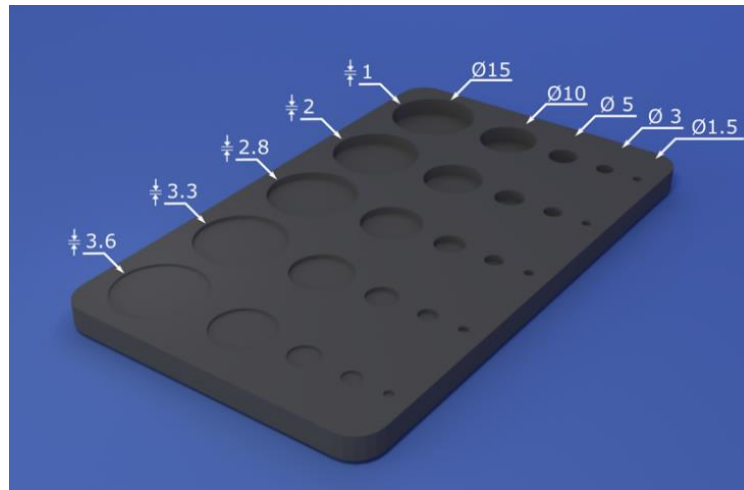


Fig 4-6. 3D rendering of the design of the 2D, 3D-printed, low-contrast phantom.

4.2.6 Grid-line artifact corrections and CBCT reconstruction

A limitation of the application of anti-scatter grids in digital radiography is the reduced x-ray fluence at detector elements obscured by grid septa. This reduced fluence results in a reduced detected signal creating grid-line artifacts (GLA) in the image.^{27,33} In theory, if the area of the element obscured by the grid-septa is small, then flat-field corrections should be able to reduce or remove these artifacts from the image. Conversely, if the area of the element covered by the grid is too large, this correction is unfeasible due to the low signal-to-noise ratio. For two-dimensional grids, this phenomenon can be further exacerbated in areas where the grid septa intersect. In our implementation, the detector elements were 139 by 139 μm , and the nominal grid-septa thickness was 100 μm . It is

important to note that the detected signal intensity did not drop below 30% of the incident x-ray fluence in any of the detector elements; this is to be expected because the nominal septal thickness was designed to be less than the detector element size. Below, we describe a two-step method for GLA correction using a modified, exposure-dependent, flat-field correction⁴⁸ and a customized spatial frequency Fourier filter.

Flat-field correction is regularly used to account for pixel-to-pixel variations (*i.e.*, fixed-pattern noise) in digital x-ray detectors. This strategy is able to successfully correct intensity variations for pixels unaffected by grid septa. However, it is ineffective for pixels that are partially obscured by grid septa due to exposure-dependent gain variations in these affected pixels. We have briefly described the necessity to characterize exposure-dependent, pixel-to-pixel, gain variations by performing flat-field corrections at various exposure levels.⁶⁰ This correction was achieved using an adapted approach from Altunbas *et al.*⁴⁸ where we used six exposure levels (E) – achieved using copper filtration of the x-ray beam (0, 0.5, 1, 1.5, 2, and 2.5 mm thicknesses) to generate exposure-dependent (E) gain correction map, $G(x, y, E)$, for each exposure level that was calculated using the following:

$$G(x, y, E) = \frac{I_{no-grid}^f(x, y, E)}{I_{grid}^f(x, y, E)} \quad (4.3)$$

where $I_{no-grid}^f(x, y, E)$ is the intensity value measured in analog to digital units (ADUs) of a flat-field image with no-ASG, and $I_{grid}^f(x, y, E)$ is the measured flat-field corrected pixel ADU with ASG. Data was organized using a multidimensional array (3072 x 2560 x 6), and pixel specific gain-factors were analyzed. Fig 4-7, shows the exposure dependent variations in gain-factors for a sub-set of pixels: representing pixels unaffected by grid-artifacts, affected by grid-septa, and affected by grid intersections.

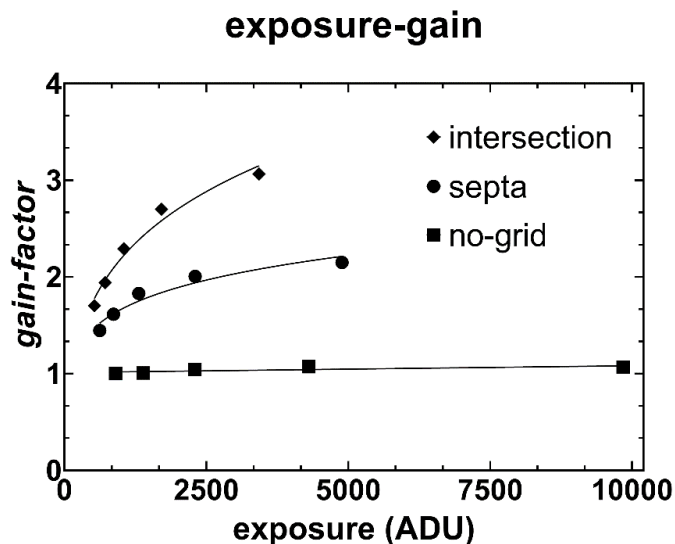


Fig 4-7. Exposure dependent gain-factor variations for three, example, detector elements illustrating the effect of varying the degree of grid septa shadow. Septa represents low shadow and septal intersection a greater degree of shadow. Power series curve-fits are shown in solid lines.

Gain-factors for pixels unaffected by grid-artifacts remained at unity (*i.e.*, standard deviations < 0.05), whereas pixels affected by grid-artifacts were well described by a power function, $G(ADU) = a \times ADU^b + c$. For such cases, curve coefficients (a , b , and c) were calculated (MATLAB, The MathWorks, Natick) and stored in a lookup table to reduce the computational burden of the correction. Projection images were corrected using this pixel-specific, exposure-dependent, gain correction.

In spite of the careful characterization of the gain response of detector elements obscured by the grid, faint grid-line artifacts remained visible in the projection data. However, the periodic nature of the grid-line artifacts allows implementation of a customized, fast-Fourier-transform (FFT), notch filter to further reduce grid-line artifacts.⁶¹ Only gridlines were affected by the FFT filter because no other structures presented the same spatial frequency in the projection image data. Fig 4-8A shows the Fourier power spectrum of an open image with the grid in place. A binary-mask was created using a combination of thresholding and manual segmentation of the power-spectrum. This binary-mask shown

in Fig 4-8B was used to remove the selected frequencies of each projection image in frequency space.

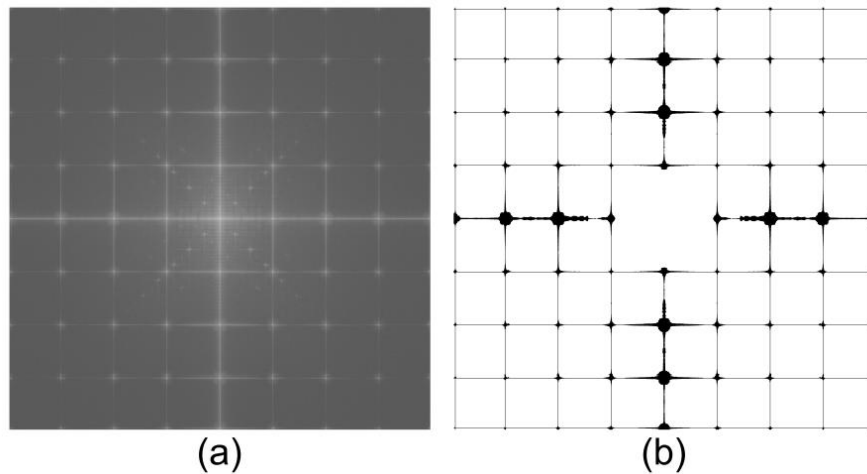


Fig 4-8. FFT images of an open acquisition with the 2D anti-scatter grid in place. (a) FFT power-spectrum. (b) thresholded and manually segmented binary-mask of FFT notch filter use to remove grid-line artifacts from projection images in frequency space.

The two sets of two-hundred and fifteen (215) projection images for each volume, with and without the 2D-ASG respectively, were used to reconstruct CBCT volumes using a Parker-weighted FDK algorithm. The full-resolution volumes ($119 \times 119 \times 119 \mu\text{m}$) were spatially averaged to $357 \times 357 \times 595 \mu\text{m}$, which is a clinically relevant voxel size,⁶² to improve the signal-to-noise characteristics of the data.

4.2.7 CBCT data analysis

Quality assurance (QA) phantoms are an effective tool to accurately and precisely evaluate the performance of clinical CT systems qualitatively and quantitatively.^{63,64} The phantom used in this study consisted of eight separated modular sections designed to assess the following aspects of CBCT image quality: spatial resolution, geometric accuracy, uniformity, noise, artifact characterization, contrast-to-noise ratio, and linearity. Fig 4-9 includes the technical details of the QA phantom.

Spatial resolution and geometric accuracy, evaluated by sections 1, 2, 4 and 5 of the QA phantom, were used to determine overall image quality differences between the two CBCT reconstructions – with and without 2D-ASG. Spatial resolution was qualitatively assessed by calculating the modulation transfer function (MTF) using the two, slanted edges located in sections 1 and 4.⁶³ Qualitatively, spatial resolution was also evaluated using the nine bar patterns (0.4 to 2.0 lp.mm⁻¹) of section 5. Geometric accuracy of the system was measured using the embedded array of five 0.8 mm diameter steel beads (section 2). Beads were arranged in a rectangular, 40 x 40 mm², pattern with one bead located exactly at the centroid.

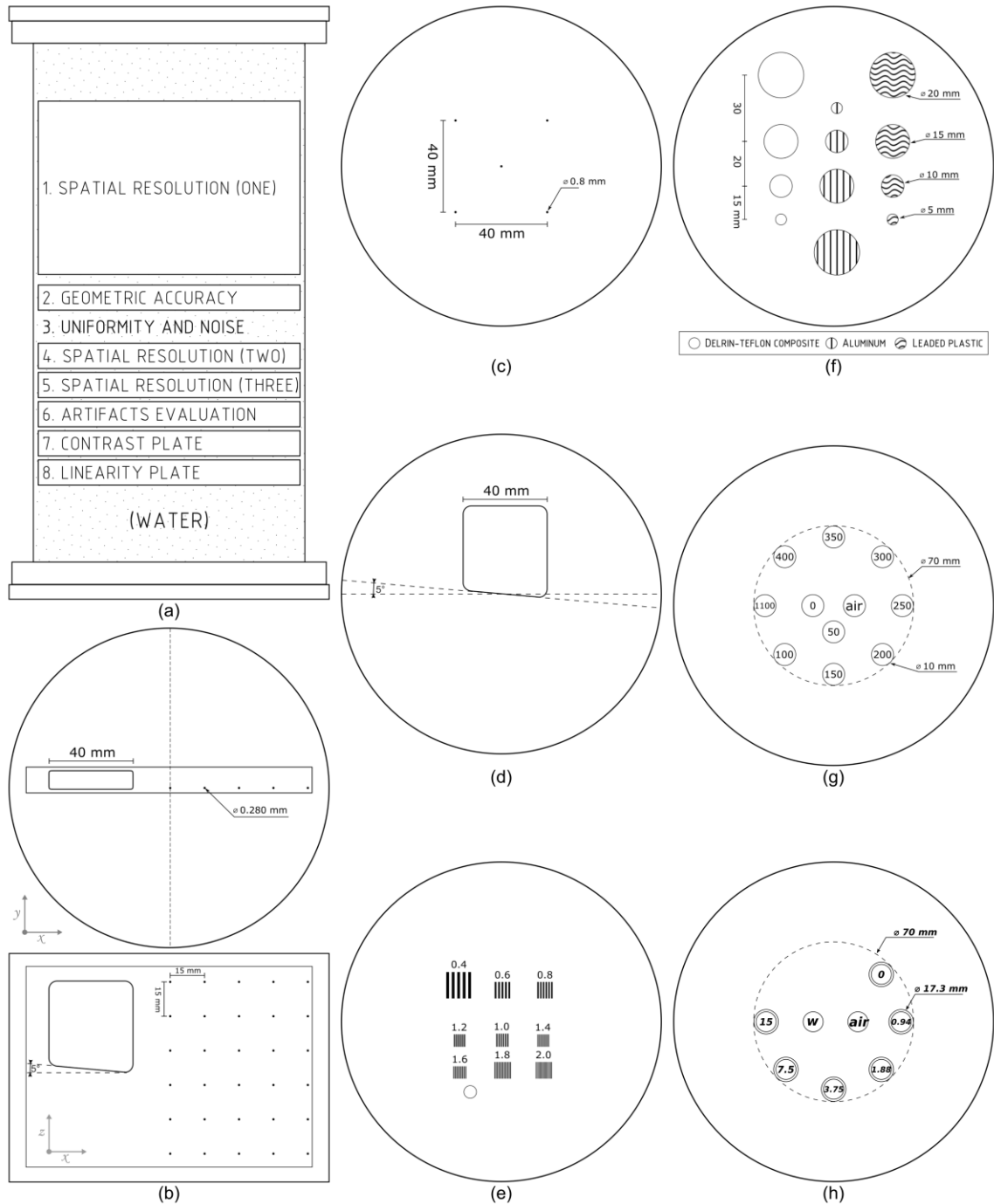


Fig 4-9. Technical details of the modular QA phantom. (a) Modules organization. (b) Spatial resolution section comprised of a (5x6) tungsten-carbide beads array, and a (x-z) slanted-edge. (c) Geometric accuracy plate with five steel beads designed to verify voxel-spacing in the reconstructed images. (d) Spatial resolution plate comprised of a (x-y) slanted-edge. (e) Spatial resolution plate used for qualitative

evaluation using bar-patterns with different pitches, values are expressed in $\text{lp}\times\text{mm}^{-1}$. (f) Artifacts characterization plate designed to investigate artifacts that may be encountered near large dense objects (*i.e.*, trabecular bone or metal implants). (g) Contrast plate comprised of bone-mimicking inserts (CIRS, Norfolk, VA and SB3TM Gamex RMI, Middleton, WI), values are expressed in $\text{mg}\times\text{cm}^{-3}$ of bone mineral density. (h) Linearity plate with iodine filled vials (Omnipaque, Sanofi Winthrop, New York, NY) at different concentrations, values in $\text{mg}\times\text{ml}^{-1}$.

Other sections of the phantom (3, 6, 7, and 8) were used to quantify improvements in image quality related to scatter rejection. The linearity plate of the QA phantom (Fig 4-9H), which consists of 1.73 by 3.93 cm vials filled with various concentrations of iodine (15, 7.5, 3.75, 1.875, 0.9375, and 0 $\text{mg}\cdot\text{ml}^{-1}$), was used to evaluate improvements in low-contrast visualization. CNR was calculated for each concentration of iodine using the same methodology described in the 2D low-contrast visualization section of this manuscript.

Shading artifacts (*i.e.*, cupping and streaking) were evaluated using the water-filled uniformity and artifact characterization sections (Fig 4-9F) of the phantom, respectively. Cupping was quantitatively measured using the Uniformity Index (UI) within cylindrical regions of interest (ROI) in section 3 near the central reconstruction slice:

$$UI = \frac{I_{periphery} - I_{center}}{I_{center}} \quad (4.4)$$

where $I_{periphery}$ and I_{center} are the mean intensities of ROIs located correspondingly. Qualitatively, cupping was visualized using radial signal profiles across the diameter of the uniformity section of the phantom. Finally, qualitative improvements in streak-artifact intensity were assessed by using the leaded-plastic inserts located in section 6 (Fig 4-9F).

4.3 Results

4.3.1 Parametric modelling

Fig 4-10A shows the Python-based node-tree interface. The interface included a preview of the CAD design that updated every time a parameter was modified. The design of the

2D-ASG CAD file took less than 6 minutes following input of all the parameters. Fig 4-10B, shows a closeup of the optimized STL geometry of one grid channel.

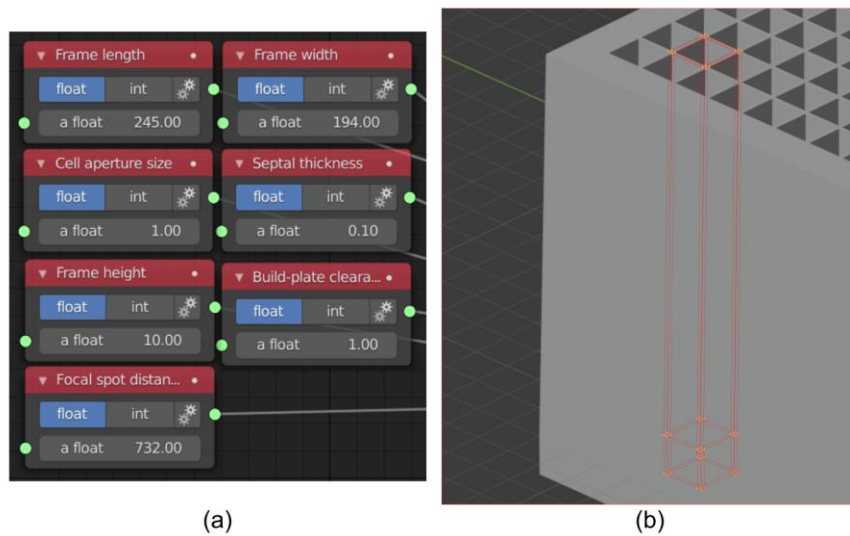


Fig 4-10. Blender 2D-ASG parametric modelling module. (a) Node-tree interface with various user definable 2D-ASG parameters. (b) CAD model preview and drawing of the optimized geometry of one grid channel.

4.3.2 2D-ASG post-manufacturing evaluation

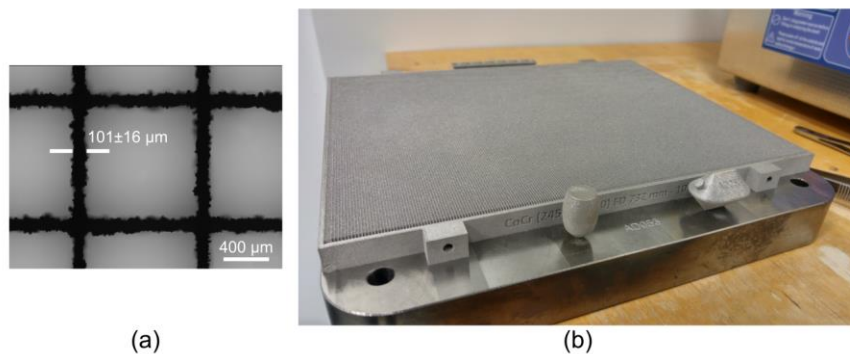


Fig 4-11. Large-area, focused, 2D-ASG after manufacturing and post-processing. (a) closeup of grid septa using the measuring microscope (nominal septal width was $101 \mu\text{m}$). (b) picture of the 2D-ASG after heat treatment still attached to the LBPf build-plate.

Images of the 245 x 194 x 10 mm 2D-ASG after heat-treatment and before wire-EDM are shown in Fig 4-11, demonstrating mechanical stability and appropriate grid septa

thickness ($101 \pm 16 \mu\text{m}$). After wire-EDM, consistent grid height allowed the 2D-ASG to lay flat against the x-ray detector, which made grid-detector coupling straightforward to achieve. Mechanical stability facilitated routine handling of the device as well as consistent grid shadows across the detector. Fig 4-12, shows closeup gain maps in different regions of the detector.

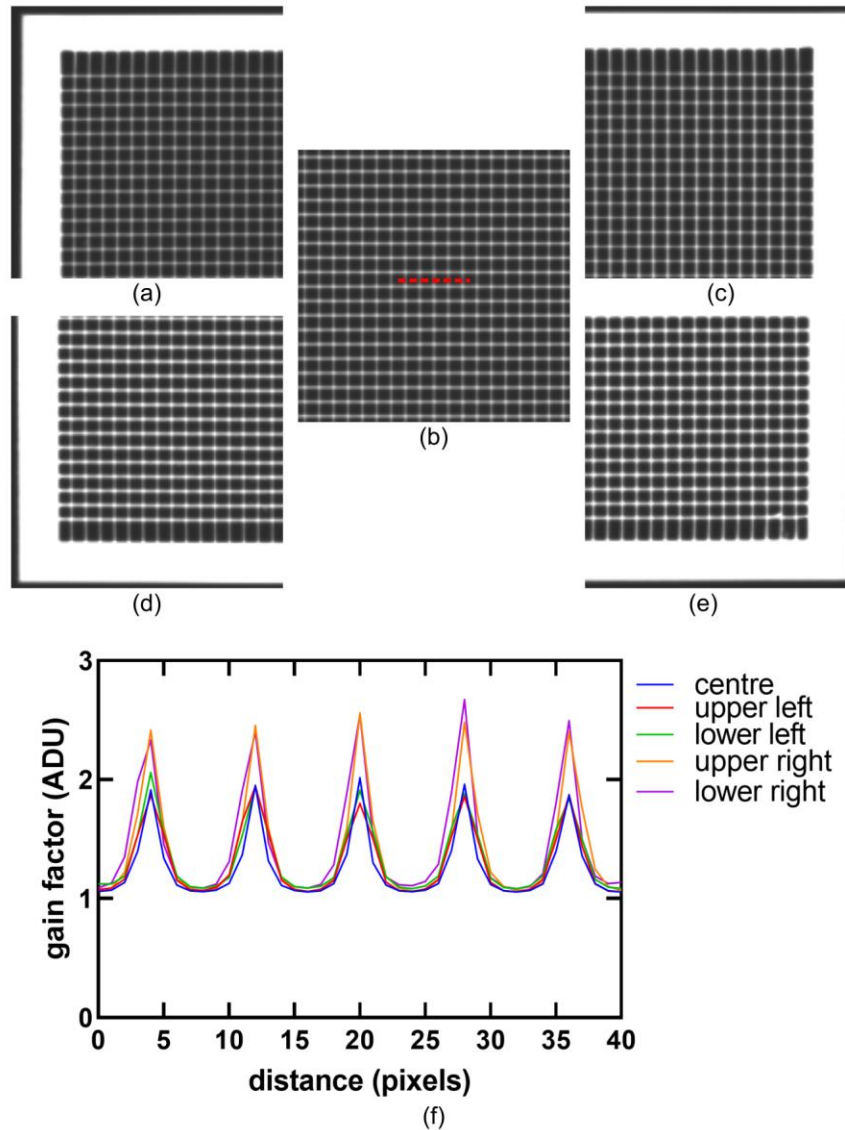


Fig 4-12. Grid-septa shadow consistency across the 2D-ASG (a-e) close-up images of gain maps at various regions of the grid upper left, center, upper right, lower left, and lower right, respectively. (f) line profiles across five grid-septa at each location showing consistency of grid-septa shadow thickness. The line profiles, for each

region, were placed approximately in the same relative location marked by the red-dotted line in (b).

An average transmission of 78% was achieved, which is consistent with the nominal 101 μm , septa (Fig 4-11A). Since each 139 x 139 μm detector element might be covered by varying amounts of 2D-ASG septa, primary transmission is better depicted using a cumulative histogram of the transmission map (Fig 4-13). Detector elements located underneath grid-septa intersections received the lowest amount of primary transmission, ~30 %, while elements located in open grid-channels received the largest amount of transmission, ~97%.

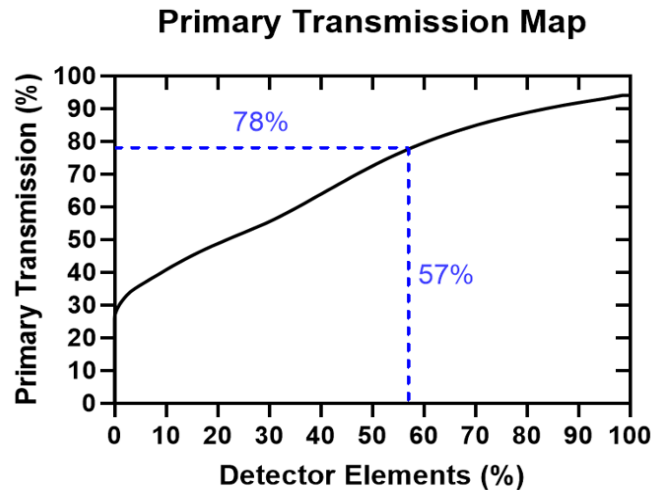


Fig 4-13. Cumulative histogram of the transmission map for a flood-field image of the large-area, focused, 2D-ASG.

4.3.3 2D low-contrast visualization

Low-contrast object conspicuity (*i.e.*, improved detection of small, low-contrast objects) is improved by a decrease in image noise. Fig 4-14A,B shows a side-by-side comparison of the 3D-printed, low-contrast phantom imaged without and with the 2D-ASG as described previously. CNR values, as a function of phantom's hole diameter and thickness, were improved for all cases. Proportionally larger improvements were observed as the hole diameter decreased, Fig 4-14C,D.

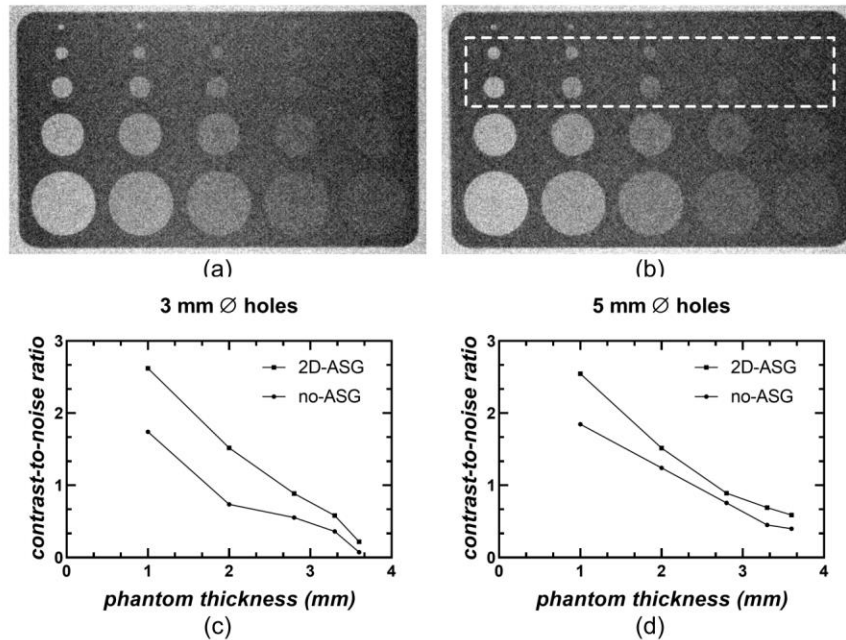


Fig 4-14. Low-contrast object conspicuity: 2D radiographs of the low-contrast phantom acquired with a 15 cm water bath and (a) without ASG, versus (b) with 2D-ASG. (c and d) show improvements in CNR across the 5 mm and 3 mm holes marked by the dotted box in (b). Images are shown using identical window and level settings.

4.3.4 Evaluation of grid-line artifact correction

4.3.4.1 In 2D projection images

Grid-lines appear as vertical and horizontal lines with reduced x-ray fluence in raw 2D-projections (Fig 4-15A). Conventional gain-correction tends to overcorrect grid-line artifacts because it does not take into account potential signal leaking from high-intensity neighbor detector elements. Fig 4-15B displays poorly corrected grid-line artifacts, where image intensity has been overcorrected. The proposed exposure-dependent gain correction strategy was able to reduce grid-line artifacts by $> 90\%$ in high x-ray fluence regions of the image, and $> 60\%$ in regions with low x-ray fluence (Fig 4-15C,D). The improved gain correction allowed satisfactory grid-line removal with the addition of a customized notch-FFT-filter.

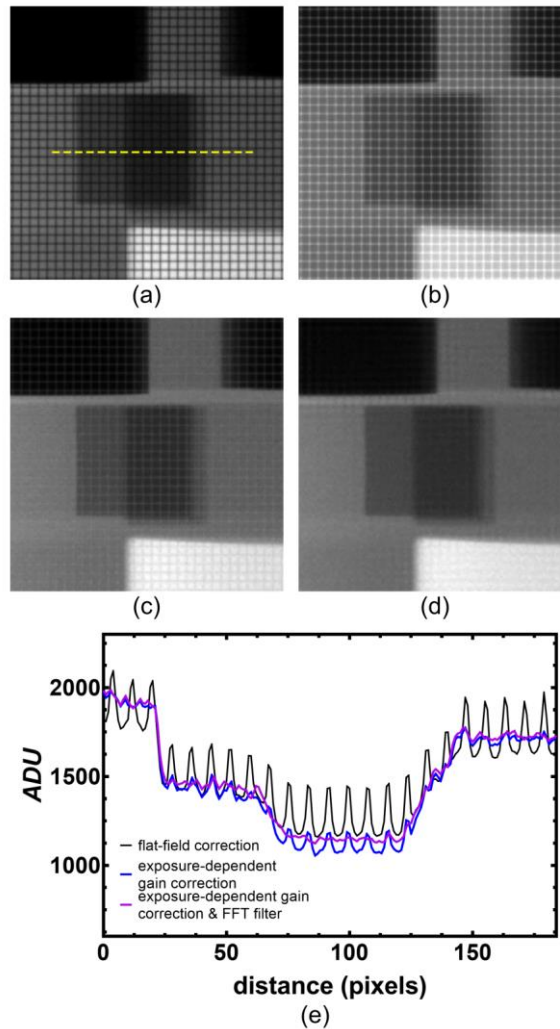


Fig 4-15. Close-up of QA phantom region in a CBCT 2D-projection image. (a) uncorrected, raw grid-line artifacts (b) with flat-field correction (c) with exposure-dependent gain correction, (d) with exposure-dependent gain correction and notch-FFT-filter and (e) line-profiles (across yellow-dotted line in (a)) showing the reduction of grid-line artifact intensity using the exposure-dependent correction method and further notch-FFT-filter.

4.3.4.2 In CBCT reconstructions

Traditional linear-gain correction produced severe ring-artifacts (*i.e.*, $s = 894.02$ HU) when compared to the exposure-dependent gain-correction (*i.e.*, $s = 85.55$ HU) for homogeneous regions of the QA phantom. Exposure-dependent gain-correction followed by Fourier-notch filtering improved the CT number precision by a further 31 HU.

Qualitative analysis of line-pairs showed appropriate maintenance of image spatial-resolution (Fig 4-16).

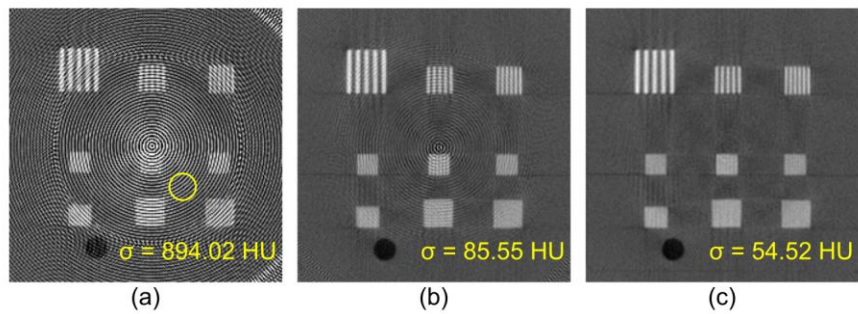


Fig 4-16. Resolution plate of QA phantom reconstructed (a) using linear-gain correction, (b) using exposure-dependent gain correction, and (c) after both exposure-dependent gain correction and Fourier-notch filtering. Standard deviations calculated in the outlined circular, yellow ROI show improvements in image quality using the proposed GLA correction method.

Improvements in CT number accuracy for homogeneous materials were observed by analyzing HU variations across an air-filled slanted edge chamber inside the QA phantom. Ring-artifacts caused by GLA were significantly minimized and residual rings were removed by Fourier filtering. Fig 4-17B,C, show low-HU variations, ~50 HU, after implementation of the proposed methods.

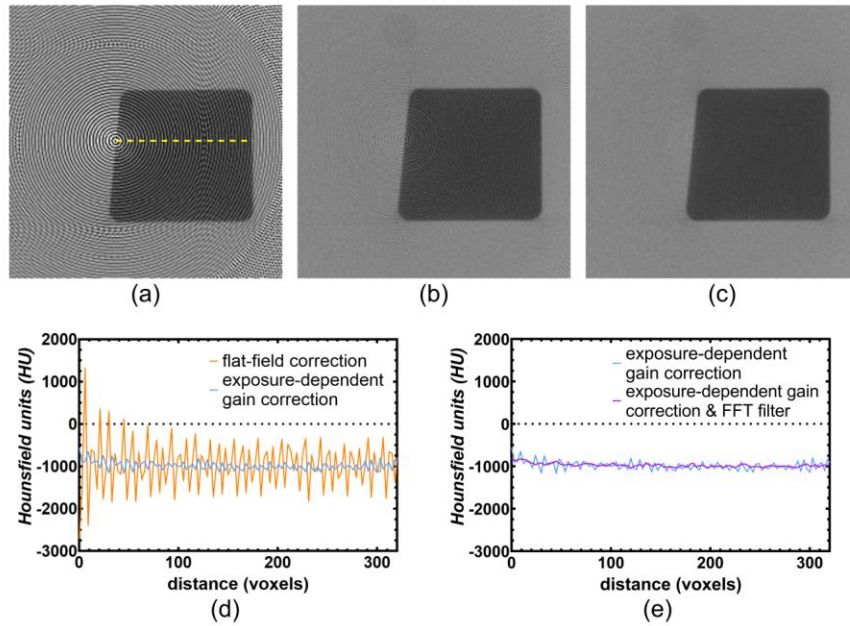


Fig 4-17. CT number accuracy improvements for air-filled, slanted-edge chamber inside the QA phantom. (a) reconstruction with traditional gain correction (b) with exposure-dependent gain correction, and (c) using Fourier filtering. (d, e) show line profiles, marked by the yellow dotted line in (a), across the air-filled structure.

4.3.5 CBCT image quality evaluation

4.3.5.1 Geometric accuracy and resolution

Fig 4-18 shows an image of the geometric accuracy plate reconstructed with the 2D-ASG in place. The distance between steel beads was 39.83 ± 0.06 mm compared to the expected 40 ± 0.025 mm, demonstrating excellent in-plane geometric accuracy. Likewise, the out-of-plane distance between tungsten-carbide beads of the first spatial resolution plate of the QA phantom was 14.98 ± 0.07 mm. The inter-bead distance was designed to be 15 mm.

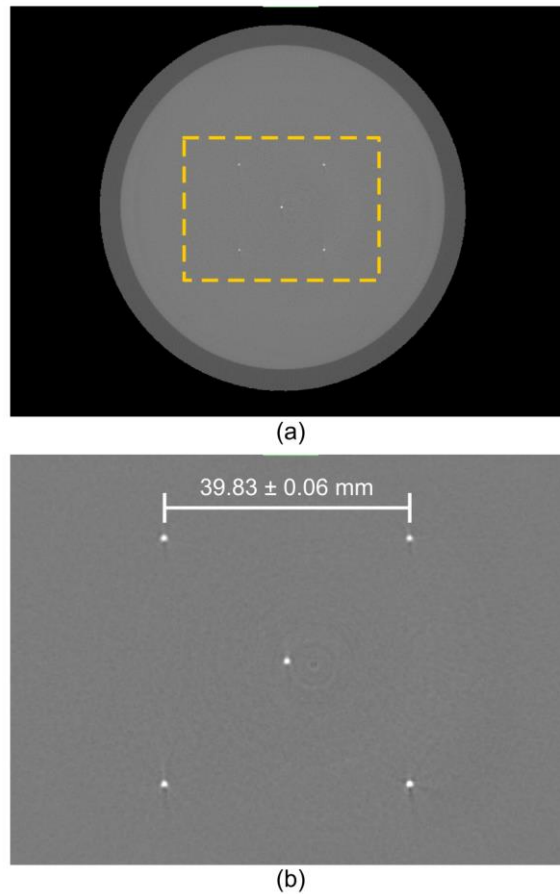


Fig 4-18. (a) CBCT slice of the geometric accuracy plate of the QA phantom, (b) closeup of the area in yellow-dotted lines in (a) showing the five steel beads in the axial plane and measured inter-bead distance.

Spatial resolution was evaluated qualitatively using the bar patterns included in one of the resolution plates of the QA phantom. Fig 4-20 shows the conservation of spatial resolution with and without the 2D-ASG. Bar patterns for 0.8 line pair/mm (lp/mm) were resolved in both experimental scenarios. These observations were quantitatively verified by the MTF curves calculated using the slanted-edge oriented in the x, y plane (Fig 4-19). An MTF of 0.1 corresponded to 0.9 lp/mm, which was in agreement with the resolution observed in the bar patterns array. The slight differences between the two MTF curves were attributed to FFT filtering effects in the 2D-ASG scenario.

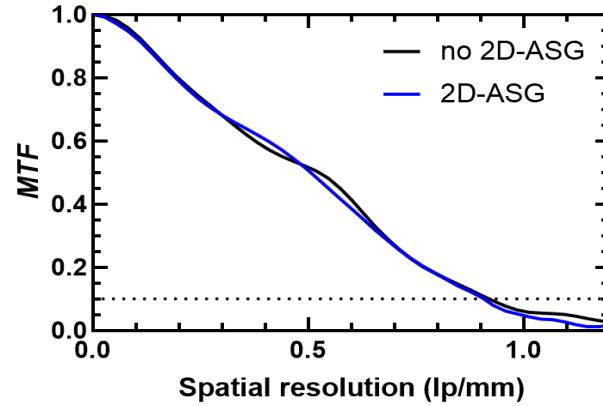


Fig 4-19. Modulation transfer function (MTF) of the CBCT reconstructions measured from the slanted-edge plate of the QA phantom.

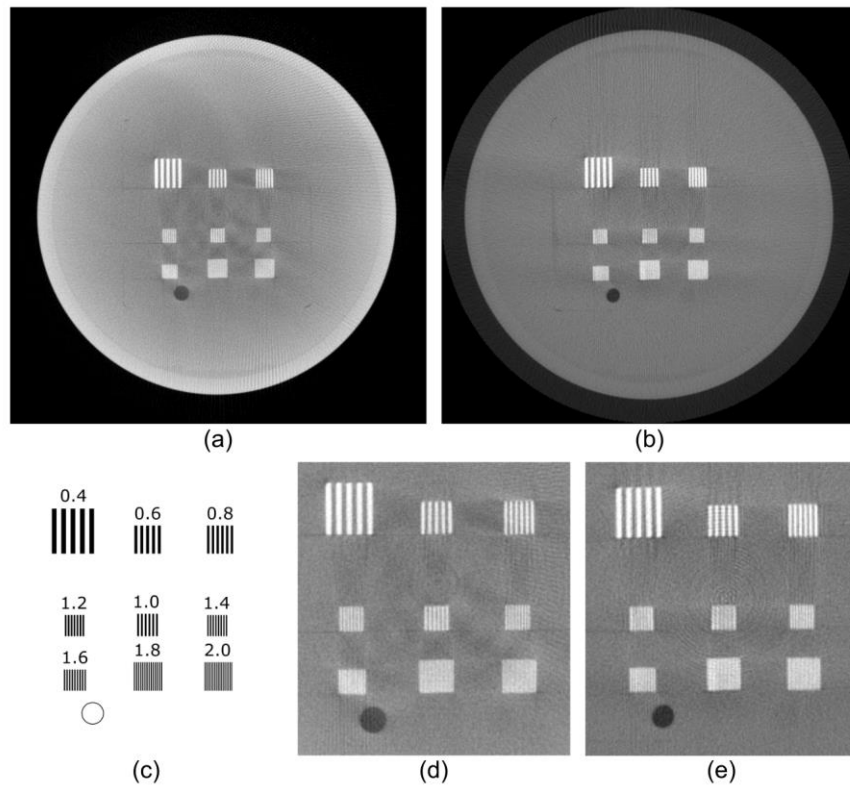


Fig 4-20. Qualitative evaluation of spatial resolution using the resolution plate of the QA phantom. (a) CBCT reconstruction without 2D-ASG. (b) CBCT reconstruction with 2D-ASG. (c) details of the resolution plate with interleaved Mylar and Aluminum sheets in lp/mm. (d, e) magnified images of (a) and (b) respectively.

4.3.5.2 Low-contrast and linearity

Table 4-2 lists the CNR values for bone-mimicking inserts of the contrast plate of the QA phantom in CBCT images with and without 2D-ASG. The arrangement of the inserts and the details of the plate are shown in Fig 4-21A. The 2D-ASG provided a 10.32% to 60.34% improvement in CNR compared to no 2D-ASG, with a 17.8% average of improvement across inserts. A substantial cupping artifact is visible in the volume acquired without 2D-ASG. This artifact is less conspicuous in the volume acquired with the 2D-ASG.

Table 4-2. Contrast plate CNR calculations with and without 2D-ASG.

Bone mineral density (mg.cm³)	CNR no 2D-ASG	CNR with 2D-ASG
1100	9.278	10.499
400	3.572	4.387
350	3.612	3.984
300	3.314	3.811
250	1.914	2.460
200	1.807	2.077
150	0.992	1.590
100	0.711	0.897
50	0.733	0.508
air	5.848	6.855

The second row of Fig 4-21 shows the calculated CT number (HU) as a function of the bone mineral density of the bone-mimicking inserts located in the contrast plate of the QA phantom. Both volumes presented a significant ($p < 0.0001$) linear correlation between signal intensity and increasing bone density. The differences in mean values and corresponding standard deviations for each insert illustrate the improvements in CNR between the two experimental scenarios.

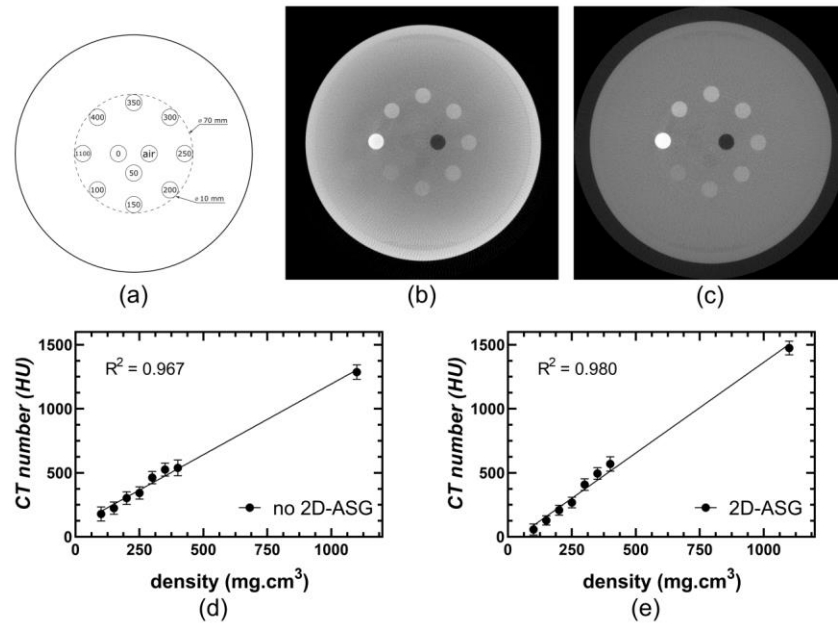


Fig 4-21. Evaluation of contrast and linearity using the contrast plate of the QA phantom. (a) details of the contrast plate showing BMD inserts at various densities. (b) CBCT reconstruction without 2D-ASG. (c) CBCT reconstruction with 2D-ASG. (d) Linearity plots for the reconstruction without the 2D-ASG (d), and with the 2D-ASG (e) (linearity plots represent HU as a function of bone mineral density).

4.3.5.3 Cupping

CBCT reconstructions of the resolution and uniformity plates of the QA phantom without and with the 2D-ASG are shown in Fig 4-22 and Fig 4-23. Without the 2D-ASG, HU values were overestimated and contributed to the lower homogeneity of the reconstructions when compared to the data where the 2D-ASG was employed. With the 2D-ASG, shading and cupping artifacts were reduced by 65% of the Uniformity Index (UI). Residual artifacts were attributed to residual scatter and beam hardening. Modelling the x-ray spectra at 80 kVp with the inherent 1 mm aluminum filtration of the x-ray unit rendered a mean energy of 38.8 keV. The addition of 154 mm of water provided additional filtration that increased the mean energy of the spectrum to 48.18 keV (Fig 4-24A). Fig 4-24B shows the decrease in transmission percent of photons at various energies across cobalt-chrome alloy and tungsten.

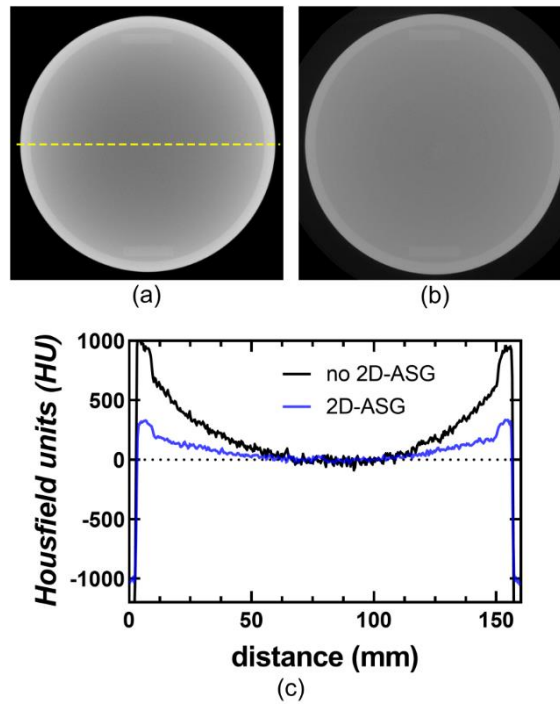


Fig 4-22. CT number accuracy evaluation using the uniformity plate of the QA phantom (a) CBCT reconstruction of the uniformity plate without 2D-ASG. (b) CBCT reconstruction of the uniformity plate with 2D-ASG. (c) HU profile along the dotted line in (a).

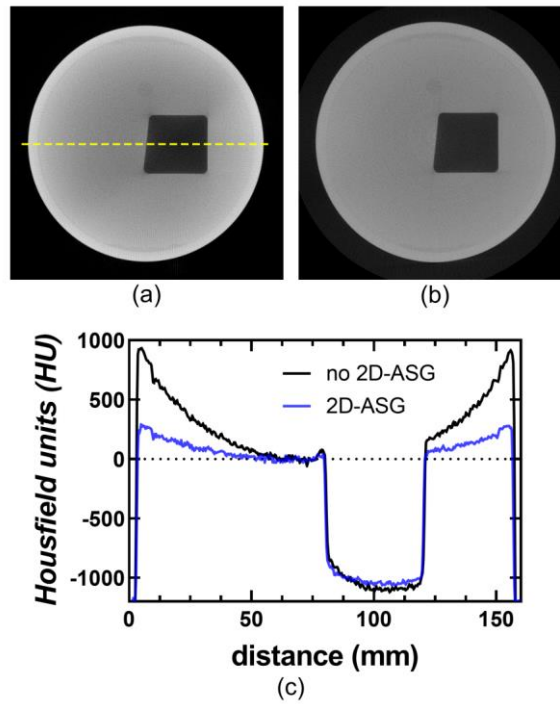
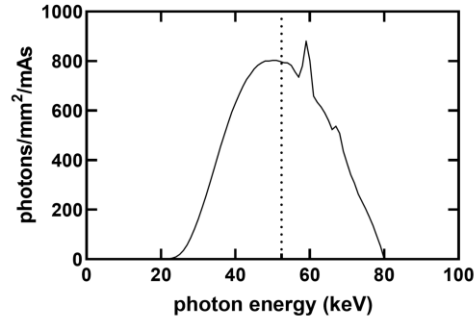


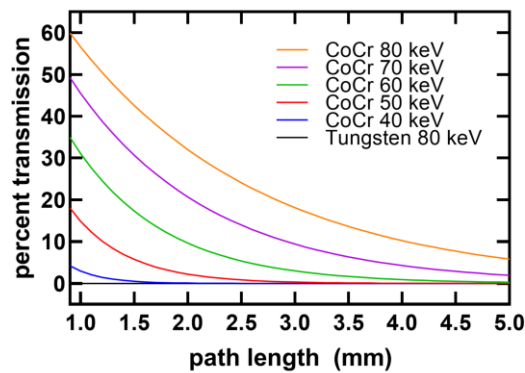
Fig 4-23. CT number accuracy evaluation using the slanted-edge, MTF, resolution plate of the QA phantom (a) CBCT reconstruction of the resolution plate without the 2D-ASG. (b) CBCT reconstruction of the resolution plate with the 2D-ASG. (c) shows a linear profile in HU across the phantom along the yellow dotted line in (a).

X-ray spectrum at 80 kVp with 154 mm water filtration



(a)

0.9 to 5 mm x-ray percent transmission



(b)

Fig 4-24. Experimental x-ray spectral characteristics and percent transmission through 2D-ASG septa. (a) characterization of the x-ray spectrum for CBCT data acquisition with an additional 154 mm of water filtration. (b) photon percent transmission through 0.9 to 5 mm of cobalt-chrome septal material.

4.4 Discussion

Small-area 2D-ASGs have been previously described as an effective means to prevent scatter-related image quality degradation in CBCT systems.^{24,35-37} However, the extension to covering a large-area of the x-ray detector is not straightforward due to design, fabrication, and implementation considerations.⁶⁵ 2D-ASGs have been previously manufactured in tungsten, due to its higher attenuation coefficient.^{24,35,36} However, our results show that large-area 2D-ASGs manufactured in cobalt-chromium alloy are able to significantly improve image quality for high-scatter scenarios at relatively-low diagnostic energies (*i.e.*, 80 kVp). For example, our cobalt-chromium 2D-ASG could then be an

effective solution for scatter reduction in peripheral cone-beam CT scanners such as the OnSight 3D Extremity System by Carestream Health.

The design of the large-area grid was achieved using an open-source software utility capable of modelling any grid geometry using a small set of user-defined parameters. This parametric approach addresses the shortcomings of traditional CAD systems, which cannot perform geometric-modelling operations on designs with more than 1000-2000 elements,⁵¹ and allows for the fast and efficient generation of system-specific, grid geometries. The capability to easily model 2D-ASGs with various geometries can be beneficial when running Monte-Carlo simulations or assessing the printability of the design. The flat-panel detector pitch, detector-to-source distance, and size of the 2D-ASG are the most critical aspects to consider. The geometry of the open channels in our parametric software utility has been modified and successfully adapted for other applications involving focused geometries (*e.g.*, gamma collimators).⁶⁶

During printing, the rapid heating and cooling cycles, characteristic of LPBF, can induce high thermal variations that promote residual stresses, warping, cracks, and even complete print failure due to de-lamination of the part from the build plate.^{49,58,67} These residual stresses compound as the part occupies a larger area of the build plate. To the best of our knowledge, the largest 2D-ASG prototypes described in the literature have not exceeded an area of 3 by 20 cm² of the build plate.^{24,33,35-37,65} Additionally, the assembling of multiple prototypes into a larger grid presents challenges such as alignment of the assembly and thicker septa at the interface. Our results show that fine tuning of the print parameters, combined with a cell-by-cell, single-path, scanning strategy, greatly facilitated the fabrication of the large-area 2D-ASGs in cobalt-chrome alloy. We believe that the success of the print was significantly aided by the heat-dissipating nature of the 2D-ASG geometry. The geometry of the grid acted in a similar way to the role of sacrificial supports in LPBF. Sacrificial supports are lattice-based structures used to raise the part from the build plate to dissipate thermal stresses and to facilitate part detachment from the build plate.⁶⁸ In the case of 2D-ASGs, the print may fail if the cell size is too large and, therefore, the distance between intersections, or contact points, does not provide enough septal support during fabrication. This is particularly important at the

corners of the 2D-ASG where grid septa are most tilted. It is worth mentioning that stress-relieving through heat treatment is mandatory to prevent uplifting or deflection of the part after detachment from the build plate.^{46,49} Furthermore, the build plate needs to be preheated in order to minimize these effects. The detachment of the part from the build plate must be done carefully and with high accuracy to maintain proper septal alignment relative to the detector face. Access to specialized machining (*e.g.*, wire electrical discharge machining) should be considered.

It is desirable to print grid septa as thin as possible because it reduces the effects of GLA and maximizes the primary transmission of the grid. Grid septal thickness is determined by laser energy, scanning strategy, powder particle size, and laser spot size. Our parameters included a spot size that was 2-5 bigger than powder particles. Similar to other researchers, our nominal thickness limit was around 100 μm . Grid septa thickness could theoretically be reduced with powders that have smaller particle size and LPBF machines with smaller focal spot. Although our results showed that a single path strategy was effective at producing structurally stable septa, this may not be the case for other metals or alloys. Xie, *et al.*⁶⁹ have shown that a double-path strategy improves both wall thickness and density for similar objects printed using tungsten. Our design matched the primary transmission characteristics of other prototypes in the literature, however, the pitch of our 2D-ASG made GLA correction challenging. Increasing both grid pitch and ratio may be an effective alternative for design optimization.

The choice of a 2D-ASG material with as high an electron density as possible will maximize the scatter rejection efficiency of the grid. However, consideration of material properties such as strength, rigidity, brittleness, and thermal conductivity, as well as cost and toxicity should be taken into account. At the time of these experiments, the LPBF printers that were capable of printing a grid this large and were available at our additive manufacturing facility could routinely print only in titanium and cobalt-chrome alloys. In our facilities, the extension to printing in other denser metals, such as tungsten, is not trivial for a variety of practical reasons, including cross contamination of various metal powders, and contraventions of ISO certifications. Nevertheless, in the future, we could certainly reproduce our work in tungsten for applications where only tungsten will

suffice. In which case, it will be necessary to refine printing parameters such as exposure time, laser energy, and scanning strategy.

In our cobalt-chrome design, all photons with an angle of incidence less than 84.28° degrees will begin to be filtered by the grid septa based on the calculation $Tan(\phi) = \text{grid-height}/\text{cell-width}$. Photons at the mean energy of our spectrum travelling through a 154 mm water filled phantom (52.4 keV) are 50% filtered by a minimum of 0.914 mm of path length through the cobalt-chrome septa with an angle of incidence of 83.7° degrees. However, photons at the peak energy of our spectrum (80 keV) are only 40% filtered at the same angle of incidence. Fig 4-24B shows the percent transmission for 80, 70, 60, 50, and 40 keV photons through various path-lengths in cobalt-chrome, and 80 keV through tungsten, as well as the modelled spectrum for our experiments. The inability of our grid to completely remove scattered photons over 52.4 keV was a limitation, however, our results suggest that scatter was sufficiently reduced to improve image quality. Future work includes the printing of similar sized 2D-ASG using tungsten and a smaller 2D-ASG on a different 3D printer with a smaller build plate (AM-125; Renishaw plc, New Mills Wotton-under-Edge, UK), on which tungsten has already been implemented.

Grid-line artifacts are a major concern when it comes to the implementation of 2D-ASG. If septal thickness is larger than the detector elements, fixed-pattern noise correction might not be feasible, leading to severe ring artifacts in the CBCT reconstruction. In our implementation, no detector element received less than 30% of primary signal. Furthermore, consistent grid structure was observed across the whole 2D-ASG. This demonstrates the accurate geometry of focused septa. Our combination of exposure-dependent gain correction and FFT notch filtering allowed for the effective correction of grid-line artifacts. We believe that the residual GLA after exposure-dependent gain correction were caused by a combination of residual scatter, temporal blurring due to ghosting, and non-linear veiling glare. Other groups have presented alternative methods to correct GLA, including total variation suppression and residual scatter characterization.^{33,37} Our results show that exposure dependent gain correction outperforms traditional flat-field corrections and might reduce the need for alternative methods in other 2D-ASG geometries, especially if the 2D-ASG has a larger pitch and

improved scatter rejection characteristics (*e.g.*, made of tungsten). Our GLA correction method will require testing for the case of clinical CBCT systems due to the effect of gantry flexure and potential grid misalignment as a function of angle. In this scenario, the location of the x-ray focal spot might change, impacting the accuracy of the gain maps. An angle-dependent calibration may be required to maintain optimal GLA correction. Although the FFT notch filter was able to remove GLA in the centre of the field-of-view, some artifacts were noticeable near the edges of the 2D-ASG frame. These artifacts were caused by Gibbs ringing and affected the periphery of the CBCT reconstruction. This could be a limitation in the case of volume stitching.

Similar to other studies,^{24,35-37} improvements in image quality using our 2D-ASG were particularly noticeable in CT number accuracy and low-contrast visualization, 65% and 48% improvement, respectively. Although our results do not match the level of improvement reported by these studies, we believe there are significant differences in our experimental setup that account for these discrepancies. First, it is possible that the residual cupping observed in our images could be caused by residual scatter not captured by our cobalt-chrome 2D-ASG. Secondly, our experiments covered a larger-area of the flat-panel detector, were conducted at lower energies (80 vs 125 kVp), and did not include additional filtration to ameliorate the effects of beam hardening. Finally, our volumes were reconstructed using a limited number of projection images (215° vs 360°). We plan to use iterative reconstruction methods in the future to reduce streak artifacts that are characteristic of Parker-weighted CBCT reconstructions.

4.5 Conclusion

We have successfully designed, manufactured, and implemented the first large-area, 2D-ASG for flat-panel CBCT. Traditional CAD design techniques for these complicated structures are unwieldy, inefficient, and do not lend themselves well to design revision. Our implementation of an open-source, parametric modelling approach significantly reduces the design time, computational burden, and greatly facilitates revisions and design changes.

We optimized the additive manufacturing process to successfully produce the required grid geometry ensuring mechanical stability, scatter rejection, and optimal primary transmission. These optimizations included considerations for the energy deposition within the melt-pool, as well as the implementation of a cell-by-cell single-path scanning strategy. Grid septa thickness and transmission characteristics of the 2D-ASG were rigorously evaluated using a metrology microscope and an automated script to average septa thickness with sub-pixel resolution.

Grid line artifacts (GLA) were corrected using both an exposure-dependent gain correction and a FFT notch filter. The relatively high pitch of our 2D-ASG compared to previously reported ASG prototypes exacerbated the GLA removal problem, which warrants further investigation using iterative methods or artificial intelligence (AI).

Significant improvements (65%) in CT number accuracy, as measured by the uniformity index, were observed when using the 2D-ASG, making these CBCT reconstructions more suitable for quantitative imaging tasks and for clinical scenarios that require accurate image segmentation. Significant CNR improvements were observed for low-contrast bone-mineral inserts. These improvements in CNR could be key when diagnosing low-contrast pathologies in clinical imaging. The use of a 2D anti-scatter grid also separates the effect of scatter from beam-hardening, making it potentially easier to correct remaining beam-hardening artifacts using established methods.⁷⁰

Future work includes the implementation of the 2D-ASG in a clinical CT system and at higher energies. In these systems, an angle-dependent gain correction may be required to reduce the effects of gantry flexure. Iterative or AI-based reconstruction techniques could also be used to improve GLA correction and the noise characteristics of our CBCT reconstructions. We anticipate that, at higher energies, 2D-ASGs manufactured in cobalt-chrome might not be as effective as those printed in other more attenuating metals, such as tungsten.

4.6 Acknowledgements

Support for this project came from the Canadian Institutes of Health Research (Foundation Grant FDN 148474) and the Ontario Research Fund (Research Excellence RE-077-66). D.W.H. is the Dr. Sandy Kirkley Chair in Musculoskeletal Research within the Schulich School of Medicine & Dentistry at Western University. S.F.C. is supported in part by a Transdisciplinary Bone & Joint Training Award from the Collaborative Training Program in Musculoskeletal Health Research at The University of Western Ontario. The authors would also like to thank Matt Parkes and Tom Chmiel at ADEISS for their assistance with the manufacturing of the 2D-ASG.

4.7 References

1. Jaffray D, Siewerdsen J. Cone-beam computed tomography with a flat-panel imager: initial performance characterization. *Medical physics*. 2000;27(6):1311-1323.
2. Jaffray DA, Siewerdsen JH, Wong JW, Martinez AA. Flat-panel cone-beam computed tomography for image-guided radiation therapy. *International Journal of Radiation Oncology* Biology* Physics*. 2002;53(5):1337-1349.
3. Fahrig R, Moreau M, Holdsworth D. Three-dimensional computed tomographic reconstruction using a C-arm mounted XRII: Correction of image intensifier distortion. *Medical physics*. 1997;24(7):1097-1106.
4. Manzke R, Grass M, Hawkes D. Artifact analysis and reconstruction improvement in helical cardiac cone beam CT. *IEEE transactions on medical imaging*. 2004;23(9):1150-1164.
5. Sonke JJ, Zijp L, Remeijer P, van Herk M. Respiratory correlated cone beam CT. *Medical physics*. 2005;32(4):1176-1186.
6. Nemtoi A, Czink C, Haba D, Gahleitner A. Cone beam CT: a current overview of devices. *Dentomaxillofacial Radiology*. 2013;42(8):20120443.
7. Yegya-Raman N, Kim S, Deek MP, et al. Daily Image Guidance with Cone Beam Computed Tomography May Reduce Radiation Pneumonitis in Unresectable Non-Small Cell Lung Cancer. *International Journal of Radiation Oncology* Biology* Physics*. 2018;101(5):1104-1112.
8. Lechuga L, Weidlich GA. Cone beam CT vs. fan beam CT: a comparison of image quality and dose delivered between two differing CT imaging modalities. *Cureus*. 2016;8(9).

9. Elstrøm UV, Muren LP, Petersen JB, Grau C. Evaluation of image quality for different kV cone-beam CT acquisition and reconstruction methods in the head and neck region. *Acta Oncologica*. 2011;50(6):908-917.
10. Zhu L, Xie Y, Wang J, Xing L. Scatter correction for cone-beam CT in radiation therapy. *Medical physics*. 2009;36(6Part1):2258-2268.
11. Nagarajappa AK, Dwivedi N, Tiwari R. Artifacts: The downturn of CBCT image. *Journal of International Society of Preventive & Community Dentistry*. 2015;5(6):440.
12. Siewerdsen JH, Jaffray DA. Cone-beam computed tomography with a flat-panel imager: Magnitude and effects of x-ray scatter. *Medical physics*. 2001;28(2):220-231.
13. Pauwels R, Araki K, Siewerdsen J, Thongvigitmanee SS. Technical aspects of dental CBCT: state of the art. *Dentomaxillofacial Radiology*. 2014;44(1):20140224.
14. Pauwels R, Jacobs R, Singer SR, Mupparapu M. CBCT-based bone quality assessment: are Hounsfield units applicable? *Dentomaxillofacial Radiology*. 2014;44(1):20140238.
15. Nackaerts O, Maes F, Yan H, Souza PC, Pauwels R, Jacobs R. Analysis of intensity variability in multislice and cone beam computed tomography. *Clinical oral implants research*. 2011;22(8):873-879.
16. Bhoosreddy AR, Sakhavalkar PU. Image deteriorating factors in cone beam computed tomography, their classification, and measures to reduce them: A pictorial essay. *Journal of Indian Academy of Oral Medicine and Radiology*. 2014;26(3):293.
17. Mao W, Gardner SJ, Snyder KC, et al. On the improvement of CBCT image quality for soft tissue-based SRS localization. *Journal of applied clinical medical physics*. 2018;19(6):177-184.
18. Gardner SJ, Studenski MT, Giaddui T, et al. Investigation into image quality and dose for different patient geometries with multiple cone-beam CT systems. *Medical physics*. 2014;41(3).
19. Cha BK, Jeon S, Seo C-W, et al. Optimization of X-ray image acquisition and reconstruction for a C-arm CBCT system with a flat-panel detector. *Nuclear Instruments and Methods in Physics Research Section A: Accelerators, Spectrometers, Detectors and Associated Equipment*. 2018.
20. Posiewnik M, Piotrowski T. A review of cone-beam CT applications for adaptive radiotherapy of prostate cancer. *Physica Medica*. 2019;59:13-21.

21. Hansen DC, Landry G, Kamp F, et al. ScatterNet: A convolutional neural network for cone-beam CT intensity correction. *Medical physics*. 2018;45(11):4916-4926.
22. Shi L, Wang AS, Wei J, Zhu L. Fast shading correction for cone-beam CT via partitioned tissue classification. *Physics in medicine and biology*. 2019.
23. Pellerin O, Pereira H, Ty CVN, et al. Is dual-phase C-arm CBCT sufficiently accurate for the diagnosis of colorectal cancer liver metastasis during liver intra-arterial treatment? *European radiology*. 2019.1-11.
24. Altunbas C, Kavanagh B, Alexeev T, Miften M. Transmission characteristics of a two dimensional antiscatter grid prototype for CBCT. *Medical physics*. 2017;44(8):11.
25. Zhao W, Vernekohl D, Zhu J, Wang L, Xing L. A model-based scatter artifacts correction for cone beam CT. *Medical physics*. 2016;43(4):1736-1753.
26. Stankovic U, Ploeger LS, van Herk M, Sonke JJ. Optimal combination of anti-scatter grids and software correction for CBCT imaging. *Medical physics*. 2017;44(9):4437-4451.
27. Rührnschopf EP, Klingenbeck K. A general framework and review of scatter correction methods in x-ray cone-beam computerized tomography. Part 1: Scatter compensation approaches. *Medical physics*. 2011;38(7):4296-4311.
28. Rührnschopf and EP, Klingenbeck K. A general framework and review of scatter correction methods in cone beam CT. Part 2: scatter estimation approaches. *Medical physics*. 2011;38(9):5186-5199.
29. Maier J, Eulig E, Vöth T, et al. Real-time scatter estimation for medical CT using the deep scatter estimation: Method and robustness analysis with respect to different anatomies, dose levels, tube voltages, and data truncation. *Medical physics*. 2019;46(1):238-249.
30. Altunbas C, Park Y, Yu Z, Gopal A. A unified scatter rejection and correction method for cone beam computed tomography. *Medical Physics*. 2021;48(3):1211-1225.
31. Siewerdsen JH, Moseley D, Bakhtiar B, Richard S, Jaffray DA. The influence of antiscatter grids on soft-tissue detectability in cone-beam computed tomography with flat-panel detectors. *Medical physics*. 2004;31(12):3506-3520.
32. Wiegert J, Bertram M, Schaefer D, et al. Performance of standard fluoroscopy antiscatter grids in flat-detector-based cone-beam CT. Paper presented at: Medical Imaging 2004: Physics of Medical Imaging2004.

33. Alexeev T, Kavanagh B, Miften M, Altunbas C. Novel ring artifact suppression method for CBCT imaging with two-dimensional antiscatter grids. *Medical physics*. 2019.
34. Schafer S, W. Stayman J, Zbijewski W, Schmidgunst C, Kleinszig G, H. Siewerdsen J. Antiscatter grids in mobile C-arm cone-beam CT: effect on image quality and dose. *Medical physics*. 2012;39(1):153-159.
35. Alexeev T, Kavanagh B, Miften M, Altunbas C. Two-dimensional antiscatter grid: A novel scatter rejection device for Cone-beam computed tomography. *Medical physics*. 2018;45(2):529-534.
36. Park Y, Alexeev T, Miller B, Miften M, Altunbas C. Evaluation of scatter rejection and correction performance of 2D antiscatter grids in cone beam computed tomography [published online ahead of print 2021/02/09]. *Med Phys*. 2021;48(4):1846-1858.
37. Yu Z, Park Y, Altunbas C. Simultaneous scatter rejection and correction method using 2D antiscatter grids for CBCT [published online ahead of print 2020/04/22]. *Proc SPIE Int Soc Opt Eng*. 2020;11312.
38. Vogtmeier G, Dorscheid R, Engel KJ, et al. Two-dimensional anti-scatter grids for computed tomography detectors. Paper presented at: Medical Imaging 2008: Physics of Medical Imaging2008.
39. Tang C-M, Stier E, Fischer K, Guckel H. Anti-scattering X-ray grid. *Microsystem technologies*. 1998;4(4):187-192.
40. Lee S, Chung W. Quantitative analysis of effects of the grid specifications on the quality of digital radiography images. *Australasian physical & engineering sciences in medicine*. 2019;42(2):553-561.
41. Veldkamp WJ, Thijssen MA, Karssemeijer N. The value of scatter removal by a grid in full field digital mammography. *Medical Physics*. 2003;30(7):1712-1718.
42. Lehmann V, Rönnebeck S. MEMS techniques applied to the fabrication of anti-scatter grids for X-ray imaging. *Sensors and Actuators A: Physical*. 2002;95(2-3):202-207.
43. Goldenberg B, Lemzyakov A, Nazmov V, Palchikov E. LIGA method of forming high-contrast collimators and anti-scatter grids with high aspect ratio. *Resource-Efficient Technologies*. 2018. (2):1-4.
44. Grasso M, Colosimo BM. Process defects and in situ monitoring methods in metal powder bed fusion: a review. *Measurement Science and Technology*. 2017;28(4):044005.

45. Kretzschmar N, Ituarte IF, Partanen J. A decision support system for the validation of metal powder bed-based additive manufacturing applications. *The International Journal of Advanced Manufacturing Technology*. 2018;96(9-12):3679-3690.
46. Sun S, Brandt M, Easton M. Powder bed fusion processes: An overview. In: *Laser Additive Manufacturing*. Elsevier; 2017:55-77.
47. Wu H, Li J, Wang H. Removing ring artifacts in cone-beam CT via TV-Stokes and unidirectional total variation model. *Medical physics*. 2019.
48. Altunbas C, Lai CJ, Zhong Y, Shaw CC. Reduction of ring artifacts in CBCT: Detection and correction of pixel gain variations in flat panel detectors. *Medical physics*. 2014;41(9).
49. Bartlett JL, Li X. An overview of residual stresses in metal powder bed fusion. *Additive Manufacturing*. 2019.
50. Wang C-S, Chang T-R, Hu Y-N, Hsiao C-Y, Teng C-K. STL mesh re-triangulation in rapid prototyping manufacturing. Paper presented at: IEEE International Conference on Mechatronics, 2005. ICM'05.2005.
51. Gibson I, Rosen D, Stucker B, Khorasani M. Design for additive manufacturing. In: *Additive manufacturing technologies*. Springer; 2021:555-607.
52. Ghouse S, Babu S, Van Arkel RJ, Nai K, Hooper PA, Jeffers JR. The influence of laser parameters and scanning strategies on the mechanical properties of a stochastic porous material. *Materials & Design*. 2017;131:498-508.
53. Ciurana J, Hernandez L, Delgado J. Energy density analysis on single tracks formed by selective laser melting with CoCrMo powder material. *The International Journal of Advanced Manufacturing Technology*. 2013;68(5-8):1103-1110.
54. Isaza J, Aumund-Kopp C, Wieland S, Petzoldt F, Bauschulte M, Fraunhofer DG. AM-Special Processes and Materials: New Materials and Applications by 3D-Printing for Innovative Approaches. Paper presented at: European Congress and Exhibition on Powder Metallurgy. European PM Conference Proceedings2015.
55. Hubbell JH, Seltzer SM. *Tables of X-ray mass attenuation coefficients and mass energy-absorption coefficients 1 keV to 20 MeV for elements Z= 1 to 92 and 48 additional substances of dosimetric interest*. National Inst. of Standards and Technology-PL, Gaithersburg, MD (United ...;1995.
56. Guo M, Gu D, Xi L, Du L, Zhang H, Zhang J. Formation of scanning tracks during Selective Laser Melting (SLM) of pure tungsten powder: Morphology, geometric features and forming mechanisms. *International Journal of Refractory Metals and Hard Materials*. 2019;79:37-46.

57. Mingear J, Zhang B, Hartl D, Elwany A. Effect of process parameters and electropolishing on the surface roughness of interior channels in additively manufactured nickel-titanium shape memory alloy actuators. *Additive Manufacturing*. 2019;27:565-575.
58. Yang Y, Jamshidinia M, Boulware P, Kelly S. Prediction of microstructure, residual stress, and deformation in laser powder bed fusion process. *Computational Mechanics*. 2018;61(5):599-615.
59. Baronette R. Quantitative Analysis of Three-Dimensional Cone-Beam Computed Tomography Using Image Quality Phantoms. 2018.
60. Cobos SF, Nikolov HN, Pollmann SI, Holdsworth DW. Reduction of ring artifacts caused by 2D anti-scatter grids in flat-panel CBCT. Paper presented at: Medical Imaging 2020: Physics of Medical Imaging2020.
61. Chakraborty D, Tarafder MK, Banerjee A, Chaudhuri SB. Gabor-based spectral domain automated notch-reject filter for quasi-periodic noise reduction from digital images. *Multimedia Tools and Applications*. 2019;78(2):1757-1783.
62. Fokas G, Vaughn VM, Scarfe WC, Bornstein MM. Accuracy of linear measurements on CBCT images related to presurgical implant treatment planning: A systematic review. *Clinical oral implants research*. 2018;29:393-415.
63. Du LY, Umoh J, Nikolov HN, Pollmann SI, Lee T-Y, Holdsworth DW. A quality assurance phantom for the performance evaluation of volumetric micro-CT systems. *Physics in Medicine & Biology*. 2007;52(23):7087.
64. Petrov IE, Nikolov HN, Holdsworth DW, Drangova M. Image performance evaluation of a 3D surgical imaging platform. Paper presented at: Medical Imaging 2011: Physics of Medical Imaging2011.
65. Altunbas C, Alexeev T, Miften M, Kavanagh B. Effect of grid geometry on the transmission properties of 2D grids for flat detectors in CBCT. *Physics in Medicine & Biology*. 2019;64(22):225006.
66. Sydney L.M. Wilson SP, Hristo N, Nikolov, Rob Stodilka, David W. Holdsworth. Highly Focused Collimators for Increased Resolution of Hand-Held Gamma Probes. Paper presented at: Imaging Network Ontario Symposium; March 23-24, 2021.
67. Mercelis P, Kruth JP. Residual stresses in selective laser sintering and selective laser melting. *Rapid prototyping journal*. 2006.
68. Hussein A, Hao L, Yan C, Everson R, Young P. Advanced lattice support structures for metal additive manufacturing. *Journal of Materials Processing Technology*. 2013;213(7):1019-1026.

69. Xie Y-j, Yang H-c, Wang X-b, Zhao L, Kuang C-j, Han W. Control of wall thickness and surface morphology of tungsten thin wall parts by adjusting selective laser melting parameters. *Journal of Iron and Steel Research International*. 2019;26(2):182-190.
70. Edey D, Pollmann S, Lorusso D, Drangova M, Flemming R, Holdsworth D. Extending the dynamic range of biomedical micro-computed tomography for application to geomaterials. *Journal of X-ray science and technology*. 2019;27(5):919-934.

Chapter 5

5 General discussion and conclusions

In this chapter, an overview of the development of each body of research (Chapters 2 – 4) is provided and a summary of the conclusions for each section is discussed. Additionally, the limitations of each project are presented, and future work proposed.

5.1 Development of the bodies of research

Before summarizing the conclusions, limitations, importance, and future work related to this dissertation as a whole (Chapters 2-4), the overall development of each body of research needs to be explained. In particular, the reasons for the development of each chapter individually and in parallel. Table 5-1 summarizes the timeline for each project with respect to the first four years of the research program.

Table 5-1. Overall development of bodies of research

Year one	Year two	Year three	Year four
2D-ASG			
	Cost-effective CT system		
			HDR-CT

As seen in Table 5-1, the first year was devoted only to the development of our large-area, two-dimensional, anti-scatter grid (2D-ASG) project (Chapter 4). This project was prioritized, at that time, as we were in an exceptional position to develop meaningful collaborations with two of our industrial partners (Renishaw and Carestream Health). One of these collaborations included the help of a Renishaw’s senior biomedical engineer (Matt Parkes) who was temporally working in London at our additive manufacturing centre. His knowledge of metal 3D-printing was instrumental for the success in the manufacturing of our large-area 2D-ASG. The second collaboration revolved around the interest of Carestream Health for the development of new technologies using their new line of wireless flat-panel detectors. The clinically available flat-panel detector that was used for the 2D-ASG project (Chapter 4), shares the same technology used in one of

Carestream's peripheral cone-beam CT scanners. For these reasons we decided to switch the focus of the anti-scatter grid project from non-destructive testing to low-energy clinical applications. This strategic decision did not compromise the objectives of this dissertation, as the challenges for the design, manufacturing, and implementation of 2D-ASGs for non-destructive testing are similar to the challenges for their clinical application.

The other two projects (Chapter 2 and 3) were developed in parallel due to the reduced research capacity caused by the COVID-19 pandemic, which delayed the manufacturing and implementation of the cost-effective CT machine – described in Chapter 2. Ideally, this low-cost CT scanner could have been used as the data acquisition hardware for the high-dynamic range CT project (Chapter 3). Instead, we took advantage of one of the pre-clinical CT scanners that we have available at our pre-clinical imaging facilities to speed up the high-dynamic range data acquisition process. Again, we strongly believe this strategic decision did not impact the objectives of this dissertation because the pre-clinical CT scanner was operated using a protocol that matched the imaging capabilities of the proposed cost-effective CT scanner. Furthermore, the pre-clinical scanner is equipped with an x-ray unit with the exact same characteristics as the x-ray unit intended to be used with the cost-effective scanner. Finally, we do not anticipate any major difficulties in the future integration of the high-dynamic range protocol with the described cost-effective CT scanner.

5.2 Overview and Objectives

Additive manufacturing (AM), especially laser powder-bed fusion (LPBF), has the potential to transform the way we manufacture biomedical components due to its ability to increase object bio-compatibility,¹⁻⁴ improve cost-effectiveness,^{5,6} and enhance patient-specific-care.⁷⁻⁹ However, routine quality control of components manufactured using LPBF becomes challenging because the specific object to be used must be tested non-destructively (NDT).^{10,11} Routine quality control, which is a major road block for the implementation of LPBF in the health sector, could ensure the stability of the AM process, and properly assess component quality prior to clinical use.¹⁰⁻¹² Cone beam CT, which is the preferred imaging modality for this task,¹³ allows precise quantification and

visualization of the entire microarchitecture of an object – with resolutions on the order of several micrometers.^{10,14} This visualization is accomplished by generating a series of three-dimensional cross-sectional images using many individual two-dimensional radiographic projections captured at different angles around the component. Unfortunately, in the medical sector, where the cost of testing must be commensurate with the cost of the part, NDT using currently available industrial CT systems is prohibitively expensive. In addition, cone-beam geometries, which are typical of CT-based NDT, amplify the negative effects of scattered radiation, leading to a reduction in image contrast, a degradation of image quality, and a loss in the diagnostic capabilities of the NDT.^{15,16} Moreover, cone-beam CT is not immune to other confounding errors, such as under-ranging, which affects the CT reconstructions introducing additional artifacts (*e.g.*, streaks and cupping artefacts).¹⁷⁻¹⁹ The objective of this research was to design, manufacture, and implement a cost-effective solution for post-manufacturing NDT of biomedical components fabricated with medical-grade titanium-alloy using LPBF by optimizing the acquisition hardware required for NDT using cone-beam CT imaging. Additionally, we developed two novel strategies to reduce common cone-beam CT image artifacts caused by scatter radiation and photon-starvation. The technologies developed in this dissertation have the potential to accelerate implementation of LPBF using titanium-alloys, allowing manufacturers to take full advantage of the tremendous potential of AM to produce biomedical components with enhanced clinical value.

5.3 Cost-effective NDT of titanium-alloy biomedical components

The first objective of this dissertation was to design, manufacture, and implement a cost-effective CT system for non-destructive testing of titanium alloy biomedical components. In Chapter 2, we demonstrated that routine NDT of titanium-alloy medical components fabricated using LPBF can be achieved without the need of prohibitively expensive scanners like the Nikon XT H 225, which weighs over 2400 kg and costs more than \$750,000. We accomplished this task by manufacturing a low-cost scanner and by optimizing the CT imaging of titanium-alloy LPBF-fabricated components, using low-

energy x-rays (*i.e.*, 80 kVp) and cost-effective x-ray detector technology (*i.e.*, a scintillating-screen lens-coupled to a dSLR camera).

We used the work conducted by Panna et al.²⁰ as the basis to design our system using a front-lit tilted detector geometry, combined with a carefully planned compact assembly of the other components of the CT scanner. These two strategies allowed us to overcome the light sensitivity limitations of previously described lens-coupled detector systems:²¹⁻²⁴ (1) by improving the x-ray fluence using the front-lit configuration and the close assembly, and (2) by reducing the demagnification required to image an appropriate field-of-view using a dSLR camera with a full-frame (36 by 24 mm) photosensor. Although, this approach has been used for advanced x-ray imaging techniques,²⁵⁻²⁷ this is the first implementation for medium-size, high-definition, CT scanning. In this context, we have also described a feasible geometric calibration correction to account for the distortion caused by the tilted scintillating screen.

Imaging systems must be designed to produce the highest possible signal-to-noise ratio (SNR). Lens-coupled detectors generate an image based on the conversion of optical photons into electric charge using a photodetector. These optical photons are emitted by the scintillator and are the result of the conversion of x-ray photons into optical photons.²⁸ Scintillators usually convert only 7.5% of the x-ray photon energy into visible light. For example, an 80 keV x-ray photon will yield approximately 2400 green, 2.5 eV, optical photons. If the light collection efficiency of the lens, and the camera's photosensor is not sufficient to generate at least one electric charge per incident x-ray photon the detector will be quantum noise limited (*i.e.*, a secondary quantum sink). Our cost-effective scanner achieved a conversion ratio between x-ray photons and electric charges that was calculated to be ~ 2 . This is mainly due to the low demagnification ($m = 7.5$) required to image a 225 by 180 mm field-of-view using a dSLR camera with a full-frame photodetector. We believe that the positive results we achieved with our lens-coupled detector are closely linked to this acceptable conversion of x-ray photons into electric charge. As described in Chapter 2, this light sensitivity could be improved by removing the Bayer filter of the commercially available camera, or by adapting the field-

of-view to the sample's size, which will decrease the demagnification of the system and therefore significantly increase light sensitivity.

Non-destructive testing (NDT) using industrial CT imaging has been described as a costly methodology.^{10,11} The cost associated with NDT using CT imaging has been a major point of discussion when proposing routine testing of parts produced using additive manufacturing technologies like laser powder-bed fusion.¹¹ By tailoring this technology to the specific case of NDT of medical components fabricated using titanium-alloy, and using low-cost data acquisition hardware, we have been able to propose a significantly more cost-effective solution. Our scanner was able to match most of the required characteristics for the task including: a medium-sized field-of-view, acceptable noise levels, voxel spacing, porosity evaluation, geometric evaluation, and low artifact levels. Although our spatial resolution was slightly over the recommended value for NDT in the medical sector (*i.e.*, $\leq 100 \mu\text{m}$) we strongly believe this limitation will be easily resolved when using a microfocus x-ray source. As described in Chapter 2 the image blur caused by the large focal spot of the clinical x-ray tube, which was used as an alternative due to COVID restrictions, will be decreased at least one order of magnitude. Future work for this project includes the replacement of the clinical x-ray tube by the proposed portable, microfocus, x-ray source to improve the effective spatial resolution of the system. It also includes the modification of the camera's photosensor by removing its Bayer filter to increase its quantum efficiency. And finally, it includes exploring the use of mirrorless cameras to improve data collection and data transferring times.

The imaging of highly attenuating materials using cone-beam CT presents a variety of special challenges because projection images with regions with low signal-to-noise ratio (SNR) are responsible for severe artifacts in the CT reconstructions. Modifying the imaging parameters to increase photon fluence in these regions (*e.g.*, increasing the x-ray source current), and thereby improving SNR, is not possible due to the limited dynamic-range of x-ray detection systems. For this reason, imaging parameters are optimized to prevent saturation of the detector elements where there is no object present, producing areas of low photon fluence (*i.e.*, under-ranging). High-dynamic-range radiography (HDR) can be defined as a collection of techniques used to increase the dynamic-range of

x-ray based imaging systems and therefore reduce the image artifacts caused by under-ranging.^{17-19,29-32} The objective of this chapter was to develop a high-dynamic-range technique for fixed-current, 80 kVp energy potential, CT imaging for NDT of titanium-alloy LPBF medical components. The fixed current and energy potential constrains for this project, described below, were imposed to match the imaging capabilities of our cost-effective CT scanner and therefore align with the general objective of this dissertation. In this context, we have developed, implemented, and evaluated a novel dual-exposure technique for high-dynamic range radiography. We describe a method to increase the SNR of obscured regions in the projection images by combining a short-exposure acquisition with a long-exposure acquisition. Our work also includes the description of a novel technique for combining the dual-exposure data to reduce discontinuity artifacts, which are commonly seen in other high-dynamic range CT approaches.^{17,19,32}

Other research groups have proposed similar dual-exposure, high-dynamic range, radiographic techniques for CT imaging,^{19,32} including NDT of metal parts,¹⁷ but these techniques use either varying tube potentials (*i.e.*, kVp) or varying tube currents (*i.e.*, mA). Since the portable x-ray unit proposed to be used with our cost-effective scanner (Chapter 2) has a fixed current (*i.e.*, 0,5 mA) and a maximum 80 kVp energy potential, a novel dual-exposure technique based on varying integration times was developed. We have demonstrated that the proposed method alleviates the artifacts caused by photon starvation, particularly in the case of imaging medical components that are required to have thick sections of metal (*i.e.*, > 17 mm of solid titanium). A limitation of this HDR technique is that it will increase the scan time and therefore the cost of testing. Nevertheless, the current trends for the design of biomedical components are leaning towards the use of optimized highly-porous designs.³³ For example, in recent years novel porous geometries that use infinitely connected triply periodic minimal surfaces (*e.g.*, like the gyroid) have been proposed to improve the mechanical properties of highly porous implants.³⁴ Future work for this project includes the testing of our cost-effective solution using more clinically relevant geometries.

Future work also includes the integration of the proposed high-dynamic range technique with our cost-effective CT scanner. As previously mentioned, we do not anticipate any

major difficulties for achieving this goal. In contrast, we believe that some of the hurdles that we had to overcome when using the pre-clinical scanner will be minimized when using our cost-effective CT scanner. For example, we did not have complete control of the commercial CT scanner during the data acquisition process, and were therefore forced to acquire two full scans with two different protocols. This caused registration problems between the datasets when using the regular hardware of the scanner. This situation will be easily avoided with our cost-effective scanner, as we could acquire the short- and long-exposure projection images one after the other. Furthermore, the fiber-optic coupled CCD detector of the pre-clinical scanner might be more susceptible to ghosting and image lag than our lens-coupled detector. Ghosting and image lag caused a suboptimal gain and offset correction for integration times that were 8 or 16 times longer than the baseline, which produced ring artifacts in the reconstructions. These artifacts are often described as “memory effects” and are more conspicuous for consecutive high-dose imaging and fluoroscopy.³⁵ If ghosting and lag were to affect the lens-coupled detector with the same intensity, the design of our scanner will allow the easy implementation of a technique described by Snoeren et al.³⁵, where ghosting and lag artifacts are reduced by exposing the scintillating screen to UV radiation. Snoeren et al. have demonstrated that UV radiation can prevent the trapping/de-trapping of x-ray generated charge at the imperfections of the scintillating crystals. These traps, which are in part responsible for memory artifacts, can be continuously filled using a UV “refreshing light”, thus reducing the effects of image lag and ghosting.³⁵

5.4 Large-area 2D focused anti-scatter grids

Recent advancements in additive manufacturing allow the fabrication of highly focused two-dimensional anti-scatter grids (2D-ASGs), which are well described devices for scatter removal,³⁶⁻³⁸. This 2D-ASGs do not require additional supporting material that otherwise would reduce the intensity of primary x-rays compromising their potential improvements in image quality. Furthermore, these grids have sub-pixel septal thickness, which allows for the correction of grid line artifacts while maintaining high primary x-ray transmission efficiency. The objective of this study was to design, manufacture, and evaluate a large-area, two-dimensional, focused, anti-scatter grid for scatter reduction in

cone-beam CT. We believe that we have described four clear innovations in this field of research. (1) To our knowledge, this is the first scientific publication evaluating the performance of an anti-scatter grid covering a significant (475 cm^2) area of a flat-panel detector (2), We have developed a fast and parametric method for focused, anti-scatter grid design using open-source software (3) We describe a novel method to remove grid-line artifacts using a combination of an adaptive gain correction and Fourier notch-filtering, and (4) We have demonstrated that cobalt-chrome alloys might be a suitable material for scatter removal for applications using energy potentials up to 80 kVp.

Although we decided to focus on the clinical implementation of our 2D-ASG due to previously described reasons, the impact that this device could have for scatter reduction in image-based NDT is significant. Especially considering that at 80 kVp roughly half of the photons interact with medical grade titanium by Compton scatter, rather than photoelectric absorption. Nonetheless, we understand that for NDT applications the selection of the 2D-ASG material might be critical and we anticipate that for this application tungsten will perform superiorly than cobalt-chrome alloy. We also anticipate that there will be limitations for the integration of the described 2D-ASG (Chapter 4) and our cost-effective CT scanner (Chapter 2), mainly due to the front-lit tilted geometry of the scintillating screen and the limited space of the compact assembly. On the positive side, we are now in a position to innovate in the field and perhaps design a novel grid geometry that could adapt to the geometry of our cost-effective CT scanner. One alternative will be to design a grid with an adapting pitch and ratio to adjust for the variable scatter field across the scintillating screen. The scatter field will be asymmetric due to the presence of a variable air-gap between the sample and the tilted screen. In areas with a larger air-gap between the object and the scintillating screen, where the scatter field will be less intense, the pitch of the grid could be increased and the ratio reduced in order to make the manufacturing of the focused grid septa in that region more feasible.

Future work includes the design and manufacturing of tungsten 2D-ASGs that will be adapted for the geometries of some of the pre-clinical micro-CT scanners located at our imaging facilities. In this case, scatter reduction will improve the quantitative value of the

data used for pre-clinical research. Additionally, our research group has modified the 2D-ASG parametric modelling software for the design of focused collimators for applications in nuclear medicine.³⁹

5.5 Significance and future directives

This dissertation has described the development of new technologies for cost-effective NDT of titanium-alloy, LPBF, 3D-printed medical components. These technologies have the potential to be incorporated into routine quality assurance and validation as part of a medical devices quality management system. By reducing the cost of the x-ray detector, the x-ray source, and required shielding, we have ensured that the scan cost will be a small fraction of the overall cost of the validated component. We have demonstrated that by taking advantage of several characteristics of AM-fabricated titanium-alloy medical components, NDT can be done using a relatively low-energy potential (*i.e.*, 80 kVp). For instance, the object may be complex but porous, which reduces the effective total path-length through the metal. Our system will allow each 3D-printed part to be scanned and compared to CAD specifications before clinical use. This will provide a competitive edge in meeting regulatory requirements, enhancing component quality, and ensuring the best patient outcome.

Aside from NDT of medical components, the work on this dissertation has contributed to the development of other research programs within the Robarts Research institute and between university departments (*e.g.*, biomedical engineering and anthropology). For example, the parametric modelling software and the development of additive manufacturing protocols for the manufacturing of anti-scatter grids have been instrumental for the manufacturing of tungsten gamma collimators that are currently being investigated by our group for applications in nuclear medicine and cancer surgical treatment.³⁹ Additionally, the gyroid-based, highly-porous, test samples designed to test our low-cost CT scanner have been utilized in a few research projects including: one investigating drug-delivery for infection control in orthopedic applications,⁴⁰ and a second optimizing magnetic resonance imaging near porous metal implants.⁴¹ Finally, through the Collaborative Specialization in Musculoskeletal Health Research program,

we have learned about the opportunities for the use of cost-effective and portable solutions for CT imaging in archaeology.

Future directives include the further development of these collaborations with other areas of research. Mainly, our cost-effective CT scanner has the potential to generate a significant impact in exploration of remote archaeological sites, where the removal of samples from the locality might be culturally insensitive or impractical.⁴² Our scanner could be easily disassembled and transported to these sites, reducing the costs and risks associated with sample transport. Furthermore, the dSLR camera, which is part of the system, could perform additional duties related to photographic and photometric analysis, thereby increasing the cost-effectiveness of the hardware for this task. The establishment of a temporary research site should include x-ray safety considerations to avoid the transport of heavy x-ray shielding. An alternative will be to restrict the access to the perimeter, where the scanner is operating, using wireless interlocks, and to use wireless technology for scanner control. Space exploration is another related application of the technology described in this dissertation, as extended space missions are a good example of a situation where a portable CT imaging systems will be of great value.⁴³ The design of our cost-effective scanner could be tailored for this application, by reducing the overall size and weight of the housing frame, and by reducing the field-of-view to match the requirements for geological samples. Again, the photographic hardware included in the CT scanner could be used for other research tasks.

In conclusion, this dissertation has presented a variety of novel technologies for advanced, volumetric, radiographic applications where the cost-effectiveness, the portability, and the versatility of the imaging system is paramount. We have demonstrated that CT-based non-destructive testing of medical components can be accomplished using cost-effective hardware, and that common CBCT artifacts caused by scatter radiation and under-ranging can be reduced using 2D focused anti-scatter grids and high-dynamic range radiography, respectively. These technologies have the potential to accelerate clinical implementation of novel, custom, bio-compatible, AM-manufactured, medical components.

5.6 References

1. Fousová M, Vojtěch D, Kubásek J, Jablonská E, Fojt J. Promising characteristics of gradient porosity Ti-6Al-4V alloy prepared by SLM process. *Journal of the mechanical behavior of biomedical materials*. 2017;69:368-376.
2. Hedia H, Aldousari S, Abdellatif A, Fouda N. A new design of cemented stem using functionally graded materials (FGM). *Bio-medical materials and engineering*. 2014;24(3):1575-1588.
3. Kováčik J. Correlation between Young's modulus and porosity in porous materials. *Journal of materials science letters*. 1999;18(13):1007-1010.
4. Choren JA, Heinrich SM, Silver-Thorn MB. Young's modulus and volume porosity relationships for additive manufacturing applications. *Journal of materials science*. 2013;48(15):5103-5112.
5. Wang D, Wang Y, Wu S, et al. Customized a Ti6Al4V bone plate for complex pelvic fracture by selective laser melting. *Materials*. 2017;10(1):35.
6. Liu Y, Wang W, Zhang L-C. Additive manufacturing techniques and their biomedical applications. *Family Medicine and Community Health*. 2017;5(4):286-298.
7. Mattei L, Pellegrino P, Calò M, Bistolfi A, Castoldi F. Patient specific instrumentation in total knee arthroplasty: a state of the art. *Annals of translational medicine*. 2016;4(7).
8. Rengier F, Mehndiratta A, Von Tengg-Kobligk H, et al. 3D printing based on imaging data: review of medical applications. *International journal of computer assisted radiology and surgery*. 2010;5(4):335-341.
9. Höhne J, Brawanski A, Gassner HG, Schebesch K-M. Feasibility of the custom-made titanium cranioplasty CRANIOTOP®. *Surgical neurology international*. 2013;4.
10. du Plessis A, le Roux SG, Guelpa A. Comparison of medical and industrial X-ray computed tomography for non-destructive testing. *Case Studies in Nondestructive Testing and Evaluation*. 2016;6:17-25.
11. Khosravani MR, Reinicke T. On the use of X-ray computed tomography in assessment of 3D-printed components. *Journal of Nondestructive Evaluation*. 2020;39(4):1-17.
12. Kastner J, Heinzl C. X-ray computed tomography for non-destructive testing and materials characterization. In: *Integrated Imaging and Vision Techniques for Industrial Inspection*. Springer; 2015:227-250.

13. Du Plessis A, le Roux SG, Els J, Booysen G, Blaine DC. Application of microCT to the non-destructive testing of an additive manufactured titanium component. *Case Studies in Nondestructive Testing and Evaluation*. 2015;4:1-7.
14. Ewert U, Fuchs T. Progress in Digital Industrial Radiology. Pt. 2, Computed tomography (CT). *Badania Nieniszczące i Diagnostyka*. 2017.
15. Siewerdsen JH, Jaffray DA. Cone-beam computed tomography with a flat-panel imager: Magnitude and effects of x-ray scatter. *Medical physics*. 2001;28(2):220-231.
16. Siewerdsen JH, Moseley D, Bakhtiar B, Richard S, Jaffray DA. The influence of antiscatter grids on soft-tissue detectability in cone-beam computed tomography with flat-panel detectors. *Medical physics*. 2004;31(12):3506-3520.
17. Chen P, Han Y, Pan J. High-dynamic-range CT reconstruction based on varying tube-voltage imaging. *PLoS One*. 2015;10(11):e0141789.
18. Fox T, Nisius D, Duncan M, Duncan M. Dynamic range extension of x-ray imaging system used in non-invasive inspection of contraband in vehicles, involves amplifying identical samples of x-ray beams using respective gain values, and forming x-ray image. *US Patent*. 2005.2005047546-A2005047541.
19. Sisniega A, Abella M, Desco M, Vaquero J. Dual-exposure technique for extending the dynamic range of x-ray flat panel detectors. *Physics in Medicine & Biology*. 2013;59(2):421.
20. Panna A, Gomella A, Harmon K, et al. Performance of low-cost X-ray area detectors with consumer digital cameras. *Journal of Instrumentation*. 2015;10(05):T05005.
21. Fan HX. *Lens-coupled x-ray imaging systems*, The University of Arizona; 2015.
22. Madden TJ, McGuigan W, Molitsky MJ, Naday I, McArthur A, Westbrook EM. Lens-Coupled CCD detector for x-ray crystallography. Paper presented at: 2006 IEEE Nuclear Science Symposium Conference Record2006.
23. Tate MW, Chamberlain D, Gruner SM. Area x-ray detector based on a lens-coupled charge-coupled device. *Review of scientific instruments*. 2005;76(8):081301.
24. Uesugi K, Hoshino M, Yagi N. Comparison of lens-and fiber-coupled CCD detectors for X-ray computed tomography. *Journal of synchrotron radiation*. 2011;18(2):217-223.
25. George A, Chen PY, Morales-Martinez A, et al. Geometric calibration and correction for a lens-coupled detector in x-ray phase-contrast imaging. *Journal of Medical Imaging*. 2017;4(1):013507.

26. Abel LB. *Design and analysis of low-cost x-ray imaging system incorporating consumer camera imaging*, Massachusetts Institute of Technology; 2018.
27. Nguyen V-G. Digital Radiography with a Consumer Camera: Image Denoising and Deblurring. *IEIE Transactions on Smart Processing & Computing*. 2021;10(5):398-406.
28. Yaffe M, Rowlands J. X-ray detectors for digital radiography. *Physics in Medicine & Biology*. 1997;42(1):1.
29. Edey D, Pollmann S, Lorusso D, Drangova M, Flemming R, Holdsworth D. Extending the dynamic range of biomedical micro-computed tomography for application to geomaterials. *Journal of X-ray science and technology*. 2019;27(5):919-934.
30. Li Y, Han Y, Chen P. X-ray energy self-adaption high dynamic range (HDR) imaging based on linear constraints with variable energy. *IEEE Photonics Journal*. 2017;10(2):1-14.
31. Nittoh K, Oyaizu E, Sakurai T, Yoshida T, Mochiki K-I. Extension of dynamic range in X-ray radiography using multi-color scintillation detector. *Nuclear Instruments and Methods in Physics Research Section A: Accelerators, Spectrometers, Detectors and Associated Equipment*. 2003;501(2-3):615-622.
32. Sukovic P, Clinthorne NH. A method for extending the dynamic range of flat panel imagers for use in cone beam computed tomography. Paper presented at: 2001 IEEE Nuclear Science Symposium Conference Record (Cat. No. 01CH37310)2001.
33. Mahmoud D, Elbestawi MA. Lattice structures and functionally graded materials applications in additive manufacturing of orthopedic implants: a review. *Journal of Manufacturing and Materials Processing*. 2017;1(2):13.
34. Guariento L, Buonamici F, Marzola A, Volpe Y, Governi L. Graded Gyroid Structures for Load Bearing Orthopedic Implants. Paper presented at: 2020 IEEE 10th International Conference Nanomaterials: Applications & Properties (NAP)2020.
35. Snoeren RM, Steinhauser H, Alving L, Stouten H. Flat detector ghost image reduction by UV irradiation. Paper presented at: Medical Imaging 2009: Physics of Medical Imaging2009.
36. Alexeev T, Kavanagh B, Miften M, Altunbas C. Two-dimensional antiscatter grid: A novel scatter rejection device for Cone-beam computed tomography. *Medical physics*. 2018;45(2):529-534.

37. Altunbas C, Kavanagh B, Alexeev T, Miften M. Transmission characteristics of a two dimensional antiscatter grid prototype for CBCT. *Medical physics*. 2017;44(8):11.
38. Park Y, Alexeev T, Miller B, Miften M, Altunbas C. Evaluation of scatter rejection and correction performance of 2D antiscatter grids in cone beam computed tomography [published online ahead of print 2021/02/09]. *Med Phys*. 2021;48(4):1846-1858.
39. Sydney L.M. Wilson SP, Hristo N. Nikolov, Rob Stodilka, David W. Holdsworth. Highly Focused Collimators for Increased Resolution of Hand-Held Gamma Probes. Paper presented at: Imaging Network Ontario Symposium; March 23-24, 2021.
40. Khazae T. Characterization and Enhancement of Local Drug Delivery in Orthopaedic Infection. 2020.
41. Hong G, Cobos FS, Khazae T, Liu J, Drangova M, Holdsworth DW. Effective magnetic susceptibility of 3D-printed porous metal scaffolds2021, *Magnetic Resonance in Medicine*.
42. Cobos SF, Stock JT, Nelson AJ, Holdsworth DW. Cost-effective micro-CT scanner for remote archaeological sites. Paper presented at: Image Network Ontario; March 26-27 2020, 2020; Virtual.
43. Cramer A, Hecla J, Wu D, et al. Stationary computed tomography for space and other resource-constrained environments. *Scientific reports*. 2018;8(1):1-10.

Curriculum Vitae

Name: **Santiago Fabian Cobos Cobos**

Post-secondary Education and Degrees: University of Cuenca
Cuenca, Azuay, Ecuador
2005-2010 D.D.S.

The University of Western Ontario
London, Ontario, Canada
2015-2017 M.Sc.

The University of Western Ontario
London, Ontario, Canada
2017-Present Ph.D. (candidate)

Honours and Awards: Dentistry Research Day (poster award)
2016,

Gabriel G. Altmann (research award)
2016,

Francis Chan (humanitarian award)
2017,

London Health Research Day (poster award)
2019

Imaging Network Ontario Symposium (pitch award)
2021

Related Work Experience Teaching Assistant
The University of Western Ontario
2016-2019; Oral Histology

Adjunct Clinical Instructor
The University of Western Ontario
2018-2020; Operative Dentistry

Limited-duties Course Coordinator
The University of Western Ontario
2018-2020; Applied Head and Neck Anatomy

Posters:

(2020) Cost-effective micro-CT scanner for remote archaeological sites. Imaging Network Ontario, Toronto, Canada

(2020) Sparse-view Cone-beam CT Reconstruction for Assessing Migration in Knee Arthroplasty: a Phantom Study. Imaging Network Ontario, Toronto, Canada.

(2020) MRI characterization of a Novel Porous 3D Printed Metal Scaffold. Imaging Network Ontario, Toronto, Canada

(2020) MRI Artifact Reduction Near 3D-Printed Porous Metal Scaffolds. Canadian Bone and Joint Conference, London, Canada

(2019) 3D Printed Large-area Grid for Scatter Reduction in Cone-beam CT. London Health Research Day. London, Canada

(2017) Topographic Analysis of the TMJ Glenoid Fossa using MicroCT Imaging. American Association of Anatomist, Chicago, United States

(2016) Topographic Analysis of the TMJ Glenoid Fossa using MicroCT Scans. Schulich Dentistry Annual Research Day, London, Canada

Presentations:

(2021) Cost-effective micro-CT imaging of medical components fabricated with additive manufacturing. Imaging Network Ontario, London, Canada

(2020) Reduction of Ring Artifacts Caused by 2D Anti-scatter Grids in Flat-panel CBCT. SPIE Medical Imaging, Huston, United States

(2020) Micro-CT Imaging Technique to Characterize Diffusion of Small Molecules. SPIE Medical Imaging, Huston, United States

(2019) Selective Laser Melted 2D Focused Anti-Scatter Grids for Cone-beam CT. Imaging Network Ontario, London, Canada

(2018) 3D-printed Anti-scatter Collimators for Artifact Reduction in Cone-beam CT. SIAM Conference on Imaging Science, Bologna, Italy

(2018) Parametric Modelling and Metal 3D Printing of Anti-Scatter Grids for Cone-Beam CT. Imaging Network Ontario, Toronto, Canada

Publications:

Published & Accepted

Cobos, S.F., Nikolov, H.N., Pollmann, S.I. and Holdsworth, D.W. (2020), March. Reduction of ring artifacts caused by 2D anti-scatter grids in flat-panel CBCT. In *Medical Imaging 2020: Physics of Medical Imaging* (Vol. 11312, p. 1131228). International Society for Optics and Photonics.

Goodman, C.D., Pautler, J.D., Balestrini, C.S., **Cobos, S.F.**, D'Souza, L., Eansor, P., Jaswal, J., Nichols, A., Norris, M., Sharma, M. and Willmore, K. (2021). Evaluation of a 3-Dimensional-Printed Head Simulation Technique for Teaching Flexible Nasopharyngoscopy to Radiation Oncology Residents. *International Journal of Radiation Oncology*Biography*Physics*, 109(2), 317-323.

Hong, G., **Cobos, S.F.**, Khazaei, T., Liu, J., Drangova, M. and Holdsworth, D.W. (2021) Effective magnetic susceptibility of 3D-printed porous metal scaffolds – in press. *Magnetic Resonance in Medicine*.

Submitted

Cobos S.F., Norley C.J., Nikolov H.N. and Holdsworth D.W. (2021) 3D printed large-area focused grid for scatter reduction in cone-beam CT. Submitted to *Medical Physics*.

Cobos S.F., Norley C.J., Pollmann S.I. and Holdsworth D.W. (2021) Cost-effective micro-CT system for non-destructive testing of titanium 3D printed medical components. Submitted to *Plos One*.

Cobos S.F., Norley C.J., Pollmann S.I. and Holdsworth D.W. (2021) High-dynamic-range micro-CT for non-destructive testing of titanium 3D-printed medical components. Submitted to *Biomedical Physics & Engineering Express*.